

# Alma Mater Studiorum Università di Bologna

---

---

SCUOLA DI SCIENZE

Corso di Laurea Magistrale in Astrofisica e Cosmologia

Dipartimento di Fisica e Astronomia

## The clustering properties of galaxy clusters in the AMICO-KiDS survey: constraints on the cosmological parameters and on the mass-richness relation

Tesi di laurea

Relatore:

**Dott. Federico Marulli**

Co-relatore:

**Ch.mo Prof. Lauro Moscardini**

Presentata da:

**Lorenza Nanni**

---

---

Sessione II  
Anno Accademico 2018/2019



# Contents

<b>Abstract</b>	<b>1</b>
<b>Sommario</b>	<b>2</b>
<b>Introduction</b>	<b>4</b>
<b>1 Cosmology</b>	<b>6</b>
1.1 Cosmological principle . . . . .	6
1.2 Fundamentals of General Relativity . . . . .	6
1.3 The Fridman-Lemaître-Robertson-Walker metric . . . . .	8
1.3.1 Cosmological distances . . . . .	9
1.3.2 The Hubble-Lemaître Law . . . . .	10
1.3.3 The cosmological redshfit and the scale factor . . . . .	10
1.3.4 Distance measures . . . . .	11
1.4 Friedmann Equations . . . . .	12
1.4.1 Einstein’s Static Universe . . . . .	12
1.4.2 Friedmann Models . . . . .	14
1.4.3 Flat, open and closed Universes . . . . .	14
1.4.4 The Big Bang . . . . .	16
1.5 The Standard Cosmological Model . . . . .	17
<b>2 Formation and evolution of cosmic structures</b>	<b>19</b>
2.1 Cosmic Inflation . . . . .	19
2.2 The Jeans Theory . . . . .	20
2.2.1 Jeans scale . . . . .	20
2.2.2 The Jeans Theory in static Universes . . . . .	21
2.3 The Jeans theory in expanding Universes . . . . .	22
2.3.1 Cosmological horizon . . . . .	22
2.3.2 Outside the Cosmological Horizon . . . . .	23
2.3.3 Inside the Cosmological Horizon . . . . .	23
2.4 Perturbation theory . . . . .	26
2.4.1 Punctual variance of the field and mass variance . . . . .	27
2.4.2 The primordial Zel’dovich spectrum . . . . .	28
2.4.3 The Transfer Function . . . . .	29
2.5 The evolution theory in the non-linear regime . . . . .	30
2.5.1 Spherical collapse . . . . .	31
2.5.2 N-body simulations . . . . .	31
2.5.3 The Mass and Luminosity functions . . . . .	32
<b>3 Clusters of galaxies</b>	<b>35</b>
3.1 Galaxy Clusters Observations . . . . .	35
3.2 Estimation of the mass . . . . .	36
3.2.1 X-ray emission . . . . .	36
3.2.2 The self-similar scaling . . . . .	37
3.2.3 Sunyaev-Zel’dovich effect . . . . .	37
3.2.4 Virial Theorem . . . . .	37

3.2.5	Luminosity and Richness . . . . .	38
3.3	Detection of clusters . . . . .	38
3.3.1	Identification in the X-ray band . . . . .	38
3.3.2	Identification through the SZ effect . . . . .	38
3.3.3	Identification in optical surveys . . . . .	38
3.4	Clusters as a cosmological probe . . . . .	39
<b>4</b>	<b>The correlation function</b> . . . . .	<b>41</b>
4.1	Clustering . . . . .	41
4.2	The Two-Point Correlation Function . . . . .	42
4.2.1	The 2PCF estimators . . . . .	42
4.3	Geometric distortions . . . . .	43
4.4	Redshift-space distortions . . . . .	44
4.4.1	The Photometric redshifts . . . . .	44
4.4.2	The 2D 2PCF estimators and dynamical distortions . . . . .	45
4.5	2PCF measures . . . . .	46
4.5.1	Projected and real-space correlations . . . . .	47
4.5.2	The 2PCF in the redshift-space . . . . .	48
4.6	Bias . . . . .	48
4.6.1	Theoretical bias models . . . . .	49
<b>5</b>	<b>The AMICO-KiDS galaxy cluster catalogue</b> . . . . .	<b>51</b>
5.1	The KiDS survey . . . . .	51
5.2	The AMICO detection algorithm . . . . .	52
5.2.1	Linear optimal matched filtering . . . . .	52
5.2.2	Models for member galaxies and field galaxies . . . . .	53
5.2.3	Mass proxies in AMICO . . . . .	54
5.3	The KiDS-AMICO cluster catalogue . . . . .	54
5.4	Mass-observable relation . . . . .	55
5.5	Main properties of our sample . . . . .	56
<b>6</b>	<b>Results</b> . . . . .	<b>58</b>
6.1	The CosmoBolognaLib . . . . .	59
6.2	Redshift-space 2PCF . . . . .	59
6.2.1	Evolution of bias . . . . .	61
6.3	The real-space 2PCF . . . . .	64
6.4	Constraints on the bias and the mean photo-z errors . . . . .	66
6.5	Cosmological parameters . . . . .	70
6.6	The scaling relation . . . . .	77
6.7	Comparison between the different bias estimation . . . . .	81
<b>7</b>	<b>Discussion and conclusions</b> . . . . .	<b>83</b>
7.1	Scientific background . . . . .	83
7.2	Discussion . . . . .	85
7.3	Conclusion and future perspectives . . . . .	86
<b>A</b>	<b>Bayesian statistics</b> . . . . .	<b>87</b>

# Abstract

Independent cosmological probes are required to accurately constrain the cosmological framework. During the last decades, several multi-wavelength large-scale surveys have been employed to collect representative samples of cosmic tracers. One of the main aims of these projects is to construct pure and complete galaxy cluster catalogues up to high redshifts, to extract cosmological constraints from the statistical properties of these structures. Galaxy clusters are the most massive virialised systems in the Universe, corresponding to the rare and highest peaks of the dark matter density field. Their statistical properties can thus be exploited to assess the matter density field and its growth. One of the main advantages in using galaxy clusters as cosmological probes is the possibility of measuring accurately their masses, with different independent methods, and thus constraining their effective bias as a function of the cosmological model. This cannot be achieved with galaxies or other cosmic tracers.

The clustering of galaxies provides one of the most powerful cosmological probes to constrain both the geometry and the dynamics of the Universe. In particular, large photometric galaxy samples are required to accurately measure their two-point correlation function (2PCF), or power spectrum, which can be used to assess the underlying density and velocity fields of the Universe. The clustering of galaxy clusters provides an independent probe of the large-scale structure of the Universe, which could not be satisfactorily exploited in the past due to the difficulties in building large enough cluster samples. The situation has dramatically changed during the past decades, when huge and accurately characterised cluster samples became publicly available, allowing the cosmological usage of cluster clustering up to large scales and redshifts (e.g. Veropalumbo et al., 2014, Sereno et al., 2015b, Veropalumbo et al., 2016, Marulli et al., 2018).

In this Thesis work, we present new measurements of the clustering of a photometric sample of galaxy clusters, focusing on the redshift-space 2PCF. The analysed galaxy cluster sample has been built using the *Adaptive Matched Identifier of Clustered Objects* (AMICO) algorithm (Maturi et al., 2019) on the Kilo-Degree Survey (KiDS, de Jong et al., 2017). We analyse the full catalogue, as well as sub-catalogues selected in mass and redshifts. All these new measurements are compared to theoretical predictions of the standard  $\Lambda$  cold dark matter ( $\Lambda$ CDM) cosmological framework, finding consistent results. Then, we perform a statistical analysis to extract constraints on the matter density contrast  $\Omega_M$ , the amplitude of the density fluctuations  $\sigma_8$ , the dark energy equation of state parameter  $w_0$ , and the effective bias of the sample. Specifically, assuming a  $\Lambda$ CDM framework, we obtain  $\Omega_M = 0.26 \pm 0.02$ ,  $\sigma_8 = 0.76 \pm 0.05$ ,  $S_8 = \sigma_8 \sqrt{\Omega_M/0.3} = 0.73 \pm 0.08$  and  $w_0 = -1.07 \pm 0.34$ , fixing the other parameters at Planck18 values (Aghanim et al., 2018a).

Finally, we present a new method to infer the cluster mass scaling relation from cluster clustering measurements, and provide constraints on the scaling relation normalisation, slope and scatter. The values obtained are  $\alpha = 0.04 \pm 0.05$ ,  $\beta = 1.9 \pm 0.5$  and  $\gamma = -1.3 \pm 0.5$ , consistent with constraints from weak gravitational lensing (Bellagamba et al., 2019). This represents the primary original result of this work.

The statistical analyses presented in this Thesis work have been performed with the CosmoBolognaLib, that are a large set of *free software* C++/Python numerical libraries for cosmological calculations, particularly useful to investigate the large-scale structure of the Universe (CBL, Marulli et al., 2016). Specifically, both the measurements and the statistical Bayesian analyses have been performed with the CBL V5.2. To constrain the cluster scaling relation from the redshift-space 2PCF, we implement and systematically validate new likelihood modules that were not present in the CBL before this work. These new functions will be released in a forthcoming version of the CBL.

# Sommario

Per vincolare accuratamente il modello cosmologico sono richiesti test indipendenti. Negli ultimi decenni, molte *survey* su grande scala e su più lunghezze d'onda sono state utilizzate per raccogliere campioni rappresentativi di traccianti cosmologici. Uno degli obiettivi principali di questi progetti è costruire cataloghi di ammassi di galassie *completi e puri* fino ad alti redshift per vincolare la cosmologia dalle proprietà statistiche di questi oggetti. Gli ammassi di galassie sono le strutture virializzate più massive presenti nell'Universo, corrispondendo ai picchi più alti e rari del campo di densità della materia oscura. Le loro proprietà statistiche possono dunque essere sfruttate per studiare il campo di densità della materia e la sua crescita. Uno dei vantaggi principali nell'utilizzare i cluster come strumenti di indagine cosmologica è la possibilità di misurare accuratamente la loro massa con metodi indipendenti e dunque vincolare il loro *bias effettivo* come funzione del modello cosmologico. Questo non può essere fatto per le galassie o altri traccianti cosmologici.

Il *clustering* delle galassie è uno dei più potenti test cosmologici sia per vincolare la geometria sia per vincolare la dinamica dell'Universo. In particolare, sono richieste survey spettroscopiche su grandi volumi cosmologici per misurare con accuratezza la funzione di correlazione a due punti (2PCF) o lo spettro di potenza, che possono essere sfruttati per ottenere informazioni sul campo di densità sottostante e sul campo di velocità dell'Universo.

Il clustering degli ammassi di galassie fornisce un test indipendente per studiare la struttura a grande scala dell'Universo, che non poteva essere sfruttato in passato per l'impossibilità di ottenere un campione di ammassi sufficientemente grande. La situazione è drasticamente cambiata negli ultimi decenni, quando grandi e accuratamente caratterizzati cataloghi di cluster vennero resi pubblici, permettendo lo studio cosmologico del clustering degli ammassi su grande scala e su un ampio range in redshift (per esempio Veropalumbo et al., 2014, Sereno et al., 2015b, Veropalumbo et al., 2016, Marulli et al., 2018).

In questo lavoro di Tesi presentiamo nuove misurazioni del clustering di un campione fotometrico di ammassi di galassie, concentrandoci sulla 2PCF nello spazio dei redshift. Il catalogo di ammassi di galassie analizzato è costruito usando l'algoritmo *Adaptive Matched Identifier of Clustered Objects* (AMICO) (Maturi et al., 2019) sulla Kilo-Degree Survey (KiDS, de Jong et al., 2017). È stato analizzato l'intero catalogo e anche diversi sotto-cataloghi, selezionati in massa e in redshift. Tutte queste misurazioni sono confrontate con le previsioni teoriche del modello cosmologico standard ( $\Lambda$  cold dark matter,  $\Lambda$ CDM), trovando risultati consistenti. È stata poi effettuata un'analisi statistica per fornire vincoli sul contrasto di densità della materia  $\Omega_M$ , sull'ampiezza delle fluttuazioni di densità  $\sigma_8$ , sul parametro dell'equazione di stato dell'energia oscura  $w_0$  e sul bias effettivo del catalogo. In particolare, assumendo uno scenario  $\Lambda$ CDM, otteniamo  $\Omega_M = 0.26 \pm 0.02$ ,  $\sigma_8 = 0.76 \pm 0.05$ ,  $S_8 = \sigma_8 \sqrt{\Omega_M/0.3} = 0.73 \pm 0.08$  e  $w_0 = -1.07 \pm 0.34$ , fissando gli altri parametri ai valori stimati da Planck18 (Aghanim et al., 2018a).

Infine presentiamo un nuovo metodo per stimare la relazione di scala tra la massa degli ammassi di galassie e le loro caratteristiche fotometriche utilizzando la misura del *clustering*, dando vincoli alla normalizzazione, alla pendenza e allo *scatter* della relazione di scala. I valori che otteniamo sono  $\alpha = 0.04 \pm 0.05$ ,  $\beta = 1.9 \pm 0.5$  e  $\gamma = -1.3 \pm 0.5$ , consistenti con quelli ottenuti da uno studio precedente che ha utilizzato dati di lensing gravitazionale debole (Bellagamba et al., 2019). Questo rappresenta il risultato originale più importante di questo lavoro di Tesi.

L'analisi statistica presentata in questa Tesi è condotta con le CosmoBolognaLib, che sono un'ampia libreria di *free software* C++/Python per studi cosmologici, particolarmente utile per studiare la struttura dell'Universo a grande scala. Nello specifico, sia la misurazione che l'analisi Bayesiana sono condotte con le CBL V5.2. Per vincolare la relazione di scala dalla 2PCF nello

spazio dei redshift, abbiamo implementato e validato nuovi moduli di likelihood che non erano presenti nelle CBL prima di questo lavoro. Queste nuove funzioni saranno rese pubbliche nella prossima versione delle CBL.



# Introduction

The  $\Lambda$ CDM cosmological model provides a satisfactory description of the Universe as a whole, and is currently considered as the standard cosmological framework. This model is based on two fundamental assumptions: the existence of cold Dark Matter particles and the presence of a non-null Cosmological Constant,  $\Lambda$ , in the Einstein field equations. The physical origin and behaviour of these two fundamental components of our Universe are far to be understood.

The Dark Matter is described as a matter component that interacts only through gravitation with the other matter components. In particular, in the standard cosmological model, the Dark Matter is assumed to be composed by non-relativistic particles.

The Dark Energy represents the dominant component in the Universe today. Described by the Cosmological Constant  $\Lambda$  in the standard framework, it is an energy component that has been introduced to explain the currently accelerated expansion of the Universe.

To our physical knowledge, both the Dark Matter and the Dark Energy are necessary to explain the formation and evolution of cosmic structures and the observed cosmic acceleration (Riess et al., 1998). These two components represent the  $\sim 27\%$  and  $\sim 68\%$  of the total mass-energy in the Universe, respectively. That means that only the  $\sim 5\%$  of the Universe is constituted of ordinary matter and radiation.

In the standard cosmological model there is also another fundamental assumption necessary to explain astronomical observations: the existence of an accelerated evolutionary period, called Inflationary Era, between  $10^{-33}$  to  $10^{-30}$  s after the Big Bang. Thanks to this assumption, it is possible to explain why the Universe is flat, the absence of the monopoles, and the homogeneity of the Universe on large scales. According to the  $\Lambda$ CDM model, the Inflationary Period sets the initial conditions of the Universe. At the end of this Era, the seeds for the structure formation are present, caused by the *inflaton decay*. The formation and evolution of cosmic structures in this framework starts at the end of this Era, and proceeds as described in the Jeans Theory.

In this scenario, galaxy clusters play a crucial role. They are hosted in the most massive CDM haloes and their evolution is dominated by the CDM component. Studying galaxy clusters, we can infer fundamental cosmological information. Indeed, investigating their mass function (Press et al., 1974) and the mass-to-light ratio (Schechter, 1976), it is possible to constrain the mass density parameter,  $\Omega_M$ , and the amplitude of the matter power spectrum,  $\sigma_8$  (Oukbir et al., 1992). Moreover, the cluster correlation function can be exploited to constrain cosmological parameters (e.g. Marulli et al., 2018). To assess reliable constraints, it is crucial to accurately estimate the cluster masses, possibly with multiple independent methods, such as gravitational lensing, X-ray or Sunyaev-Zel'dovich effect observations, and by calibrating scaling relations between some cluster observables and their masses.

In view of the ongoing and next-generation large photometric surveys that will explore the Universe in visible wavelengths, it is crucial to accurately estimate the cluster scaling relations involving photometric quantities. Gravitational lensing data are generally used to infer cluster masses in photometric optical surveys. Using this information together with the estimation of some photometric cluster properties, such as the richness, it is possible to derive cluster scaling relations.

In this Thesis work we introduce a new independent method to infer the cluster scaling relation using cluster clustering data. To do that, we implement new algorithms to constrain at the same time the  $\Lambda$ CDM parameters and the cluster scaling relation parameters from the redshift-space 2PCF of galaxy clusters. The new method is applied on the AMICO-KiDS catalogue, a photometric cluster sample recently constructed with the AMICO code from the Kilo-Degree Survey (see Maturi et al., 2019).

This Thesis is organised as follows:

- In Chapter 1, we will introduce the modern cosmological scenario, describing the  $\Lambda$ CDM model that will be the framework of our analysis.
- In Chapter 2, at first, we will present the Jeans Theory exploited to describe the formation and evolution of cosmic structures. Then, we will discuss in detail the perturbation theory and its prediction on the power spectrum.
- In Chapter 3, the main properties of galaxy clusters will be reported. Then we will focus on the different methods used to estimate their mass, being one of the main topics of this Thesis. Moreover, the different approaches to detect galaxy clusters will be illustrated.
- In Chapter 4, we will introduce the correlation function, that is the main statistical tool exploited in this Thesis work, giving the general definition and the most used estimators. We will describe the main issues in cluster clustering measurements. Finally, we will explain how to model the 2PCF, taking into account redshift-space distortions and photometric redshift uncertainties.
- In Chapter 5, we will illustrate how the AMICO-KiDS catalogue is extracted from the Kilo-Degree Survey, describing the main characteristics of the AMICO code. Then, the main properties of the catalogue are presented.
- In Chapter 6, we will show the results of this Thesis work, focusing on the evolution of the clustering signal both as a function of redshift and mass, providing constraints on cosmological parameters, on the effective bias, and on the parameters of the cluster scaling relation.
- In Chapter 7, we will summarise the main results of this Thesis work and discuss future perspectives.

# Chapter 1

## Cosmology

In this Chapter our aim is to present the cosmological scenario on which this dissertation is built on. At first, we introduce the fundamental mathematical structure of modern cosmological models, giving a brief overview on General Relativity Theory (Section 1.2) with the intent of presenting the Friedmann-Lemaître-Robertson-Walker metric (Section 1.3) and the Friedmann Equations (Section 1.4). Then, once we have provided the definition of redshift, Hubble Flow and distances, different Universe models will be illustrated. Finally, the main features of the currently adopted Standard Cosmological Model are described (Section 1.5).

### 1.1 Cosmological principle

The scientist Nicolaus Copernicus (1473-1543) recognised that Earth is not in any particularly privileged position in the solar system. This idea was extended in modern Cosmology where this principle states we do not occupy any special place in the Universe too. Therefore, it is reasonable to assume that the Universe would look to any other observers like it looks to us.

However, until the beginning of the 20th century, little was known about the distribution of matter in the Universe. For example, it was thought that the Milky Way was the entire cosmos. On the other hand, it was thought that on sufficiently large scales gravitational force becomes the predominant force governing nature, so it could be possible to describe the Universe through Einstein's General Theory of Relativity (Einstein, 1915). However, using *General Relativity* (GR) for an arbitrary distribution of matter was found to be impossible. Thus, simplified models had been developed to make progress in investigating the cosmos as a whole.

Indeed, for this purpose, the *Cosmological Principle* (CP) was introduced by Einstein even if there were not any observational evidence. The CP states that the cosmos is essentially homogeneous and isotropic, where *isotropy* is the property to look the same in every direction and *homogeneity* is the property of being identical everywhere in space.

On small scales, the Universe is clearly anisotropic and inhomogeneous, but current observations ensure indeed that the assumption of CP is correct for describing the Universe on sufficiently large scales. Thus, nowadays cosmologists define homogeneity and isotropy in an average sense: the Universe is isotropic and homogeneous on scales of 100Mpc or more (see Scrimgeour et al., 2012).

### 1.2 Fundamentals of General Relativity

Modern cosmology is based on two crucial assumptions: the CP is a good approximation for studying the Universe; the dominant interaction on cosmological scales is gravity, so cosmology is based on GR, being the best theory of gravity so far.

In Special Relativity (SR) the *interval* between two events at  $(t, x, y, z)$  and  $(t + dt, x + dx, y + dy, z + dz)$ , is defined as:

$$ds^2 = c^2 dt^2 - (dx^2 + dy^2 + dz^2) , \quad (1.1)$$

where  $ds^2$  is *invariant* under a change of coordinate system, by using the Lorentz transformations. The metric given in the Eq.(1.1) is called Minkowski metric and the spacetime that it describes is called *Minkowski spacetime* (Minkowski, 1908) that is *pseudo-Euclidean*, or *flat*. The path of a light ray is given by  $ds^2 = 0$ , that is the *null cone* in the Minkowski spacetime. The path of a particle under no external forces between any two events is  $\int_{path} ds^2$ , and this corresponds to the shortest distance between any two points, being a straight line in the Minkowski spacetime. From Eq.(1.1) we distinguish three types of interval: the interval may be time-like ( $ds^2 > 0$ ), space-like ( $ds^2 < 0$ ) or light-like ( $ds^2 = 0$ ). The action of a force causes particle tracks to deviate from the straight line. Eq.(1.1) applies only within the context of SR, in which spacetime is not curved by the presence of mass and energy.

GR is built up on *Differential Geometry* and all the equations are written in tensor form. Thanks to the *Principle of General Covariance*, or *Covariance Principle*, we can generalise the results obtained in SR to GR. Indeed, the Covariance Principle states that the laws of physics in a general reference frame are obtained from the laws of SR by replacing tensor quantities of the Lorentz group with tensor quantities of the spacetime manifold, described by Differential Geometry. The essence of Einstein's theory is to transform gravitation from being a force to being a property of spacetime, that is not necessarily flat but may be curved. In the context of GR, the geometry of *spacetime* is described by the *metric tensor*,  $g_{\mu\nu}$ . Then, the interval between two events in GR can be written as

$$ds^2 = g_{\mu\nu} dx^\mu dx^\nu, \quad (1.2)$$

where  $\mu, \nu$  both run from 0 to 3;  $x^0 = ct$  is the time coordinate,  $t$  is the *proper time*, and  $x^1, x^2, x^3$  are the space coordinates. We can explicitly re-write Eq.(1.2) as:

$$ds^2 = g_{00} dt^2 + 2g_{0\mu} dx^\mu dt + g_{\mu\nu} dx^\mu dx^\nu \quad (1.3)$$

where  $g_{00} dt^2$  is the time component,  $2g_{0\mu} dx^\mu dt$  is the mixed component and  $g_{\mu\nu} dx^\mu dx^\nu$  is the spatial one.

While  $g_{\mu\nu}$  describes the geometry of spacetime,  $ds^2$  tells us if the interval is time-like ( $ds^2 > 0$ ), space-like ( $ds^2 < 0$ ) or light-like ( $ds^2 = 0$ ), like in SR.

A particle moves along its path according to:

$$\int_{path} ds^2 = 0, \quad (1.4)$$

so the integral along the path is stationary but paths are no longer straight, like in the Minkowski spacetime. From Eq.(1.4), the path of a free particle, called *geodesic*, is described by

$$\frac{d^2 x^i}{ds^2} + \Gamma_{kl}^i \frac{dx^k}{ds} \frac{dx^l}{ds} = 0, \quad (1.5)$$

where  $\Gamma$ s are called *Christoffel symbols*, linked to the metric tensor by

$$\Gamma_{kl}^i = \frac{1}{2} g^{im} [g_{mk,l} + g_{ml,k} - g_{kl,m}],$$

using the covariant notation, while  $g^{im} g_{mk} = \delta_k^i$ , where  $\delta_k^i$  is the *Kronecker delta*. Thus, the metric  $g_{\mu\nu}$  determines the causal structure of spacetime by governing the propagation of light and of any other signal. The properties of curved spaces were well-known, thanks to the work done in differential geometry, while Einstein was developing his theory. For example, it was known that the Riemann-Christoffel tensor, defined as:

$$R_{kml}^i = \frac{\partial \Gamma_{km}^i}{\partial x^l} - \frac{\partial \Gamma_{kl}^i}{\partial x^m} + \Gamma_{nl}^i \Gamma_{km}^n - \Gamma_{nm}^i \Gamma_{kl}^n,$$

could be used to determine whether a given space is curved or flat because is linked with the intrinsic curvature of the manifold. From the Riemann-Christoffel tensor, the Ricci tensor and Ricci scalar are derived as:

$$R_{ik} = R_{ilk}^l, \\ R = g_k^i R_{ik}.$$

Both are used in the definition of the Einstein tensor:

$$G_{ik} \equiv R_{ik} - \frac{1}{2}g_{ik}R, \quad (1.6)$$

which is obviously symmetric and contains 10 independent components since the metric tensor is symmetric and contains (at most) 10 independent components. Moreover, the Einstein tensor is covariantly conserved and this propriety is expressed by the Bianchi identities:

$$\Delta_\mu G^\mu_\nu = 0.$$

The tensor  $G_{ik}$  contains at most second order partial differential equations, like in Maxwell's Equations. The key factor in GR is the relationship between the distribution of matter and the metric describing the spacetime geometry given by Eq.(1.6). To link the metric to the distribution of matter, we have to express the mass-energy of the *source* with the same mathematical properties: it must be described by a symmetric and covariantly conserved (0, 2) tensor built out of the matter-energy content of the system. One such tensor is the *energy-momentum tensor*, defined as:

$$T_{ik} = (p + \rho c^2) u_i u_k - p g_{ik},$$

for a perfect fluid with four-velocity  $u^\mu$ , characterised by density  $\rho$  and pressure  $p$ . An important property of fluids is the continuity equation that can be written in a fully covariant form as  $T^k_{i;k} = 0$  so, also energy-momentum tensor is covariantly conserved.

Within the *classical limit*, this equation must reduce to the *Poisson's equation* describing Newtonian gravity:

$$\Delta\phi = 4\pi G\rho, \quad (1.7)$$

in order to recover classical mechanics. so it should be linear in the second derivative of the metric.

Therefore, Einstein proposed as his fundamental equation

$$G_{ik} = \frac{8\pi G}{c^4} T_{ik}, \quad (1.8)$$

where the quantity  $8\pi G/c^4$  ensures that the Poisson's equation in its standard form (given in Eq.(1.7)) results in the limit of a weak gravitational field. According to the *Einstein Field Equations* (expressed in Eq.1.8), matter sources determine the spacetime curvature, which affects the motion of matter. Einstein Field Equations are 10 (with only 6 independent) partial differential equations, highly non-linear. Hence, unlike Newton's Law, the effect of two gravitational sources is not just their sum.

### 1.3 The Fridman-Lemaître-Robertson-Walker metric

The CP ensures that exists a time  $t$  such that the Universe is homogeneous and isotropic on each time slice  $\Sigma_t$ , that are sub-manifolds of the spacetime variety, i.e. hypersurfaces of constant time  $t$ . The matter content on each  $\Sigma_t$  then affects the light propagation.

Robertson, Walker, Lemaître and Friedmann assumed the CP in the 1920s and 1930s, long before the available observational evidence supporting this principle. As we said, it is a convenient assumption to solve the Einstein Field Equations for cosmological purposes because, under this assumption, the Universe can be described as a perfect fluid. For each fluid element are assigned the three spatial coordinates  $x^\alpha$  ( $\alpha = 1, 2, 3$ ), called *comoving coordinates*, and a time parameter. As time parameter is considered the *proper time*  $t$ , which is measured by a clock moving with the fluid element. The geometrical properties of spacetime, as we have discussed in Section 1.2, are described by a metric. Thanks to the assumption of isotropy, the mixed components  $g_{0\mu}$  of Eq.(1.3) have to be null. So, the general form for the metric is

$$ds^2 = c^2 dt^2 - g_{\mu\nu} dx^i dx^j = c^2 dt^2 - dl^2.$$

It can be shown that homogeneity and isotropy uniquely identify the Friedmann Lemaître Robertson Walker (FLRW) metric, that is expressed as

$$ds^2 = c^2 dt^2 - a(t)^2 \left[ \frac{dr^2}{1 - Kr^2} + r^2 (d\theta^2 + \sin^2 \theta d\phi^2) \right], \quad (1.9)$$

where we have used spherical polar coordinates:  $r$ ,  $\theta$  and  $\phi$  are the comoving coordinates and the origin  $r = 0$  is totally arbitrary;  $t$  is the *proper time* of an observer moving along with the homogeneous and isotropic cosmic fluid at  $r$ ,  $\theta$  and  $\phi$  constant;  $a(t)$  is called *cosmic scale factor*, or *expansion parameter*; the curvature parameter  $K$  is a constant. Usually,  $(d\theta^2 + \sin^2 \theta d\phi^2)$  is represented by  $d\Omega^2$ . The scale factor  $a(t)$  is a dimensionless function of time that describes how distances grow or decrease with time; it is generally normalised so that  $a(t_0) = 1$  at the present time. If the expansion of the Universe is perfectly homogeneous and isotropic, then the comoving coordinates of any point remain constant with time.

The parameter  $K$  could take any real value, however, if  $K \neq 0$ , it is possible re-scaling  $r$  and  $a$

$$\begin{aligned} dr &\rightarrow \sqrt{\pm K} dr \\ a^2 &\rightarrow K^2 a^2, \end{aligned}$$

and in this way  $K$  will only allow to be equal to 1, 0 or  $-1$ .

We can introduce new coordinates to describe the topology of the hypersurface  $\Sigma_t$ . This is apparent from the line element  $d\sigma$ , defining  $ds^2 = -dt^2 + a(t)^2 d\sigma^2$ :

- **Flat Universe** : for  $K = 0$  the coordinate  $r$  is very similar to the usual radial coordinate in  $\mathbf{R}^3$ ,

$$d\sigma^2 = dr^2 + r^2 d\Omega^2$$

and  $\Sigma_t$  is flat (zero spatial curvature);

- **Closed Universe** : for  $K = +1$  the proper radius  $R_{(3)}$  of the Universe is bounded and we have:

$$r = \sin(\chi) \Rightarrow d\sigma^2 = d\chi^2 + \sin^2(\chi) d\Omega^2$$

and  $\Sigma_t$  is a three-dimensional sphere;

- **Open Universe** : for  $k = -1$ , one can write

$$r = \sinh(\Psi) \Rightarrow d\sigma^2 = d\Psi^2 + \sinh^2(\Psi) d\Omega^2$$

and  $\Sigma_t$  is a three-dimensional hyperboloid.

### 1.3.1 Cosmological distances

The *proper distance* is defined as the distance measured by a chain of rulers linking an observer in  $P_0$  to  $P$  at time  $t$ . Supposing that  $P$  is observed from  $(0, 0, 0)$ , used to define the origin of a set of polar coordinates, and has comoving coordinates  $(r, \theta, \phi)$ , we can assume that along the radial geodesics, from the observer to  $P$ ,  $(\theta, \phi)$  are constant. Therefore, we can define the proper distance, when  $dt = 0$ , in the FLRW metric as:

$$d_p = \int_0^r \frac{a dr'}{(1 - Kr'^2)^{1/2}} = af(r) \quad (1.10)$$

where the function  $f(r)$  is, respectively:

$$\begin{aligned} f(r) = \sin^{-1} r &\iff K = 1 ; \\ f(r) = r &\iff K = 0 ; \\ f(r) = \sinh^{-1} r &\iff K = -1 . \end{aligned}$$

Because the proper distance depends on  $a(t)$ , its values changes in time. In other words, in an expanding Universe, the distance between two objects increases in time. Thus, we may

define the proper distance between two bodies only if we specified a time  $t$ . Of course this proper distance is of little *operational* significance because one can never measure simultaneously all the distance elements (rulers) separating  $P$  from  $P_0$  for the same time.

The proper distance at time  $t$  is related to that at the present time  $t_0$  by

$$d_c = d_p(t_0) \equiv a_0 f(r) = \frac{a_0}{a} d_p(t)$$

that is called *comoving distance*.

### 1.3.2 The Hubble-Lemaître Law

When we study the spectrum of a galaxy at visible wavelengths, it typically contains lines produced in the stellar atmospheres. Considering a particular line which wavelength as measured in a laboratory on Earth is  $\lambda_{em}$ , the wavelength we measure for the same line in a distant galaxy's spectrum  $\lambda_o$  will not, in general, be the same. We say that the galaxy has *redshift*  $z$ , given by the formula

$$z = \frac{\lambda_o - \lambda_e}{\lambda_e},$$

when  $z > 0$ . When  $z < 0$ , this quantity is called *blueshift*, rather than redshift.

By 1929, enough galaxy redshifts had been measured resulting that galaxies are generally redshifted. Edwin Hubble studying this data found the relation:

$$z = \frac{H_0}{c} r.$$

Hubble interpreted the observed redshift of galaxies as being a sort of Doppler shift due to their radial velocity away from Earth, (Hubble, 1929).

We have seen that the proper distance  $d_P$  of a source changes over time because of the time-dependence of the expansion parameter  $a$ . Thus, a source at  $P$  has a radial velocity with respect to the origin  $P_0$  given by

$$v_r = \dot{a} f(r) = \frac{\dot{a}}{a} d_P. \quad (1.11)$$

Eq.(1.11) is called the *Hubble-Lemaître law* and the quantity

$$H(t) \equiv \frac{\dot{a}}{a},$$

is called the *Hubble constant* or the Hubble parameter. The value of this parameter evaluated at the present time for our Universe,  $H(t_0) \equiv H_0$ , is not known to any great accuracy. It is believed, however, to have a value around  $H_0 \approx 70 \text{ km s}^{-1} \text{ Mpc}^{-1}$ ; for example in Riess et al. (2019) has been found  $H_0 = 74.24 \pm 1.82 \text{ km s}^{-1} \text{ Mpc}^{-1}$ .

It is conventional to take into account of the uncertainty in  $H_0$  by defining the dimensionless parameter  $h$ , so that  $H_0 \equiv h 100 \text{ km s}^{-1} \text{ Mpc}^{-1}$ . The global motion of objects in the Universe with respect to each other, given by the Universe explanation itself, is called the *Hubble Flow*.

$H_0$  also gives the Universe scale. Indeed, considering a galaxy in  $r$ , with a leaving speed  $v_0$  at  $t_0$ , we have

$$v_0 = H_0 r \quad \longrightarrow \quad t_0 = \frac{r}{v} = \frac{r}{H_0 r} = H_0^{-1}$$

so, using this law over reversing time, we can find the moment in which the galaxies are nearest and so an approximated estimate of the current age of the Universe. Hubble found out  $H_0 \sim 500 \frac{\text{km/s}}{\text{Mpc}}$  so  $H_0^{-1} \sim 10^9 \text{ yr}$ . Nowadays, the age of the Universe is considered to be around 13.8Gyr (see results obtained in Aghanim et al., 2018a).

### 1.3.3 The cosmological redshift and the scale factor

The redshift  $z$  is related to the scale factor  $a$  and it is used in describing the evolution of the Universe. Consider the radiation wavelength emitted  $\lambda_{em}$  by the source and observed as  $\lambda_o$ . The

radiation travels along a light ray (null geodesic) from the source to the observer so that  $ds^2 = 0$  and, therefore, from Eq.(1.10), we can write:

$$\int_{t_e}^{t_o} \frac{c dt}{a(t)} = \int_0^r \frac{dr}{(1 - Kr^2)^{1/2}} = f(r), \quad (1.12)$$

Light emitted from the source at  $t'_e = t_e + \delta t_e$  reaches the observer at  $t'_o = t_o + \delta t_o$ . Since  $f(r)$  does not change, because  $r$  is a comoving coordinate and both the source and the observer are moving with the cosmological expansion, we can write:

$$\int_{t'_e}^{t'_o} \frac{c dt}{a(t)} = f(r). \quad (1.13)$$

If  $\delta t$ , and therefore  $\delta t_o$  are sufficiently small, Eqs.(1.12)-(1.13) imply that

$$\frac{\delta t_o}{a_0} = \frac{\delta t}{a}$$

If, in particular,  $\delta t = 1/\nu_e$  and  $\delta t_o = 1/\nu_o$ , where  $\nu_e$  and  $\nu_o$  are the frequencies of the emitted and observed light, we have  $\nu_e a = \nu_o a_0$  equivalent to

$$\frac{a}{\lambda_e} = \frac{a_0}{\lambda_o}.$$

Hence, we can relate the cosmological redshift with the scale factor, thanks to the following equation:

$$1 + z = \frac{a_0}{a}. \quad (1.14)$$

This equation links an observable quantity,  $z$ , to the expansion of the Universe and tell us that  $z$  increases when we go back in time, which is a measure both for the distance and the time of the observed object. It is important to underline that the cosmological redshift is not a Doppler effect: it is led by the expansion of the Universe, instead of a motion of the source. The expansion of the Universe leads to

$$\lambda(t) \propto a(t), \quad \nu(t) \propto a(t)^{-1}, \quad v_p \propto a(t)^{-1}.$$

### 1.3.4 Distance measures

As we said,  $d_p$  and  $d_c$  cannot be used to estimate a distance because  $a(t)$  it is not constant in time. Other definitions are introduced for measuring distance through astrophysical observables.

For example, distant objects are observed through their luminosity and we know that their emission arrives to us in a limited amount of time. Thus, we can measure their emission inside our past light cone. The link between the energy flux we measure,  $l$ , and the source intrinsic luminosity,  $L$ , is

$$l = \frac{L}{4\pi d_L^2},$$

where  $d_L$  is called *luminosity distance*. We have also to take into account both cosmological redshift and time dilatation, so we have

$$l = \frac{L}{4\pi a_0 r} \left( \frac{a_0}{a} \right)^2$$

because, for the time dilatation, we have  $\delta t_o = (a_0/a)\delta t$ , while for the cosmological redshift a factor  $(a_0/a)$  has to be counted. Using Eq.(1.14), we obtain the definition of luminosity distance:

$$d_L = a_0 r (1 + z)$$

that is commonly used to measure distances using *standard candles*, generally type Ia supernovae.

Another classic measure of distance in cosmology is the angular one,  $d_A$ . We see an object of proper angular dimension  $D_{pr}(z)$  at redshift  $z$  as  $d_A$  under an angle  $\delta\theta$

$$d_A(z) = \frac{D_{pr}(z)}{\delta\theta}, \quad (1.15)$$

where  $D_{pr} = a(t)r d\theta$ , assuming a flat space in Eq.(1.9). This quantity is then connected to  $d_L$  through the *duality relation*:

$$d_A = a(t)r = \frac{d_L}{(1+z)^2}$$

which is commonly used to derive distance with *standard rulers*, nowadays in the context of baryonic acoustic oscillations (introduced below, in Section 2.4.3).

## 1.4 Friedmann Equations

Assuming the CP and describing the Universe as a perfect fluid, it is possible to find solutions for Einstein Field Equations (Eq.1.8), in which the FLRW metric is used to define  $g_{ij}$ , while  $T_{ij}$  describe the perfect fluid. Thanks to these assumption, from Eq.(1.8), we obtain only two linear independent equations, called *Friedmann Equations* (Friedmann, 1922):

1. time-time component

$$\ddot{a} = -\frac{4\pi G}{3} \left( \rho + \frac{3p}{c^2} \right) a; \quad (1.16)$$

2. space-space component

$$\dot{a}^2 + kc^2 = \frac{8\pi G}{3} \rho a^2. \quad (1.17)$$

These two equations are linked by the adiabatic condition

$$d(\rho c^2 a^3) = -p da^2 \quad (1.18)$$

that means the Universe is expanding without energy loss, that is an obvious assumption because the Universe is a closed system.

Friedmann Equations have been obtained in 1922, when the Universe was commonly considered static. However, these equations are dynamical ones. For a static Universe we must have:

$$\ddot{a} = \dot{a} = 0,$$

that implies

$$\rho = -\frac{3p}{c}.$$

Thus, pressure or density has to be a negative quantity that is a *non-physical* solution.

### 1.4.1 Einstein's Static Universe

In 1917, to derive a cosmological model from Eq.(1.8), Einstein made different assumptions. Firstly, as we said in Section 1.1, he introduced the CP. Then, he assumed the Universe had a closed spatial geometry with uniform positive curvature, so a finite volume but without edges or boundaries (to be consistent with the CP assumption). The last assumption was that the Universe is static and its large-scale properties do not vary with time. The CP assumption in addition to the idea of stationarity over time is called *Perfect Cosmological Principle*. On this principle during 1950s is set up the *steady-state theory*, introduced by Hermann Bondi, Fred Hoyle, and Thomas Gold, that coexisted with the *Big Bang Theory* till the Cosmic Microwave Background (CMB) was observed for the first time in 1964, that was predicted in the Big Bang Theory but impossible to explain within the steady-state model.

With these assumptions, it is possible obtain solutions to the Einstein Field Equations but without physical meaning because pressure or density of the isotropic and homogeneous fluid describing the Universe has to be negative. To obtain a physical solution, Einstein added to

the equations an extra-term, called the *cosmological constant*. Thus, Einstein proposed the alternative form for Eq.(1.8), as:

$$G_{ik} \equiv R_{ik} - \frac{1}{2}g_{ik}R - \Lambda g_{ik} = \frac{8\pi G}{c^4}T_{ik}, \quad (1.19)$$

where the cosmological constant could be interpreted as a sort of repulsive force keeping the matter from moving because its action is contrasting the attractive pull of gravity. Moreover, the inclusion of a cosmological constant means that the Universe also in the absence of any mass-energy (*standard*) source would not be flat.

### Cosmological constant

Assuming an Universe with a cosmological constant, the energy-impulse tensor can be defined as:

$$\tilde{T}_{ij} = T_{ij} + g_{ij} \frac{c^4}{8\pi G} \Lambda.$$

Thus, we can re-write the Eq.(1.19) as

$$R_{ij} - \frac{1}{2}g_{ij}R = \frac{8\pi G}{c^4}\tilde{T}_{ij}$$

Defining the effective pressure and the effective density as follows:

$$\begin{aligned} p_{eff} = \tilde{p} &= p + p_\Lambda = p - \frac{c^4}{8\pi G}\Lambda, \\ \rho_{eff} = \tilde{\rho} &= \rho + \rho_\Lambda = \rho + \frac{c^4}{8\pi G}\Lambda, \end{aligned} \quad (1.20)$$

we can express  $\tilde{T}_{ij}$  as

$$\tilde{T}_{ij} = T_{ij} + g_{ij} \frac{c^4}{8\pi G} \Lambda = -\tilde{p}g_{ij} + (\tilde{p} + \tilde{\rho}c^2) U_i U_j$$

and the Friedmann Equations become

$$\begin{cases} \ddot{a} = -\frac{4\pi G}{3} \left( \tilde{\rho} + \frac{3\tilde{p}}{c} \right) a \\ \dot{a}^2 - kc = \frac{8\pi G}{3} \tilde{\rho} a^2 \end{cases}$$

wich define the characteristics of the Einstein's Universe, assumed static and with negligible pressure (*dusty*). In this scenario, Friedmann Equations lead to

$$\begin{cases} \Lambda = \frac{k}{a^2} \\ \rho = \frac{kc^2}{4\pi G a^2}. \end{cases}$$

We have, as assumption,  $p = 0$ , so, to have  $\rho > 0$  the only possible geometry is  $K = +1$  and this means that, for having a static Universe with  $\Lambda$ , the only solution is considering a spherical Universe. When Edwin Hubble discovered the expansion of the Universe, static model were abandoned but models with  $\Lambda$  have been reintroduced at the end of the 20th century to describe the observed accelerated expansion of the Universe. Nowadays, the origin of this repulsive action is commonly assigned to the Dark Energy, capable to explain the accelerated expansion of the Universe. Indeed, for example, in the De Sitter Model, the presence of  $\Lambda$  causes an accelerated expansion.

### De Sitter Universe

The so-called de Sitter Model assumes an empty ( $p = 0$  and  $\rho = 0$ ) and flat Universe ( $K = 0$ ) but with  $\Lambda$ . These assumptions lead to  $\tilde{p} = -c^2\tilde{\rho}$  and from Friedmann Equations, we have:

$$\frac{\dot{a}}{a} = \frac{d \ln a}{dt} = \sqrt{\frac{\Lambda}{3}} c$$

$$\begin{aligned}\Rightarrow a &\propto e^{\sqrt{\frac{4}{3}}ct} \\ \Rightarrow \ddot{a} &> 0.\end{aligned}$$

Therefore these assumptions imply a Universe in accelerated expansion.

### 1.4.2 Friedmann Models

In Friedmann models, the Universe is considered as a perfect fluid. Thus, to describe the Universe solving the Friedmann Equations (Eq.1.16-1.17), it is necessary to understand the relation between density,  $\rho$ , and pressure,  $p$ , that means to specify the *Equation of State* (EoS), which could be expressed in the general form:

$$p = w\rho c^2, \quad (1.21)$$

where  $w$  is defined so that the sound speed is:

$$c_s \equiv \left( \frac{\partial p}{\partial \rho} \right)_{s=const}^{1/2} = c\sqrt{w} \quad (1.22)$$

where  $S$  represents the entropy. The value of  $w$  changes with the type of the fluid composing the Universe:

- if we consider a fluid composed by non-relativistic ordinary matter, the relation between  $\rho$  and  $p$  is given by

$$p = nk_b T, \quad (1.23)$$

and this pressure may be neglected (*dust Universe*) so we can consider  $w = 0$ ;

- if we consider a fluid composed by relativistic ordinary matter, so a relativistic or ultra-relativistic fluid, the EoS is

$$p = \frac{1}{3}\rho c^2,$$

so, for the relativistic matter, for example a gas of photons, we have  $w = 1/3$ ;

- for the cosmological constant, we have  $w = -1$ , as described in Section 1.20.

Considering the speed of sound, given by Eq.(1.22), we have  $0 \leq w < 1$ , called *Zel'dovich interval*, indeed, for  $w < 0$ ,  $c_s$  would be imaginary, while, for  $w \geq 1$ ,  $c_s$  would be larger than the speed of light  $c$ .

Substituting in the EoS the adiabatic condition, expressed in Eq.(1.18), we obtain:

$$\rho_w = \rho_{0,w} \left( \frac{a}{a_0} \right)^{-3(1+w)}, \quad (1.24)$$

which describes how the densities of the different components of the fluid vary over cosmic time (see Fig.1.1). In fact, from Eq.(1.24), we obtain the following relations:

- for the matter component:  $w = 0, \quad \rho_{mat} = \rho_{0,mat} \left( \frac{a}{a_0} \right)^{-3} = \rho_{0,mat} (1+z)^3$
- for the relativistic component:  $w = 1/3, \quad \rho_{rel} = \rho_{0,rel} \left( \frac{a}{a_0} \right)^{-4} = \rho_{0,rel} (1+z)^4$
- for the exotic component:  $w = -1, \quad \rho_{\Lambda} = \rho_{0,\Lambda} \left( \frac{a}{a_0} \right)^0 = \rho_{0,\Lambda}$

### 1.4.3 Flat, open and closed Universes

The Friedmann Models are based on:

- Friedmann Equations, Eq.(1.16-1.17);
- Adiabatic condition, Eq.(1.18);

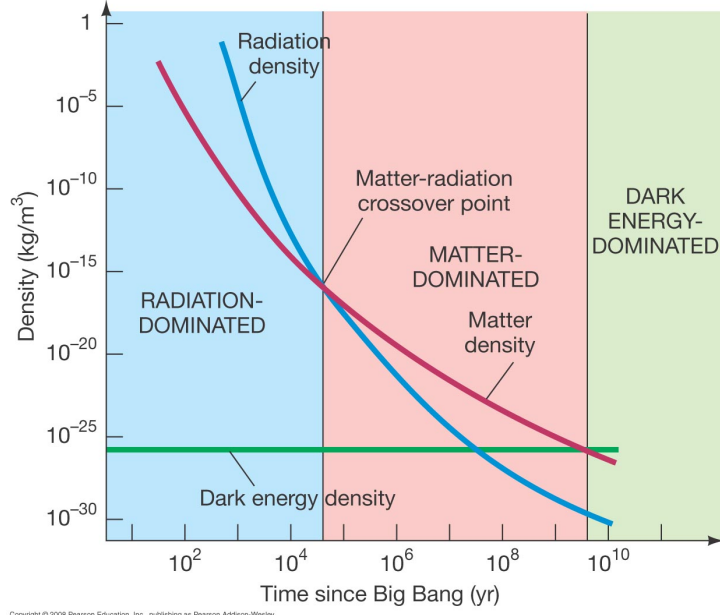


**Figure 1.1:** The density as a function of time, showing how the dominant component changes over cosmic time, that currently is dark energy density. In the Early Universe, till the time of *equivalence*  $t_{eq}$  between radiation and matter, radiation was the dominant component. After that moment, radiation became negligible and the matter was the dominant component till the equivalence moment between matter and dark energy. Credits to: Pearson (2018)

- Fundamental definitions, such as the definition of the *critical density*:

$$\rho_{crit}(t) \equiv \frac{3H^2}{8\pi G} \quad (1.25)$$

the *density parameter*:

$$\Omega \equiv \frac{\rho}{\rho_{crit}} \quad (1.26)$$

the *deceleration parameter*:

$$q(t) \equiv -\frac{\ddot{a}(t) a(t)}{\dot{a}(t)^2} \quad (1.27)$$

and the definitions of the Hubble parameter (Eq.1.11) and the redshift (Eq.1.14).

In order to show how the critical density is the density requested for having a flat Universe ( $K = 0$ ), the Second Friedmann Equation can be re-written as:

$$\frac{K}{a^2} = \frac{1}{c^2} \left( \frac{\dot{a}}{a} \right)^2 \left( \frac{\rho}{\rho_c} - 1 \right), \quad (1.28)$$

and assuming different geometry we have, at  $z = 0$ :

- flat Universe:  $K = 0 \rightarrow \rho_0 = \rho_{0,crit} \rightarrow \Omega_0 = 1$
- spherical Universe:  $K = 1 \rightarrow \rho_0 > \rho_{0,crit} \rightarrow \Omega_0 > 1$
- hyperspherical Universe:  $K = -1 \rightarrow \rho_0 < \rho_{0,crit} \rightarrow \Omega_0 < 1$

We can also re-write the Second Friedmann Equation as:

$$H^2(z) = H_0^2(1+z)^2 \left[ 1 - \sum \Omega_{o,w_i} + \sum_i \Omega_{o,w_i}(1+z)^{1+3w_i} \right] \quad (1.29)$$

where  $H(z)$  is the Hubble parameter at a generic redshift. The total density parameter is defined as the sum over all the components, that is  $\Omega_{TOT} = \sum_i \Omega_{w_i}$ . Of course, for  $\Omega_{TOT} = 1$

we have a flat Universe, while, for  $\Omega < 1$  and  $\Omega > 1$ , we have, respectively, an open Universe and a closed one.

We have already noticed that during the cosmic time, different components (matter, radiation and  $\Lambda$ ) become dominant. Notably, we can assume the Universe is entirely composed by only one type of fluid at any time, as long as we are sufficiently far from equivalence moment, with the exception of the present epoch, when  $\Omega\Lambda \approx \Omega_M$ .

#### 1.4.4 The Big Bang

Assuming both the First Friedmann Equation, Eq.(1.16) and the EoS (Eq.1.21), we can write:

$$\ddot{a} = -\frac{4\pi G}{3} (1 + 3w) \rho a ,$$

so, for  $(1 + 3w) > 0$  and  $w > -1/3$  (always true assuming the Zel'dovich interval), we have  $\ddot{a} < 0$ . While, given the positivity of  $H(t)$ , defined in Eq.(1.11),  $\dot{a} > 0$ . Therefore, the Universe is in a decelerating expansion and going back through cosmic time there would be a moment in which  $a(t) = 0$ , called *Big Bang* (BB). The BB is not avoidable in a model of Universe based on Friedmann Equations with  $w$  inside the Zel'dovich interval.

#### The Einstein-de Sitter Model

The Einstein-de Sitter (EdS) Model is the solution for the Friedmann Equations for a flat and mono-component Universe ( $k = 0$  and  $\Omega_{0,w} = 1$ ). These assumptions for solving Friedmann Equations lead to useful dependencies, summarised in Table 1.1.

**Table 1.1:** Dependencies obtained for the EdS Universe in three different cases: for a generic component (with EoS parameter  $w$ , first column), for a matter- dominated Universe, (with  $w = 0$ , second column) and for a radiation dominated Universe (with  $w = 1/3$ , third column)

$w$	$w = 0$	$w = 1/3$
$t = t_0(1+z)^{-\frac{3(1+w)}{2}}$	$t \propto (1+z)^{-3/2}$	$t \propto (1+z)^{-2}$
$a(t) = a_0 \left(\frac{t}{t_0}\right)^{\frac{2}{3(1+w)}}$	$a(t) \propto t^{2/3}$	$a(t) \propto t^{1/2}$
$H(t) = \frac{2}{3(1+w)t}$	$H(t) = \frac{2}{3t}$	$H(t) = \frac{1}{2t}$
$\rho = \frac{1}{6\pi G(1+w)^2} \frac{1}{2}$	$\rho = \frac{1}{6\pi G} \frac{1}{2}$	$\rho = \frac{3}{32\pi G} \frac{1}{t^2}$

#### Curved Universe

Considering a mono-component and curved Universe ( $K \neq 0$ ,  $\Omega_0 \neq 1$ ), Eq.(1.29) giveso:

$$\left(\frac{\dot{a}}{a_0}\right)^2 = H_0^2 \left[ (1 - \Omega_0) + \Omega_0, \left(\frac{a_0}{a}\right)^{1+3w} \right] \quad (1.30)$$

where

- $(1 - \Omega_0) = A$  is constant and describes the Universe curvature;
- $\Omega_0 \left(\frac{a_0}{a}\right)^{1+3w} = B$  decreases when  $a$  increases, because  $(1 + 3w)$  is always positive, assuming the Zel'dovich interval.

When  $a \rightarrow 0$ ,  $B$  becomes more important than  $A$ , that means the EdS solutions describe young Universes of any geometry, because, in a young Universe, it is indeed possible not to consider at all the curvature.

On the other hand, we have to consider the curvature of the Universe when  $A \geq B$ . However, considering acceptable values for  $\Omega_0$ , the Universe has an EdS behaviour for a long period during its evolution, till  $z^* \sim 10$ .

We have two different kinds of curved Universe :

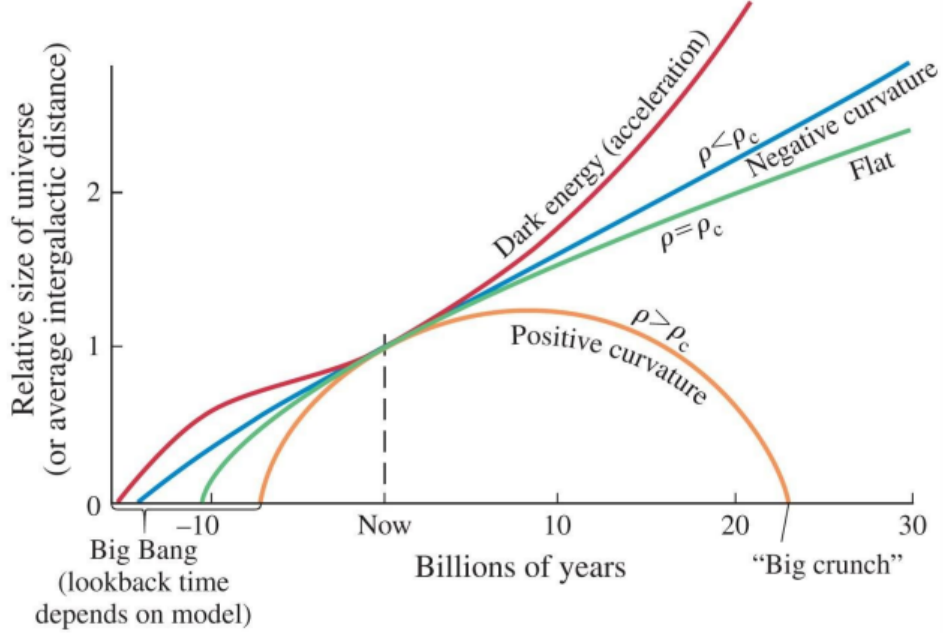


**Figure 1.2:** Evolution of the scale factor over the cosmic time for different assumption: closed Universe with  $\rho < \rho_c$  (yellow line) ending up collapsing in a second singularity (Big Crunch); flat Universe with  $\rho = \rho_c$  (green line); open Universe (blue line) with  $\rho < \rho_c$  ending up in a Big Freeze (heat death); Universe with  $\Lambda$  (red line), as assumed in  $\Lambda$ CDM model. Credits to: Trentham (2005)

- If we consider a hyperbolic Universe ( $\Omega_0 < 1$ ), from Eq.(1.30), if  $z \ll z^*$ , implies that the B term is negligible, so that:

$$\dot{a} \sim a_0 H_0 (1 - \Omega_0)^{1/2}$$

which means  $a \propto t$ ,  $H \propto 1/t$  and  $q \rightarrow 0$ .

Hence, the Universe expansion is free and non-decelerated (see Fig.1.2). Thus, the Universe expands with a constant rate leading to the *Big Freeze*, that is the thermal death of the Universe.

- If we consider a spherical Universe ( $\Omega_0 > 1$ ), from Eq.(1.30), at  $z \ll z^*$ , we have a quadratic equation. Thus, we can defined  $t_{max}$ , that is the moment in which the maximum for  $a(t)$  is reached, after an increasing period. Then, in a symmetric way,  $a(t)$  decreases and the Universe will end up collapsing in a second singularity called *Big Crunch* (see Fig.1.2).

We define  $a_{max}$  for  $\dot{a}(t_{max}) = 0$ :

$$a_{max} = a_0 \left( \frac{\Omega_0}{\Omega_0 - 1} \right)^{1/3w+1},$$

so, at the maximum radius we have the minimum density of the Universe during its evolution.

## 1.5 The Standard Cosmological Model

The standard *Big Bang* (BB) Model is obtained by solving the Friedmann Equations and it was largely accepted by scientists because its predictions could be verified through observations. In particular, the BB theory is able to explain a huge variety of phenomena, such as the Hubble Flow and the abundance of light elements. Notably, unlike other cosmological models, the Big Bang one predicts the existence of the CMB. In fact, when for the first time the CMB was detected (1964), the other models were abandoned. With the BB theory it is possible to describe the entire evolution of the cosmos, from the Planck time, the first moment in the Universe history in which our physical models are able to describe the matter structure and interactions, up today.

However, the BB theory had some open problems (we will discuss about these problems in the next Chapter, Section 2.1) solved by the *Inflation*, and it has been necessary to add the presence of the *Dark Energy* (DE) to explain the accelerated expansion observed today.

The currently accepted cosmological model is the  $\Lambda$ CDM, set up on the Big Bang Model, which can explain the large scale structures formation and evolution (described in Chapter 2) and the present accelerated expansion, introducing the cosmological constant as the dominant component at present time (see Fig. 1.1). The idea of the cosmological constant, as we discussed previously, was initially introduced by Einstein in order to obtain a static Universe with physical solutions, but, after the discover of the Universe expansion by Hubble, this addition to the Einstein Field Equations was abandoned. Only recently, in the 1990s, after the observation of the accelerated expansion of the Universe, thanks to the measurement of Supernovae (SNIa), used as standard candles (Riess et al., 1998), the  $\Lambda$  factor was re-introduced in the cosmological model, this time account for the acceleration in the Universe expansion.

In the  $\Lambda$ CDM model, the matter component is divided in two main types: baryonic matter and non-baryonic matter, distinguished by their interactions. Both baryonic and non-baryonic matter interact through gravitation, but only the baryonic one has also electromagnetic interactions. For its lack of electromagnetic interaction the non-baryonic matter is called *Dark Matter* (DM). Therefore, while the baryonic matter can be directly observed through standard observations based on the light emissions, the dark matter cannot be studied in this way. However, there are strong evidences of its existence.

In fact, its existence was for the first time inferred by Zwicky in 1933 through dynamical studies on the Coma galaxy cluster (Zwicky, 1933). He referred for the first time to this type of matter as DM. After this first indirect measurement, more and more DM evidences have been found on dynamical studies (e.g by measuring the rotation curves in late-type galaxies (Fuchs, 2001); or the velocity dispersion in early-type galaxy (Loewenstein et al., 1998) but also on gravitational lensing (e.g Li et al., 2016). However, despite the different ways to indirectly study the DM, the issue is to understand its nature. A huge list of DM particle candidates have been tested so far. In particular, these particle candidates were initially divided in two main typologies:

- Gravitationally-interacting massive particles (GIMPs): this type of particles are been excluded because, being massive, light emissions from them are expected;
- Weakly Interacting Massive Particles (WIMPs), such as axions and neutrinos: this type of particles can be further divided in relativistic particles (Hot DM (HDM)) and non-relativistic ones (Cold DM (CDM)), leading to different structure formation and evolution scenario, as we explained in Section 2.1.

Also Massive Astrophysical Compact Halo Objects (MACHOs) have been proposed as DM candidates, such as neutron stars, brown and white dwarfs because these structures are extremely massive and their light emission is negligible. However, theoretical works that MACHOs are not likely to account for the large amounts of dark matter now thought to be present in the Universe (e.g. Freese et al., 2000)

Actually, another possible alternative is to try to avoid the problem of the nature of the DM modifying the GR model, so, explaining this *mass excess* through the gravitation itself (a review on modified gravity models is given in Joyce et al., 2016).

The  $\Lambda$ CDM scenario is based on the existence of the dark matter component as Cold Dark Matter. Notably, the theory of structures formation is entirely explained thanks to this type of matter (illustrated in the following Chapter, in particular in Section (2.4.3)).

Currently, the  $\Lambda$ CDM model is broadly accepted because is capable to illustrate the formation end evolution of structures from the first seed after the Inflation Era (see Section 2.1). Moreover, the thermal evolution of the Universe, the particle formation and the accelerated expansion from the time of the equivalence between matter and  $\Lambda$  ( $z \approx 0.7$ , leading to the presence of a inflection point in the evolution of the scale factor at  $z_f \approx 0.3$ ) are explained.

## Chapter 2

# Formation and evolution of cosmic structures

In this Chapter we start introducing cosmic inflation and its importance in solving the open problems in the standard BB Theory. Then, we introduce the Jeans gravitational instability theory on which the cosmological structure formation theory is based. Finally, we describe the power spectrum of density fluctuations as a fundamental observable characterising the perturbation growth.

### 2.1 Cosmic Inflation

In our understanding of structure formation during the Universe evolution, a key element is the so-called *cosmic inflation*. In fact, the standard Big Bang scenario has some issues that can be solved by introducing an initial inflation (Guth, 1981). Moreover, the inflationary model leads to new predictions that could be tested. One of such open problems is the *horizon problem*: as already discussed in Chapter 1, the Universe appears statistically uniform on large scale, indeed the CMB temperature is almost the same across the whole sky. However, regions at distance larger than the cosmological horizon (see Section 2.3.1), cannot be in causal contact, due to the finite speed of light. Another open problem is called *flatness problem*, or *oldness problem* that is a cosmological fine-tuning problem: the Universe, to be as old as it appears, must be characterised by a density close to the critical value, Eq.(1.26) over all the cosmic time. Also small deviations from this value in its initial density would have strong effects on its evolution: an open Universe leads to a rapid cooling of the Universe while a closed Universe is characterised by a Big Crunch soon after the Big Bang. The flatness problem is so a fine-tuning problem because the only value that explains the age of our Universe is  $\Omega = 1$ , while  $\Omega$ , according to its definition, can assume all the real value. Finally, in the BB theory also predicts the existence of *magnetic monopoles*, that have never been observed. Indeed, the lack of magnetic monopoles is in contradiction with the Grand Unified Theory, which unifies electromagnetic, strong and weak interactions. This theory predicts magnetic monopoles characterised by the same abundance as protons in the early Universe, thus, according to this theory, it is expected to observe monopoles today.

To solve these problems, an accelerated evolutionary period has been introduced in the standard Big Bang scenario, called *Inflationary Era*, between  $10^{-33}$  to  $10^{-30}$  s after the Big Bang, driven by a negative-pressure vacuum energy of a scalar field, generally called *inflaton*. In this period, the Universe volume has expanded by a factor of  $\sim 10^{78}$ . This means that the whole observable Universe is originated from a small causally-connected region, and then its expansion in size has happened in a very small amount of time. During the Inflation Era, the Universe expanded in such a way that the homogeneity is preserved on the largest observable scales, justifying the smooth temperature distribution of the CMB. Moreover, its expansion is such that the Universe geometry is forced to be flat. Additionally, despite the huge number of magnetic monopoles in the early Universe, the possibility to observe them is negligible in such an expanded Universe.

Therefore, Inflationary Era sets the initial conditions of the Universe, providing also an explanation of the open problems within the standard BB Theory. Furthermore, this Inflationary Theory predicts fluctuations at the end of the cosmic inflation period, caused by the inflaton decay, that are supposed to be the seeds of the cosmic structures we observe in the local Universe.

## 2.2 The Jeans Theory

The cosmological model of structure formation is based on the Jeans gravitational instability theory (Jeans, 1902), originally developed to explain how stars and planets are formed from clouds of gas. This theory describes how small perturbations in density and velocity can occur and evolve over time, in a static, homogeneous and isotropic background fluid. The Jeans Theory is set up on the idea that the formation of structures is a consequence of gravitational instabilities. In particular, if the pressure is negligible, an overdense region tends to become denser because it attracts material from the surroundings regions, and finally collapses into a gravitationally bound system.

When the Jeans Theory is used in cosmology to explain structure formation and evolution, it is necessary to take into account that the gravitational collapse is hampered not only by the internal pressure of the structure itself, but also by the expansion of the Universe .

### 2.2.1 Jeans scale

The Jeans Theory assumes that there are two main processes in competition: the internal pressure and the gravitational force. The general idea is that a collapse is possible when the structure dimension is larger than the Jeans scale, defined as the structure size such that the two processes in competition are in equilibrium. When a perturbation is characterised by a length larger than the Jeans scale, the gravitation becomes dominant triggering the collapse of the structure.

We can calculate qualitatively the Jeans scale in different simple ways. We will consider a spherical perturbation with mass  $M$ , radius  $R$  and density  $\rho$ :

- The energy terms involved in the process are the gravitational potential energy,  $E_g = -GM\rho R^2$ , which leads to the aggregation of matter, and the kinetic energy of its particles,  $E_k = -\frac{1}{2}Mv^2$ , that contrasts the collapse, where  $v$  is the typical velocity of the particles, as the sound one  $c_s$ . Equating the two terms, we can define the Jeans scale as

$$R_J = v\sqrt{\frac{1}{2G\rho}};$$

- Considering the forces acting in the process, we have to take into account the gravitational force  $F_g = GM/R^2$  and the pressure force  $F_p = pR^2/M$ . The speed of sound is defined as  $c_s \approx P/\rho$ . Therefore, equalising the two terms, the Jeans scale is given by:

$$R_J = \frac{c_s}{\sqrt{G\rho}}$$

- The typical time scales involved are the *free-fall time*  $\tau_{FF} \propto 1/G\rho$  and also the *crossing-time*  $\tau_{cross} = 2R/c_s$ .

Thus, the scales obtained with these three approximate methods leads to  $R_J \propto \sqrt{\rho}$ . We can associate to these scales a mass as:

$$M_J \propto \rho R_J^3,$$

which is called *Jeans mass*, that is the critical mass above which gravity dominates.

### 2.2.2 The Jeans Theory in static Universes

Assuming the Universe as a perfect fluid, we can characterised it by its density  $\rho$ , pressure  $p$ , velocity  $\vec{v}$ , gravitational potential  $\phi$  and entropy  $S$ , through the following *hydrodynamic equations*

$$\begin{cases} \frac{\partial \rho}{\partial t} + \nabla \cdot (\rho \vec{v}) = 0 & \text{Mass conservation} \\ \frac{\partial \vec{v}}{\partial t} + (\vec{v} \cdot \nabla) \vec{v} = -\frac{1}{\rho} \nabla p - \nabla \phi & \text{Euler's Equation} \\ \Delta \phi = 4\pi G \rho & \text{Poisson's Equation} \\ p = p(\rho, S) & \text{Equation of state} \\ \frac{dS}{dt} = f & \text{Entropy equation} \end{cases} \quad (2.1)$$

If we consider adiabatic perturbations, we have  $S = \text{const}$  and  $p = p(\rho)$ , the system (2.1) reduces to four equations in four variables.

To obtain solutions for Eqs.(2.1) in the perturbed scenario, we will use the so-called *perturbation theory*. At first, a known solution to the *unperturbed problem* will be assumed. Then, a small perturbation is added, in order to study the time evolution of the system. In the linear perturbation theory, the added perturbations are small ( $\delta x \ll 1$ ). We are going to follow this approach.

Therefore, we start assuming the solution to Eqs.(2.1):

$$\begin{cases} \rho = \text{const} = \rho_B \\ \phi = \text{const} = \phi_B \\ v = 0 \\ p = \text{const} = p_B, \end{cases} \quad (2.2)$$

called *background solution*. Now, we add a small perturbation to the background solution, Eq.(2.2), obtaining the *perturbed solution* as follows:

$$\begin{cases} \rho = \rho_B + \delta \rho \\ \phi = \phi_B + \delta \phi \\ v = \delta v \\ p = p_B + \delta p \end{cases} \quad (2.3)$$

Since the perturbations are small, all second-order terms can be neglected. Using the perturbed solutions, Eq.(2.3), in Eq.(2.1), we obtain the so-called *perturbed hydrodynamics equations*:

$$\begin{cases} \frac{\partial \delta \rho}{\partial t} + \rho_B \nabla \cdot \delta \vec{v} & \text{Perturbed mass conservation equation} \\ \frac{\partial \delta \vec{v}}{\partial t} = -\frac{c_s^2}{\rho_B} \nabla \delta \rho + \nabla \delta \phi & \text{Perturbed Euler's Equation} \\ \Delta \delta \phi = 4\pi G \delta \rho & \text{Perturbed Laplace's Equation} \end{cases} \quad (2.4)$$

Finally, we look for solutions to the system (2.4) as *plane waves*

$$f(\vec{r}, t) = f_k \exp \left[ i \vec{k} \cdot \vec{r} + i \omega t \right], \quad (2.5)$$

where  $\vec{r}$  is the spatial vector,  $f_k$  is the wave amplitude,  $k$  is the wave number,  $\vec{k} = 2\pi \hat{k} / \lambda$  is the wave vector,  $\hat{k}$  is the wave versor and  $\omega$  is the angular frequency. Defining the *density contrast* as:

$$\delta_k = \frac{\delta \rho_k}{\rho_B} \quad (2.6)$$

we have

$$\delta(\vec{r}, t) = \delta_k \exp \left[ i \vec{k} \cdot \vec{r} + i \omega t \right]. \quad (2.7)$$

We could have also written similar equations for the other quantities but we are interested in the evolution of density perturbations.

Assuming the solutions as plane waves, we can move from the *real space* to the *Fourier space*, through Fourier transforms. In order to find the solutions for the perturbed system (Eqs.2.4) in

the *phase space*, we can set the determinant of the representative matrix of the system to zero. In this way we find a *dispersion's relation*

$$\omega^2 = k^2 c_s^2 - 4\pi G \rho_B \quad (2.8)$$

which links the wave pulsation to the speed of sound  $c_s$ , the wave vector  $k$  and the background density  $\rho_B$ . This equation has two possible solutions, depending on the sign of  $\omega^2$ , which discriminates between real and imaginary solutions. Setting  $\omega^2 = 0$  and solving for  $|\vec{k}|$  we find

$$k_J = \frac{\sqrt{4\pi G \rho_b}}{c_s} \quad (2.9)$$

called *Jeans wave number*, that is the Jeans scale in the Fourier space. We can also define the equivalent Jeans scale in the real space:

$$\lambda_J = c_s \sqrt{\frac{2\pi}{k_J}} = c_s \sqrt{\frac{\pi}{G \rho_B}} \quad (2.10)$$

that is equally to  $R_J$  previously defined in the Section 2.2.

We can now re-write the dispersion's equation, thanks to Eq.(2.10), as

$$\omega^2 = k^2 c_s^2 \left[ 1 - \left( \frac{\lambda}{\lambda_J} \right)^2 \right]. \quad (2.11)$$

We have two kinds of solution:

- If  $\lambda < \lambda_J$  and  $k > k_J$ , then  $\omega^2 > 0$ . This means that the pulsation is real. Replacing the two real values of  $\omega$  in Eq.(2.5) the solutions have an imaginary temporal part and a real phase part, thus two progressive plane waves with opposite propagation directions;
- If  $\lambda > \lambda_J$  and  $k < k_J$ , then  $\omega^2 < 0$ . This means that the pulsation is imaginary, but now the solutions are

$$\delta = \delta_k \exp\left(i\vec{k} \cdot \vec{r}\right) \exp(\mp|\omega|t) \quad (2.12)$$

that have a real temporal part, so the wave amplitude changes in time. In this case, we have stationary waves with amplitude either increasing or decreasing in time: a solution describes a perturbation with an exponential growth, the other one describes a perturbation with an exponential decrease in time. Because of the exponential growth, the perturbation is unstable. These solutions are valid for a linear regime. However, the perturbation grows exponentially in time, so it becomes quickly no linear.

## 2.3 The Jeans theory in expanding Universes

In an expanding Universe, as in  $\Lambda$ CDM model, we have to consider that the expansion contrasts the collapse of the matter. In this scenario, the velocity  $\vec{v}_B$  in Eq.(2.2) is not null and follows the Hubble-Lemaître law:

$$\vec{v}_B = H(t)\vec{x}.$$

We also assume that the background density changes over time

$$\rho_B = \rho_B(t).$$

To proceed with this study, it is convenient to define some fundamental scales of the problem.

### 2.3.1 Cosmological horizon

The cosmological horizon,  $R_H$ , is the radius defining the spherical region of the Universe in causal connection: it is the space travelled by a photon, defined as

$$R_H(t) = a(t) \int_0^t \frac{c dt'}{a(t')}. \quad (2.13)$$

The horizon is finite, due to the finite speed of light, and grows in time, also because of the expansion of the Universe. Indeed, the causally connected region grows faster than the speed of light, due to the Universe expansion.

To describe the structure formation of cosmic structures, at scale larger than  $R_H$ , the only important interaction is the gravity, described as in GR, while other interactions are important only for  $R < R_H$ .

## Hubble radius

The Hubble radius gives the distance from the observer at which the recession velocity of a galaxy would equal the speed of light.

$$R_{HS}(t) = \frac{c}{H(t)}. \quad (2.14)$$

Roughly speaking, the Hubble radius is the radius of the observable Universe because it is the distance travelled by a photon in the typical time of the universe expansion  $H^{-1}$ , as previously discuss in Section 1.3.2.

## Equivalence time and decoupling time

It is important also to define fundamental time scales. The *equivalence time*  $t_{eq}$  is defined as the moment in which the matter started to dominate in density on the radiative component, (as it is shown in Section 1.4.2, Fig.1.1). Therefore, from this moment, the radiation pressure was no longer able to contrast the gravitational collapse of matter. The *decoupling time* instead is the instant in which the baryons decouple from the radiation because the scattering rate between these two components become negligible and the free mean path of a photon becomes practically infinite.

### 2.3.2 Outside the Cosmological Horizon

For scales larger than  $R_H$  the gravity is the only important interaction so we describe the problem through GR, while the micro-physics in this discussion can be completely neglected. In this scenario, we can consider the perturbations like a closed Universe ( $\Omega > 1$ ,  $K = 1$ ), as we have previously presented in Section 1.4.4, described by Friedmann Equations because we are not interested on micro-physics. We assume these perturbations are immersed in an EdS Universe, described in Section 1.4.4. Considering these assumptions during the different Universe periods, in which we know we can consider only the dominant component coupled with the other through gravitation for  $R > R_H$ , we have:

- For  $t < t_{eq}$  the Universe is dominated by radiation, so  $w = 1/3$  and that means

$$\delta_{rad} \propto \delta_{mat} \propto a^2$$

- For  $t > t_{eq}$  the Universe is dominated by matter, so  $w = 0$  and that means

$$\delta_{mat} \propto \delta_{rad} \propto a$$

### 2.3.3 Inside the Cosmological Horizon

When we consider scales  $R < R_H$  we have to consider the micro-physics and so we have to come back to the hydrodynamics equations. In order to consider these perturbations we have to re-write hydrodynamics equations, Eq.(2.1), but in an expanding Universe. Once again we assume to know the solutions for the unperturbed case and then we are going to consider the perturbed fluid, that in the proper reference system (in physical coordinates) is:

$$\begin{cases} \frac{\partial \rho}{\partial t} \Big|_{\vec{r}} + \nabla_{\vec{r}}(\rho \vec{u}) = 0 \\ \frac{\partial \vec{u}}{\partial t} \Big|_{\vec{r}} + (\vec{u} \nabla_{\vec{r}}) \vec{u} = -\frac{1}{\rho} \nabla_{\vec{r}} p - \nabla_{\vec{r}} \phi \\ \Delta_{\vec{r}}^2 \phi = 4\pi G \rho, \end{cases} \quad (2.15)$$

where  $\vec{r} = a(t)\vec{x}$ . The velocity in physical coordinates is linked with the velocity in comoving coordinate through

$$\frac{d\vec{r}}{dt} = \dot{\vec{r}} = H\vec{r} + a\dot{\vec{x}} = H\vec{r} + \vec{v} = \vec{u},$$

where  $v = a\dot{x}$  is the peculiar velocity of perturbations compared to the Hubble flow.

To find the solution we perturb the background solution, defined as

$$\begin{cases} \rho = \rho_B + \delta\rho = \rho_B (1 + \delta) \\ \vec{u} = H\vec{r} + \vec{v} \\ \phi = \phi_b + \delta\phi \\ p = p_b + \delta p \end{cases} \quad (2.16)$$

We can write the perturbed hydrodynamics equations in the proper coordinate system

$$\begin{cases} \frac{\partial \delta\rho}{\partial t} + \rho_b \nabla \delta\vec{v} + 3H\delta\rho = 0 \\ \frac{\partial \delta\vec{v}}{\partial t} + H\vec{v} + H\vec{r} \cdot \nabla \vec{v} = -\frac{1}{\rho_b} \nabla \delta\rho - \nabla \delta\phi \\ \Delta \delta\phi = 4\pi G \delta\rho \end{cases} \quad (2.17)$$

We can also re-write these equations in co-moving coordinates in which the terms related to the Universe expansion disappear

$$\begin{cases} \left( \frac{\partial \delta\rho}{\partial t} \right)_{\vec{x}} + \frac{\rho_b}{a} \nabla_{\vec{x}} \vec{v} + 3H\delta\rho = 0 \\ \left( \frac{\partial \delta\vec{v}}{\partial t} \right)_{\vec{x}} + H\vec{v} = -\frac{c_s^2}{a} \nabla \delta\rho - \frac{1}{a} \nabla_{\vec{x}} \delta\phi \\ \frac{1}{a^2} \Delta_{\vec{x}} \delta\phi = 4\pi G \delta\rho \end{cases} \quad (2.18)$$

Thanks to these equations we can now develop the Jeans theory for an expanding Universe. Once again we are going to search for solutions as plane waves but in this case the amplitude is not longer constant over time

$$f(x, t) = f_k(t) \exp(ikx).$$

Using this equation as a solution to Eq.(2.18), we have

$$\begin{cases} \dot{\delta}_k + ik \frac{v_k}{a} = 0 \\ \dot{v}_k + \frac{\dot{a}}{a} v_k = \frac{ik}{a} (c_s^2 \delta_k + \delta\phi_k) \\ \delta\phi_k = -\frac{4\pi G \delta_k \rho_b a^2}{k^2} \end{cases} \quad (2.19)$$

in the Fourier space.

## Perturbations during the Radiation Era

As we discussed in Section 1.4.4, every Universe approaching the BB behaves as flat. Therefore, to discuss the evolution of the primordial density fluctuations, we have to solve the dispersion's relation, Eq.(2.8), for EdS Universe at  $t < t_{eq}$ . Solving the dispersion's equation to study the the temporal evolution of the density perturbation  $\delta$ , leads to two different scenarios:

1. For  $\lambda < \lambda_J$ , the perturbation propagates as a sound wave;
2. For  $\lambda > \lambda_J$ , the wave has an amplitude changing over time:

$$\delta_-(\vec{x}, t) \propto a^{-3/2} \quad (2.20)$$

$$\delta_+(\vec{x}, t) \propto a \quad (2.21)$$

The first solution, Eq.(2.20), decays and cannot lead to formation of structures. On the other hand, the second solution, Eq.(4.12) describes a density perturbation growing in time. Therefore, this solution is cosmologically relevant, because, increasing in time, it can lead to gravitational instability.

As a first approximation, Eq.(4.12) describes how a density perturbation, with  $\lambda_J < \lambda < \lambda_H$ , grows inside the horizon for every type of matter during the Radiation Era. However,

during the Radiation Era, far from  $t_{eq}$ , the Universe was completely dominated in density by a fluid of relativistic particles. Therefore, the huge radiation pressure humped the evolution of perturbations. During the Radiation Era, baryonic matter was coupled to radiative fluid via frequent scattering. For this fluid, it is the radiation pressure that prevents the perturbations from collapsing. On the other hand, DM forms a collisionless fluid (see Section 1.5). The problem of the evolution of DM before  $t_{eq}$  was for the first time investigated by Meszaros, who found out that, inside the horizon, a DM perturbation over  $\lambda_J$ , grows at most by a factor of 5/2, instead of growing proportionally to  $a$  (Meszaros, 1974). This phenomenon is called *stagnation effect* or *Meszaros effect*.

## Perturbations during the Matter Era

Considering  $t > t_{eq}$  the Universe is dominated by the matter and the radiation pressure is neglected. In hydrodynamics equation (Eq.2.17) we can see the velocity  $\vec{v}$  in its parallel and perpendicular components with respect to  $\vec{k}$ :

$$\vec{v} = \vec{v}_{k,\perp} + v_{k,\parallel}$$

Therefore Eq.(2.17) becomes

$$\begin{cases} \dot{\delta}_k + \frac{ikv_{k,\parallel}}{a} = 0 \\ \dot{v}_{k,\parallel} + \frac{\dot{a}}{a}v_{k,\parallel} = -\frac{ik}{a}(c_s^2\delta_k + \delta\phi_k) \\ k^2\delta\phi_k = -4\pi a^2\rho_B\delta_k \end{cases} \quad (2.22)$$

so, the only not neglected term is  $v_{\parallel}$  because  $v_{\perp} \propto a^{-1}$  that means this component decays rapidly during the Universe evolution.

From Eq.(2.19) we can obtain a second order differential equation that describes the temporal evolution of the density field within an expanding Universe. The dispersion relation in physical coordinates is

$$\ddot{\delta}_k + 2\frac{\dot{a}}{a}\dot{\delta}_k + (k^2c_s^2 - 4\pi G\rho_b)\delta_k = 0, \quad (2.23)$$

where

$$2\frac{\dot{a}}{a}\dot{\delta}_k = 2H(t)\dot{\delta}_k. \quad (2.24)$$

This last term contains the Universe expansion and depends on the assumed cosmological model through the Hubble parameter, while  $k^2c_s^2\delta_k$  includes the fluid velocity field.

Thanks to this equation, it is possible to investigate the evolution of perturbation for  $t > t_{eq}$  for different Universes.

If we consider a mono-component and flat Universe  $\Omega_w = 1$  with  $w = 0$ , solving the dispersion's equation, Eq.(2.23), searching for solutions having power law form, we obtain the following scenarios:

- For  $\lambda < \lambda_J$ , the dependence in time is imaginary and that means the wave propagates without changing its amplitude;
- $\lambda > \lambda_J$ , we have a wave changing its amplitude over time

$$\delta_-(t) \propto a^{-3/2}$$

$$\delta_+(t) \propto a$$

where the Jeans scales are

$$\begin{cases} k_J = \frac{5}{c_s} \sqrt{\frac{\pi G\rho_b}{6}} \\ \lambda_J = \frac{c_s}{5} \sqrt{\frac{24\pi}{G\rho_b}}. \end{cases} \quad (2.25)$$

We are interested in the Eq.(2.25) to describe structure formation in cosmology. This solution would be valid for every type of matter, however dark and baryonic matter interact through gravity but dark matter decouples from the radiation much before baryons. Therefore, dark matter, from the decoupling moment, grows proportional to the expansion factor  $a$ , while baryonic

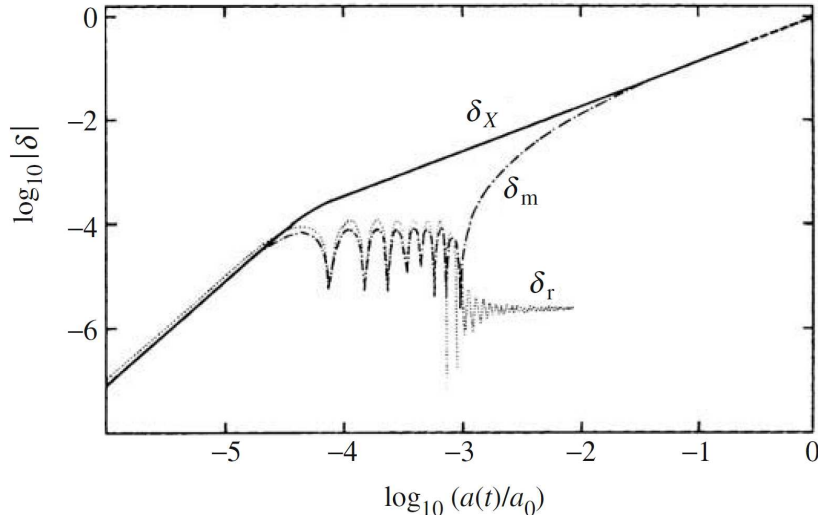


**Figure 2.1:** Evolution of density perturbations in cold dark matter  $\delta_X$ , baryonic matter  $\delta_m$  and radiation  $\delta_r$  components, at mass scale  $M \sim 10^{15} M_\odot$  in a Universe with  $\Omega = 1$ . Credits to: P. Coles (2008)

matter is still coupled with the radiation. When the baryons also decoupled from the radiation, the dark matter perturbations have already grown. For that reason, the baryonic matter immediately follows the gravitational potential of the already grown dark matter haloes. Hence, the baryonic perturbations do not have an increasing proportional to  $a$  but its growing following

$$\delta_b \propto \delta_{DM} \left(1 - \frac{a_{dec}}{a}\right).$$

This phenomenon is called *baryon catch-up* (see Fig.2.1). It is necessary to take it into account to explain the values of  $\delta_b$  we observe today. Indeed, without this phenomenon we expect  $\delta_b \sim 10^{-2}$  today, while, inside galaxy clusters we observe  $\delta_b \sim 10^3$ .

In the case of a Universe with multiple components and with flat geometry or curved one, an analytical expression which define  $\delta_+(z)$  does not exist but approximate formula are used. Moreover, it is also defined the *growth factor*  $f$ , as a function of the density parameter evaluated at  $z = 0$ :

$$f(\Omega_0) \equiv \frac{d \log \delta_+}{d \log a} \approx \Omega_{m,0}^{0.55} + \frac{\Omega_\Lambda}{70} \left(1 + \frac{1}{2} \Omega_{m,0}\right). \quad (2.26)$$

## 2.4 Perturbation theory

In Section 2.1 we have pointed out that the seeds of density perturbations  $\delta$  are produced at the end of the Inflationary Era thanks to the decay of the *inflaton field* in particles. The perturbations growth depends on Universe type, time and matter, as we have studied in the previous sections of this Chapter. Thus, at the end of Inflationary Epoch we have metric fluctuations, that we can see as  $\delta\phi_k$  in the Newtonian approach, linked to  $\delta_k$  through the Poisson's Equation. The fluctuations  $\delta\phi_k$  have a random distribution so  $\delta_k$  follow a random distribution too. Therefore, we can consider the density contrast as a homogeneous and isotropic stochastic field: the value of the field at each point is randomly extracted from a probability distribution. To extend the CP to a perturbed Universe, we have to assume that the probability distribution has to be invariant for translations and rotations. To have a good statistic, we would need a sufficiently large sample but it is not the case of our Universe, because the sample consists of the Universe itself. To solve the problem and to apply statistical methods, we can use the ergodic hypothesis. Thanks to this hypothesis we can see the Universe as a set of many independent sub-Universes because sufficiently large regions of the Universe, sufficiently separated, are statistically independent from each other.

A generic perturbation of the density field  $\delta(\vec{x}, t)$  is represented in Fourier space as a superposition of plane waves that are independent during the evolution, so we have

$$\delta(\vec{x}) = \frac{1}{(2\pi)^3} \int \delta(\vec{k}) e^{i\vec{k}\vec{x}} d^3\vec{k}$$

$$\delta(\vec{k}) = \int \delta(\vec{x}) e^{-i\vec{k}\vec{x}} d^3\vec{x}$$

where

$$\delta(\vec{x}) \equiv \frac{\delta(\vec{x}) - \delta_b}{\delta_b}.$$

As we said, the seed formation is described by a random process so the fluctuations  $\delta_k$  are generated with a stochastic and Gaussian distribution. Therefore, we expect that if we measure the  $\delta(\vec{x})$  value in different positions of the Universe, we will obtain a Gaussian distribution  $P(\delta)$ . Thus, to describe their distribution we have to know only the average  $\langle \delta(\vec{x}) \rangle$  and the variance  $\langle \delta^2(\vec{x}) \rangle$ . The average of a stochastic fluctuation is null, hence, by definition, the only value that defines this field is the variance:

$$\sigma^2 \equiv \frac{1}{V_\infty} \int d^3x \langle \delta^2(x) \rangle, \quad (2.27)$$

where  $V_{\text{inf}} = \int d^3x$  is called *Universe volume*.

In Fourier space, Eq.(2.27) is defined as

$$\sigma^2 \equiv \frac{1}{(2\pi)^3 V_\infty} \int d^3k \langle \delta^2(k) \rangle, \quad (2.28)$$

where  $\langle \delta^2(k) \rangle$  is called *power spectrum*  $P(k)$ . The power spectrum measures the contribution of the scale  $k$  to a generic fluctuation in  $\delta(x)$  indeed it is represented in Fourier space as a superposition of such plane waves, that have the advantage to be independent during their linear evolution.

The power spectrum is related via a Fourier transform to its analogous quantity in the real space, the *correlation function*, defined as:

$$\xi(\vec{r}) = \langle \delta(\vec{x}) \delta(\vec{x} - \vec{r}) \rangle \quad (2.29)$$

and that we can also defined through Fourier transform, as:

$$\xi(r) = \frac{1}{(2\pi)^3} \int d^3k P(k) e^{ikr} \quad (2.30)$$

### 2.4.1 Punctual variance of the field and mass variance

Measuring the density field of the Universe is difficult because, from an observative point of view, we can only get information on over-dense regions that emit radiation, instead we have no information about regions that are not emitting, as *voids* and regions filled by dark matter. In order to study density field, one can simply count the structures filling a given volume of the Universe. Unfortunately, the density field is a continuous function while the distribution of observable objects (galaxies, galaxy clusters) obtained by counting the emitting regions, is discrete.

If we count galaxies within a given volume  $V$ , for different volumes  $V$ , we can define:

$$\delta_g = \frac{N_g(V) - \langle N_g(V) \rangle}{\langle N_g(V) \rangle}.$$

Since we want information about the mass distribution, we can write  $\delta_g$  as:

$$\delta_g = b \left( \frac{M_g(V) - \langle M_g(V) \rangle}{\langle M_g(V) \rangle} \right) \equiv b \delta_M, \quad (2.31)$$

where we have corrected  $\delta_g$  for a *bias*  $b$ , a factor that contains all our ignorance about the formation and evolution of the galaxies when used as mass tracers. Assuming  $b = \text{const}$ , we can define the usual  $\delta$  from  $\delta_M$ , through a convolution that filters the continuous density field using a suitable window function in order to transform the discrete distribution in a continuous one. Usually, a top-hat filter is preferred, defined as a function constant inside a sphere with radius  $R_{TH}$  and null out of this radius. It is defined as:

$$W(\vec{x}, R_{TH}) = \frac{3}{4\pi R_{TH}^3} \Theta\left(1 - \frac{|x - x'|}{R_{TH}}\right), \quad (2.32)$$

using the Heavyside function. So, we can define the convolution as:

$$\delta_M(\vec{x}) = \delta(\vec{x}) \otimes W(\vec{x}, R_{TH}). \quad (2.33)$$

We can note that the top-hat filter is a low-pass filter hence, with this approach, we lose every information on scales below  $R_{TH}$ . Also,  $\delta_M$  will have a Gaussian distribution described only by variance. To determine the Gaussian form of  $\delta_M$  we define the mass variance:

$$\sigma_M^2 = \frac{1}{(2\pi)^3} \int_0^\infty \langle P(k) \rangle \hat{W}^2(\vec{k}, R) d^3\vec{k},$$

that, in spherical coordinates, is:

$$\sigma_M^2 = \frac{1}{(2\pi)^2} \int_0^\infty k^2 \langle P(k) \rangle \hat{W}^2(\vec{k}, R) d\vec{k},$$

where  $\hat{W}$  is the Fourier transform of the window function, which is a function of  $R$ , and therefore of  $M$ . Note that  $\sigma_M^2 \leq \sigma^2$ . The main contribution to  $\sigma_M^2$  is given by perturbations with  $\lambda \approx k^{-1} > R$ , because those with higher frequencies tend to be averaged out within the window volume. The mass variance is the typical size of a density fluctuation on a scale  $R$ . The value of this quantity at  $z = 0$  and  $r = 8 \text{ Mpc h}^{-1}$ , indicates as  $\sigma_8$ , is commonly used to parametrise the power spectrum normalisation.

## 2.4.2 The primordial Zel'dovich spectrum

The shape of the initial spectrum is assumed to be imprinted by inflation (as we said in Section 2.4). In this scenario the structures seeds are generated by stochastic quantum fluctuations in a scalar field (the *inflaton*) which lead to the perturbations of the density field (for a complete explanation, see Zeldovich, 1972) with random distribution. We can describe the power spectrum as a power-law form

$$P(k) = Ak^n$$

where  $A$  is the amplitude. There are not theoretical prediction for its value, while the theoretical prediction for the spectral index is  $n \approx 1$ , indeed the inflation theory does not predict a privileged scale for the fluctuations of the gravitational potential.

Therefore, while the shape of the power spectrum, given by  $n$ , may be fixed by these considerations and then compared with observative results, the amplitude value is defined by observations. Nowadays the most reliable measure of  $A$  is derived from the temperature fluctuations in the CMB.

Considering a perturbation formed at time  $t_i$ , with an amplitude  $\delta_i = \delta(\vec{x}, t_i)$  characterised by a scale  $\lambda \gg \lambda_J$ , at  $t > t_i$  its amplitude will be

$$\delta(t) = \delta_i \delta_+,$$

where the growth, described by  $\delta_+$ , is completely independent on the scale. So, for  $\lambda \gg \lambda_J$  every scale grows with the same rate, that means if we consider the primordial power spectrum as

$$P(k, t_i) = P_i = \delta_i^2,$$

at  $t > t_i$ ,

$$P(k, t) = \delta_i^2 \delta_+^2(t) = P_i \delta_+^2(t)$$

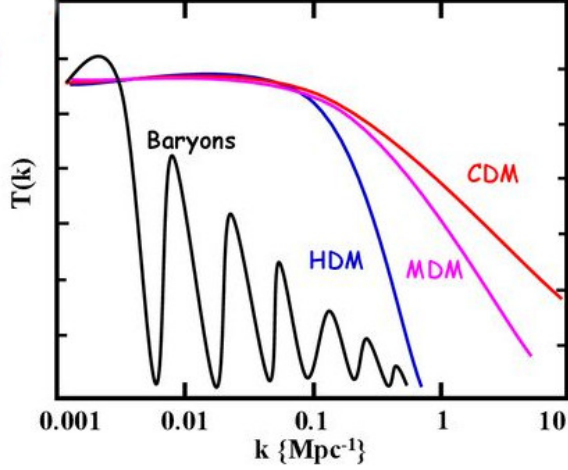


**Figure 2.2:** Transfer function for Hot Dark Matter (HDM) (red line), and Cold Dark Matter (CDM) (blue line). The HDM transfer function shows a rapid cut-off at high  $k$  caused by free-streaming, while CDM has a decrease at higher  $k$ , produced by the Meszaros suppression of fluctuations. It is also shown the transfer function for Mixed Dark Matter (30% relativistic neutrinos, 70% non-relativistic particles) and Baryons, taking into account BAO. Credits to: T. Duncan (2008)

that means the spectrum is parallelly elevated over time.

Coming back to the mass variance, we have

$$\sigma_M^2 \propto \delta_+^2 \int k^n d^3k \propto \delta_+ k^{n+3}, \quad (2.34)$$

where

$$\begin{cases} \delta_+ \propto a^2, & \text{for } a < a_{eq} \\ \delta_+ \propto a, & \text{for } a > a_{eq} \end{cases} \quad (2.35)$$

as we previously said in this Chapter.

We assume the structure collapse happens when  $\sigma_M \rightarrow 1$ :

$$1 \equiv \sigma_M \propto \delta_+^2(t) k^{n+3} \propto \delta_+^2 M^{-(n+3)/3},$$

so a structure with  $M_*$  at time  $t$ , defined as

$$M_*(t) \propto \delta_+(t)^{6/(n+3)} \quad (2.36)$$

collapses. That also means the time when the structures are formed during the Universe evolution is related to the index  $n$ . Moreover, the Eq.2.36 shows that, given an index  $n$ , the mass of the structure encountering gravitational instability grows over time.

If we consider Zel'dovich spectrum, so  $n \approx 1$ , we have, from Eq.(2.34):

$$\sigma_M(a_H) \propto M_H^{(1-n)/6} \longrightarrow \sigma_M = const,$$

when the perturbations enter in the horizon. That means the density perturbations enter the event horizon at different times but all with the same amplitude.

### 2.4.3 The Transfer Function

Depending on the assumed type of dark matter, and the parameters of the background cosmology, the growth of perturbations on particular length scales can be suppressed. In the cosmological Jeans Theory, dissipation phenomena, caused by radiation pressure and relativistic particles, occur inside  $R < R_H$  at  $t < t_{eq}$ . Moreover, considering HDM, characterised by collisionless relativistic particles, its particles can travel rapidly, within a *free streaming* radius, damping away perturbations characterised by  $M_{eq} < 10^{15} M_\odot$ . Instead, assuming CDM, characterised by collisionless non-relativistic particles, the *free streaming radius* is shorter than in HDM models.

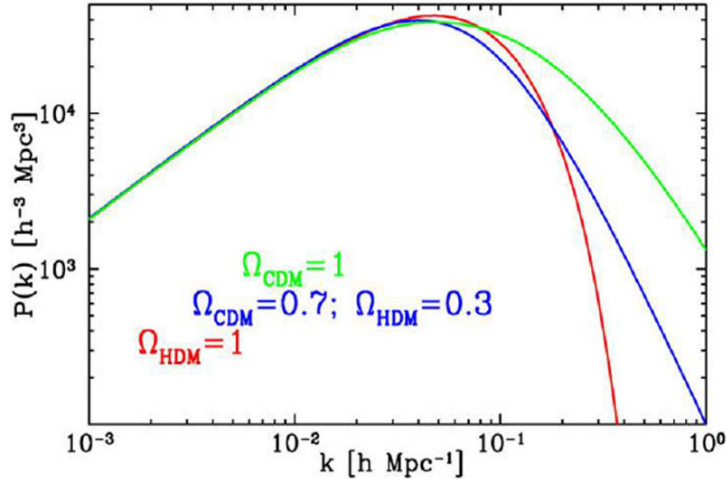


**Figure 2.3:** Resulting power spectrum for HDM (red line), CDM (green line) and Mixed DM, MDM, (blue line) in which Dark Matter is considered being formed by both relativistic and non-relativistic particles. Credits to: Norman (2010)

Thus, only perturbations with  $M_{eq} < 10^6 M_\odot$  are damped away. Because of the dimensions of the primordial structures, progenitors of the current ones, depend on the type of dark matter assumed, the CDM scenario is assumed in  $\Lambda$ CDM model, because it provides a hierarchical assembly of the matter where the first structures to virialise are the smaller ones (*Bottom-Up scenario*). Considering the HDM we have the opposite case (*Top-Down scenario*), incapable to justify our observational knowledge about structure evolution, perfectly explained by the Bottom-Up scenario.

Furthermore, prior to the decoupling, when photons were scattered by electrons through Thomson scattering, radiation pressure opposed the gravitational collapse of matter: the baryon-photon fluid perturbations oscillate in the already formed DM haloes, instead of directly collapse in them, due to the equilibrium between gravitational attraction and radiation pressure. This phenomenon generates pressure waves, known as Baryonic Acoustic Oscillation (BAO), leaving a signature in the distribution of matter on very large scales and in the features of CMB anisotropies.

The net effect of all these processes is to change the shape of the original power spectrum. It is possible to describe this change by the *transfer function*. To examine the evolution of the power spectrum, considering these phenomena, it is used the *transfer function* (see Fig.2.2).

At  $t_{eq}$ , we can describe the power spectrum as:

$$P(k, a_{eq}) = P_{in}(k)T^2(k) = Ak^n T^2(k) \quad (2.37)$$

where, in  $\Lambda$ CDM scenario:

$$\begin{cases} T(k) \propto k^{-2} & \text{for } a_H < a_{eq}, \quad k \gg k_{eq} \\ T(k) \propto k^0 & \text{for } a_H > a_{eq}, \quad k \ll k_{eq} \end{cases} \quad (2.38)$$

Finally, we can obtain an accurate theoretical prediction for the power spectrum (see Fig.2.3) at  $z_{eq}$ , characterised by a turn over at  $R_H \approx 16 (\Omega_{0,M} h)^{-1} \text{Mpc}$ .

## 2.5 The evolution theory in the non-linear regime

In the previous sections, we have discussed the evolution of primordial density perturbations within the Jeans Theory, which is based on the assumption of linearity,  $\delta(\vec{x}, t) \ll 1$ , and thus cannot describe the non-linear evolution of cosmic structures.

Indeed, after the equivalence, the density fluctuations of dark matter with mass bigger than the free streaming mass at  $t_{eq}$  can grow, and nowadays we observe structures like galaxy clusters characterised by  $\delta \approx 10^2$  or  $10^3$ . To study the non-linear evolution we have to elaborate a

non-linear theory, as we have done before for the linear one. However, in a non-linear approach, an analytic description cannot be obtained without any symmetric assumptions. Therefore, to investigate the non-linear evolution, numerical simulations are generally requested (see Section 2.5.2).

### 2.5.1 Spherical collapse

It is possible to obtain an analytical solution in the non-linear regime only for *an isolated spherically symmetric perturbation*, initially at rest. This model describes the evolution of a spherical overdensity, that detaches from the background density field and possibly collapses in a finite timescale. Assuming a background Universe in which this spherical perturbation is immersed, we can obtain the following relations:

$$\begin{cases} \delta(t) = \frac{3}{5} \delta_+(t_i) \left(\frac{t}{t_i}\right)^{2/3} \\ \delta_+ > \frac{3}{5} \frac{1 - \Omega_{bkg}(t_i)}{\Omega(t_i)(1+z_i)} \end{cases} \quad (2.39)$$

Therefore, in a closed and flat background Universe any overdensity can collapse while in an open one, the collapse is only possible when the overdensity exceeds a certain value. At first, the overdensity still follows the background dynamics, namely it follows the Hubble flow. However, the overdensity has a deceleration caused by gravitational interactions and finally stops at the *turn-around epoch*. At this point, the overdensity evolves independently of the background and it might collapse. The collapse of the perturbation, with density  $\rho_P$ , happens at the turn-around time

$$t^* \propto \sqrt{\rho_P(t^*)^{-1}} \quad .$$

At this time the perturbation is already non-linear. Then, if the structure collapsed, it is possible to reach the *virialisation* at  $t_{vir} \approx 3t^*$ , obtaining a bound object that we call halo.

### 2.5.2 N-body simulations

As we mentioned, to study the non-linear evolution numerical simulation can be exploited. The formation of cosmic structures can be approximated as the dynamical evolution of a system of particles, describing the underlying mass distribution. To study this system it is impossible to employ an analytic approach, therefore N-body simulations are exploited by cosmology to analyse the Large Scale Structure (LSS) of the Universe with numerical method. With the N-body simulations the fundamental advantage is that the growth in non-linear regime of structure can be investigated without the necessary assumptions adopted for obtaining analytical solutions.

One of the main advantages of working with the numerical simulations is that the cosmological parameters can be assumed as the users want and then the results can be compared to our observations, and, therefore, it is possible to infer which cosmological model predicts the observed LSS.

Moreover, because we are interested in the LSS of the Universe, the evolution is dominated by the gravitation so, at the first order, it will be sufficient to study the behaviour of the DM component. However, to obtain a more realistic description of the evolution of the LSS, for the purpose of comparing the results with the observation, also the baryonic component has to be considered. Considering the baryonic component means taking into account also the hydrodynamic interaction.

If only the DM component is studied, the N-body simulations solves the following dynamical equation system:

$$\begin{cases} \vec{F}_i = GM_i \sum_{i \neq j} \frac{M_j}{r_{ij}^2} \hat{r}_{ij}^2 \\ \ddot{\vec{x}} = \frac{d\vec{v}_i}{dt} = \frac{\vec{F}_i}{M_i} \\ \dot{\vec{x}}_i = \frac{d\vec{x}_i}{dt} = \vec{v}_i \end{cases} \quad , \quad (2.40)$$

where  $\vec{F}_i$  is the gravitational force of the  $i$ -th particle,  $G$  is the gravitational constant,  $M_i$  is the  $i$ -th particle mass,  $\vec{x}_i$  are the comoving coordinates of the  $i$ -th particle,  $\vec{v}_i$  are the velocity components of the  $i$ -th particle,  $r_{ij}$  is the comoving distance between the  $i$ -th and  $j$ -th particles,

and  $\hat{r}_{ij}$  is the related versor. Given the system Eq.2.40, the Euler equation in the system (2.1) can be express as:

$$\frac{d\vec{x}_i}{dt} + 2\frac{\dot{a}}{a}\vec{v}_i = -\frac{1}{a^2}\nabla\Phi = \frac{\vec{F}_i}{a^3}, \quad (2.41)$$

where  $a$  is the scale factor. The Poisson Equation defined in the system Eq.2.40 can be re-written considering the Second Friedmann Equation (1.17), as follows:

$$\Delta\Phi = 4\pi G\bar{\rho}(t)a^2\delta = \frac{3}{2}H_0^2\Omega_0\frac{\delta}{a}, \quad (2.42)$$

where  $\bar{\rho}$  is the mean density of the non-relativistic component of the Universe,  $\delta$  is the local density contrast,  $H_0$  is the Hubble parameter and  $\Omega_0$  is the density parameter dor the non-relativistic matter.

A N-body simulation consists in the integration of the dynamical equations over time steps  $\delta t$ . The final output of a N-body simulation is a set of snapshots, that illustrated at each instant the evolution of the system of particles, as a result of the action of the gravitational force.

Different computational methods are use to develop the N-body simulations, the most used techniques are:

- Particle-Particle (PP): with this computational method, the force acting on the  $i$ -th particle is computed as the sum of all the forces generated by all the other particles in the system. This method is the most accurate because the force is directly computed for each particle but it is also the most time consuming;
- Particle Mesh (PM): this method exploits a grid for determining the total gravitational force. The relevant quantities are computed in each cell. In this approach, the Poisson Equation (2.42) is solved in the Fourier domain on the grid, then it is Fourier transform for applying the force in the real space. This method is faster because grid is used instead of computing the force for each particle but in less accurate, due to the limited resolution of the grid;
- Particle-Particle Particle Mesh (P<sup>3</sup>M): in this approach is exploited a grid as in the PM techniques, but is also define a radius  $R$  and spheres with this radius are define around each particle. Inside these spheres, the PP method is used. Therefore, this method is more accurate than the PM one and it is also less time consuming than the PP method.
- Tree code: this method represents the favourite method for cosmological N-body simulations. The general idea is to solve the N-body problem in a hierarchical tree of sub-regions. Each sub-region is characterised by a proper mass centre. For the particle in the same region is used the PP method while, the gravitational interaction with the other sub-region is considered as caused by the entire mass in the region as centred in the proper centre of mass of those regions (that is assumed the single multipole force).

As we mentioned, the formation and evolution of cosmic structures is not determined only by the gravity due to the total matter distribution but also the behaviour of the gas is involved. The processes in action on the baryonic component influence the final proprieties of the structures that we observe. In particular, the processes that are taking into account in the hydrodynamic simulations are: the cooling processes, the star formation, the supernova feedback and the chemical enrichment.

An overview over the N-body simulation in cosmology, both for the gravitational force only and considering also the hydrodynamic interactions are reported in Moscardini et al. (2011).

### 2.5.3 The Mass and Luminosity functions

In order to test our cosmological models, we have to link our theoretical predictions to observables. One of these observables is the *mass function*, which is linked to the haloe formation and evolution, that describes the number of objects with a mass between  $M$  and  $M + dM$ , at a given time per unit of comoving volume. Specifically, the mass function of cosmic structure is defined as:

$$\frac{dn(M, z)}{dM} = f(\sigma(M, z)) \frac{\bar{\rho}}{M} \frac{d \ln \sigma(M, z)^{-1}}{dM}, \quad (2.43)$$

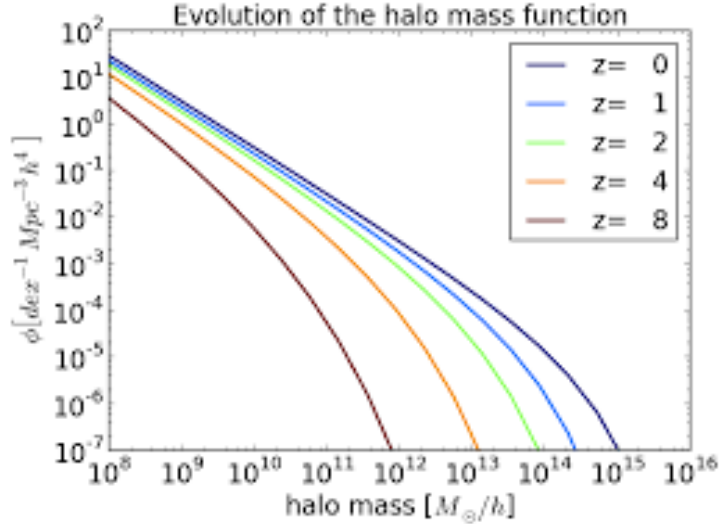


**Figure 2.4:** The dark matter halo mass function at different redshift, showing how the *knee* position, at  $M_*$ , changes over time. Credits to: Lilly (2014)

where  $\bar{\rho}$  is the mean matter density of a fluctuation with mass  $M = \frac{4}{3}\pi R^3 \bar{\rho}$ ;  $f(\sigma(M, z))\bar{\rho}$  defines the amount of mass contained in fluctuations with mass  $M$  at redshift  $z$ , and  $\sigma(M)$  represents the mass variance. In particular

$$f(\sigma(M)) = \frac{2}{\pi} \frac{\delta_c}{\sigma(M)} \exp\left(-\frac{\delta_c}{2\sigma^2(M)}\right),$$

with  $\rho_c \simeq 1.68$ , that is the threshold value for having a collapse on which the Press-Schechter model is based (Press et al. (1974)). The Press-Schechter mass function is:

$$n(M, z) dM = \sqrt{\frac{2}{\pi}} \frac{\delta_c \bar{\rho}_M(z)}{\sigma_M(z) M^2} \left| \frac{d \ln \sigma_M}{d \ln M} \right| \exp\left(-\frac{\delta_c}{2\sigma_M^2(z)}\right)$$

The form of this distribution function is that of a power-law, with an exponential cut from a certain value of the mass, called the *characteristic mass*  $M_*$ , (see. Fig.2.4):

$$M_* = M_0 \left(\frac{2}{\delta_c}\right)^{1/2\alpha},$$

where  $M_0$  is the normalisation mass value and  $\alpha = (n+3)/6$ . Therefore,  $M_*$  increases in time, together with  $\Omega_M$ , because it is dependent on  $n$ , through  $\alpha$ . At the present time,  $M_* \approx 10^{15} M_\odot/h$ , which is the typical mass for a cluster of galaxies. Hence, counting the number of clusters in the local Universe is equivalent to counting how much mass is contained in the exponential tail of the mass function. This can be exploited to constrain two degenerate cosmological parameters:  $\sigma_8$  and  $\Omega_M$ , respectively through  $\rho_M$  and the amplitude of perturbations  $A$  of the power spectrum. For local clusters

$$\sigma_8 \approx A \Omega_{0,M}^{-0.5, -0.8}, \quad (2.44)$$

with  $A \approx -0.5, -0.8$ .

From Eq.(2.43) it is possible to define the total number of haloes,  $N_h$ , above a certain mass threshold,  $M_{min}$ , in a comoving volume,  $V$ , as follows:

$$N_h \propto \int_{z_{min}}^{z_{max}} \int_{M_{min}}^{\infty} \frac{dV}{dz} n(M, z) dM dz, \quad (2.45)$$

where  $z_{min}$  and  $z_{max}$  are the redshift boundaries, and  $\frac{dV}{dz}$  is the comoving volume element.

The halo mass function is analogous to the Schechter luminosity function:

$$\Phi(L) = AL^\beta \exp\left(-\frac{L}{L_*}\right), \quad (2.46)$$

where  $A$  is the normalisation,  $\beta = \alpha - 2$  is the slope and  $L_*$  the *knee* luminosity, which marks the transition from the power-law to the exponential form, as  $M_*$  in the Press-Schechter model. If a constant mass-luminosity ratio,  $M/L$ , is assumed, it is possible to link the mass function,  $n(M)$ , to the luminosity one,  $\Phi(L)$ , with the following relation:

$$\Phi(L) = n(M) \frac{dM}{dL}. \quad (2.47)$$

# Chapter 3

## Clusters of galaxies

This Chapter starts with a brief introduction on the main cluster of galaxies properties (in Section 3.1; see Lima Neto et al. (2014) for a more detailed overview). Then, we will focus in particular on methods for estimating cluster masses, giving a description of the main *scaling relations* exploited to study these objects (Section 3.2). Moreover, we will discuss the main techniques to identify galaxy clusters. At the end of the Chapter, the role of clusters in cosmology is briefly described.

### 3.1 Galaxy Clusters Observations

Galaxy clusters have been observed for the first time quite early in the history of modern astrophysics by Messier (Messier, 1784) and Herschel (Herschel, 1785). However, their extragalactic nature was understood only through the dynamical analysis carried out by Zwicky (1937) and Smith (1936). Moreover, as we mentioned in Section 1.5, those dynamical studies led to the first hint of the existence of DM.

First catalogues of clusters were created simply by estimating the number of galaxies per unit solid angle in visible wavelengths by Abell (1958) and Zwicky et al. (1961). Then, thanks to the Uhuru satellite (Giacconi et al., 1972), the first all-sky X-ray survey was obtained, showing that clusters are spatially extended X-ray sources.

Clusters typically have masses of  $10^{13} - 10^{15} M_{\odot}$ , size extension within few Mpc, velocity dispersion of  $10^2 - 10^3$  km/s and the member galaxies contained are about  $\sim 5 \cdot 10^2$ , for a *poor cluster*, and  $\sim 10^3$ , for a *rich cluster*.

Clusters are multi-component structures composed of galaxies (2% – 5%), Intra-Cluster Medium (ICM, 11% – 15%) and DM (80% – 88%).

The typical galaxy population is composed of early-type galaxies that had ended up their star formation phase at  $z \geq 2$ . The ICM represents most of the baryonic matter contained in a cluster and it is responsible for the X-ray emission, because this gas reaches  $10^8$  K, so it is characterised by bremsstrahlung emission, with a characteristic luminosity in X-ray wavelengths of  $L_X \sim 10^{43} - 10^{45}$  erg/s.

The DM Halo, in which the baryonic matter of the cluster is situated, is generally represented by the Navarro-Frenk-White (NFW) radial profile (Navarro et al., 1997).

Therefore, since a cluster is a complex and multi-component system, it is observable across the whole electromagnetic spectrum: the galaxy population and the intra-cluster light (given by a stellar component situated outside the member galaxies) are visible in optical and near-infrared bands; the hot ICM is instead detected thanks to the strong X-ray emission; at radio frequencies, synchrotron emission from relativistic electrons located within the ICM, caused by shock processes, can be detected; at millimetre wavelengths, the thermal Sunyaev-Zel'dovich (tSZ) effect (Sunyaev et al., 1972) is observed, a phenomenon that involves CMB photons moving through the ICM. This effect leads to the distortion of the CMB black-body spectrum. Indeed, photons from the CMB passing through the ICM can be inverse-Compton scattered by the ionised plasma. On average, the energy of the scattered photons is increased. This produces a slight intensity/temperature decrease at radio wavelengths and a slight increment at mm wavelengths.

Finally, strong features are also detected thanks to the gravitational lensing effect, which gives information about the mass of the DM halo.

## 3.2 Estimation of the mass

In the study of galaxy clusters one of the main issue is to estimate their mass. Indeed, their total mass cannot be directly observed but it is necessary to use a *deducted mass* from other observable properties, called, in this context, *mass proxies*, which correlate with the true mass via the so-called *scaling relations*. Different proxies, which can be applied in different wavelengths, have been used so far to estimate the mass of clusters from observations, through the definition of different scaling relations based on the assumption of fundamental physical processes or empirically calibrated on observations (for a detailed overview on this topic see Giodini et al., 2013).

### 3.2.1 X-ray emission

As we previously mentioned, clusters are extended X-ray sources emitting thermal bremsstrahlung radiation from the ICM, which comes to a temperature of several keV. Studying this thermal emission is one of the main methods to determine the mass of a cluster, by assuming the hydrostatic equilibrium and spherical symmetry to analyse the ICM.

The condition of hydrostatic equilibrium, that is the balance between the pressure force and the gravitational one, is reached when:

$$\nabla P_{gas} = -\rho_{gas} \nabla \phi, \quad (3.1)$$

where  $P_{gas}$  and  $\rho_{gas}$  are, respectively, the gas pressure and density, while  $\phi$  is the gravitational potential. Assuming for the ICM a distribution with spherical symmetry, the hydrostatic equilibrium condition, Eq.(3.1), is expressed as follows:

$$\frac{dP_{gas}}{dr} = -\rho_{gas} \frac{GM(<r)}{r^2},$$

where  $r$  is the radial coordinate, that represents the distance from the cluster centre in this context, and  $M(<r)$  is the total mass contained within  $r$ . Using the equation of state of an ideal gas, Eq.(1.23), to link the pressure to both gas density and temperature, the mass within  $r$  is defined as:

$$M(<r) = -\frac{r}{G} \frac{k_B T}{\mu m_p} \left( \frac{d \ln \rho_{gas}}{d \ln r} + \frac{d \ln T}{d \ln r} \right), \quad (3.2)$$

where  $\mu$  is the mean molecular weight, so  $\mu \approx 0.59$  if a primordial composition is assumed, and  $m_p$  is the proton mass.

It is possible to assume the  $\beta$ -model for the gas density profile, which has been defined in Cavaliere et al. (1976) as follows:

$$\rho_{gas}(r) = \frac{\rho_0}{\left[1 + (r/r_c)^2\right]^{3\beta/2}},$$

in which  $r_c$  is the *core radius* and  $\beta$  is the ratio between the kinetic energy of the tracers used for the gravitational potential (i.e. galaxies) and the thermal energy of the gas:

$$\beta = \frac{\mu m_p \sigma_v^2}{k_B T},$$

where  $\sigma_v$  indicates the one-dimensional velocity dispersion of the considered tracers.

Assuming also a polytropic equation of state:

$$\rho_{gas} \propto P_{gas}^\gamma,$$

where  $\gamma$  is the polytropic index, assumed as  $\gamma \approx 1$  in the first models, Eq.(3.2) becomes:

$$M(<r) \approx 10^{14} \beta \gamma \frac{T(r)}{\text{keV}} \frac{r}{h^{-1} \text{Mpc}} \frac{(r/r_c)^2}{[1 + (r/r_c)^2]} h^{-1} M_\odot, \quad (3.3)$$

where  $T(r)$  is the ICM temperature at the radius  $r$ .

Nowadays, a more general approach is used, instead of assuming both the  $\beta$ -model and  $\gamma \approx 1$  (e.g. Allen et al., 2001; Arnaud et al., 2005). However, also in more general models, the assumptions of the hydrostatic equilibrium and spherical symmetry are held.

### 3.2.2 The self-similar scaling

To explain the physics of the ICM it is possible to assume that only gravity determines its thermodynamical characteristics (for this approach an extensive description is given in Borgani, 2008). With this simply assumption, we expect that the diffuse gas in clusters of different dimensions are the scaled version of each other because gravity does not have preferred scales. Thus, the models following this assumption are the so-called *self similar*. The mass is expressed as follows:

$$M_{\Delta_c} \propto \rho_c(z) \Delta_c R_{\Delta_c}^3, \quad (3.4)$$

where  $M_{\Delta_c}$  is the mass contained within the radius  $R_{\Delta_c}$ ,  $\rho_c(z)$  is the critical density of the Universe and  $\Delta_c$  is a multiplicative factor, and  $\rho_c(z) \Delta_c$  represents the density of the structure, which is referred to both DM and baryonic matter forming the considered cluster. Assuming hydrostatic equilibrium, if  $\rho_{gas}$  is the ICM density, the X-ray luminosity for thermal bremsstrahlung emission is:

$$L_X \propto \int_V \left( \frac{\rho_{gas}}{\mu m_p} \right)^2 T^{1/2} dV.$$

If it is assumed that the gas distribution follows the DM distribution, then

$$L_X \propto M_{\Delta_c} \rho_c T^{1/2}. \quad (3.5)$$

Therefore, the total mass of the cluster is linked with observable quantities that we can measure by modelling the X-ray spectra of the objects assuming that this emission is caused by the bremsstrahlung radiation process.

### 3.2.3 Sunyaev-Zel'dovich effect

As we previously noticed in Section 3.1, the tSZ effect involves electrons situated in the ICM and the CMB photons. This effect can be used to identify clusters, and also their mass (as it has been recently done in Salvati et al., 2018). Indeed, the tSZ effect is characterised by the Comptonization parameter  $y$  that is related to the cluster mass by  $y \propto T M$ , and assuming also the thermal equilibrium,  $y \propto M^{5/3}$ .

### 3.2.4 Virial Theorem

The total mass of a galaxy cluster can also be directly estimated by applying the Virial Theorem. Indeed, the mass can be estimated using spectroscopic measurements of the projected velocity dispersion of the member galaxies, under the assumption of dynamical equilibrium (Binney et al., 1987). Indeed, it is possible to demonstrate, as done in Binney et al. (1987), that:

$$M(r) = -\frac{r \sigma_r^2(r)}{G} \left[ \frac{d \ln \rho}{d \ln r} + \frac{d \ln \sigma_r^2(r)}{d \ln r} + 2\beta(r) \right], \quad (3.6)$$

where  $\rho(r)$  is the galaxy number density,  $\sigma_r$  is the radial component of the velocity dispersion and  $\beta(r) = 1 - \sigma_t^2(r)/\sigma_r^2(r)$  is the *isotropy parameter*, which characterises the ratio of the tangent to the radial dispersion.

For simplicity, we can assume a system characterised by an isotropic velocity field. With this assumption it is possible to apply the Virial Theorem in its scalar form (see Binney et al., 1987), and the total virial mass  $M_V$  is estimated as:

$$M_V = \frac{\sigma^2 R_V}{G} = \frac{3 \pi \sigma_P^2 R_{V,P}}{2G}, \quad (3.7)$$

in which it is assumed that  $\sigma^2 = 3\sigma_P^2$ , for the spherical symmetry,  $R_V$  is the virial radius,  $R_{V,P}$  and  $\sigma_P$  are the projected radius and velocity dispersion along the line-of-sight, respectively.

Therefore, the virial mass of a cluster depends on the global velocity dispersion ( $\sigma$ ) and on the spatial distribution of the galaxy population, indeed we can estimate  $\sigma$  only within the region in which the distribution of galaxies is such that a spectrum can be analysed, because  $\sigma$  is inferred by the spectrum. Moreover, Eq.(3.7) is based on the assumption that the galaxy distribution perfectly follows the DM profile.

### 3.2.5 Luminosity and Richness

It is expensive in terms of telescope time to infer the mass by applying the dynamical approach presented above. In fact, it is necessary to have very accurate spectra for a sufficient number of members to undertake this type of analysis. For this reason, especially when large cluster samples are examined, simpler proxies based on the global optical properties of clusters are considered, as their total optical luminosity ( $L_{op}$ ) or *richness* ( $N_{gal}$ ) that provide a *direct* indication of the mass assuming a scaling relation which links the observable quantity to the mass. These relations are empirically calibrated. The advantage of defining these relations, based on different observable quantities, is that they can be used quickly on large samples. Furthermore, these estimators can be applied to low mass groups that typically lack a sufficient number of member galaxies for a robust dynamical mass estimation, and every time spectra cannot be accurately measured.

$N_{gal}$  and  $L_{op}$  are simply evaluated by counting member galaxies and summing their luminosities, respectively. Both  $N_{gal}$  and  $L_{op}$  must be corrected for the expected contamination by field galaxies (see Section 5.2.1). These types of optical scaling relations are generally more difficult to interpret because their behaviour cannot be predicted from simple physics arguments because the observed galaxy properties are the results of the complex and non-linear process of galaxy formation and evolution. Indeed, optical scaling relations can only be calibrated empirically.

## 3.3 Detection of clusters

### 3.3.1 Identification in the X-ray band

As we said, since the first attempts to map the X-ray sky, clusters were associated with extended sources, caused by thermal bremsstrahlung from ICM. Currently, thanks to the much improved in X-ray instruments, X-ray surveys are recognised as an efficient method for constructing samples of galaxy clusters out to cosmological redshifts.

Using X-ray surveys has many advantages: firstly, the X-ray selection reveals physically-bound systems, because the diffuse thermal emission from ICM is explained by the existence of a potential-well within which the gas is in dynamical equilibrium with the cool baryonic matter (galaxies and stars within ICM) and the DM; moreover, the X-ray luminosity is well correlated with the cluster mass (Eq.3.5); furthermore, clusters are high contrasted objects in the X-ray sky; finally, a fundamental advantage of X-ray selection is the possibility to define the flux limit in our survey leading to a simple evaluation of the survey volume and therefore to a simple computation of space densities and is easiest than in optical survey have an accurate selection function.

### 3.3.2 Identification through the SZ effect

The tSZ effect allows to identify galaxy clusters by measuring the distortion of the CMB spectrum caused by the ICM. The main property of this effect is the fact that its surface brightness is redshift-independent, therefore providing nearly mass-limited cluster samples from high-resolution mm surveys at arbitrarily high redshift (e.g. Salvati et al., 2018). Moreover, this method provides in principle a reliable estimate of cluster masses (see Par.3.2.3).

### 3.3.3 Identification in optical surveys

In Optical and Near Infrared bands surveys, clusters of galaxies are identified by looking for overdensities of galaxies. With this type of detection, the main problems are to distinguish between proper physical clustered objects from clumps caused by random alignments and non-collapsed overdensities, and to discriminate member galaxies from the field ones. In order to

identify the member galaxies, one of the possibilities is to derive the galaxy redshifts from their emission spectrum or to estimate through photometry the *photometric redshift* (discussed in Section 4.4.1), that is less precise than the spectroscopic ones.

Hence, the projection of galaxies along the line of sight affects the searching of clusters through identification of overdensities in optical and overdensities surveys and this effect increases at high redshift because of the accumulated field galaxies signal. This effect increase with redshift until the overdensity produced by a galaxy cluster becomes almost impossible to detect, except for the richest clusters. The problem of projection contamination has caused optical searches to be considered as implausible, and, in particular, their selection functions difficult to quantify (see Yee et al., 2002) while in X-ray it is possible to obtain with high accuracy.

However, ongoing and upcoming photometric surveys are going to increase the current census of galaxies by orders of magnitude, pushing the limits of detection towards lower masses and higher redshifts and so, these new data are meant to be used also for searching galaxy clusters as overdensities produced by these galaxies. In particular, in order to use this amount of photometric data for cosmological studies, it is necessary to link the measured properties of the member galaxies to the total cluster mass.

Unluckily, scaling relations between the mass and any galaxy observable can only be calibrated empirically, as we said in Par.3.2.5. Various different mass proxies for photometric data have been suggested in the literature so far: the most used ones are based on the number of (red) galaxies inside a given radius (e.g. Andreon et al., 2010), on photometric stellar mass estimates (i.e. Pereira et al., 2018) and on their luminosities (e.g. Mulroy et al., 2014).

Currently, galaxy clusters are detected, in photometric surveys, by running algorithms which search for not-negligible cluster-scale overdensities in the galaxy distribution. Usually one or more observables, related to the properties and abundance of galaxies, are estimated and considered during selection clusters procedure, indeed mass proxies, and also the derived mass-scaling relations, are often estimated directly by the cluster finders (e.g. Simet et al., 2017).

One of the most used method is using the redMaPPer cluster finding algorithm, a cluster finder specifically designed to make optimal use of ongoing and near-future large photometric surveys (presented in Rykoff et al., 2014). In brief, redMaPPer utilises all the band used to study the survey to self-calibrate a model for redsequence galaxies. The obtained model is then used to detect clusters as red galaxy overdensity, while simultaneously estimating the probability that each red galaxy is a cluster member. The cluster richness  $\Lambda$  is the sum of the membership probabilities over all the red galaxies attributed to the detected cluster.

In 5 we investigate another algorithm, called AMICO, developed for searching galaxy clusters in photometric survey. In particular, we discuss its application on the Kilo-Degree Survey that lead to the cluster catalogue studied in this Thesis. Also with this algorithm the richness is defined exploiting statistical information about membership.

### 3.4 Clusters as a cosmological probe

Galaxy clusters are the largest and most massive, gravitational bound structures in the Universe, therefore the highest density peaks in the large-scale structure of the Universe are traced by them.

Their properties are functions both of the underlying cosmology and of the processes operating within them. However, the description of the cosmic structure formation for these objects is relatively simple since gas dynamical effects are negligible than inside galaxies. In fact, on scales smaller than cluster ones, instead, the complex astrophysical processes, related to galaxy formation and evolution, become relevant and it is necessary to take into account also gas physics. Therefore, galaxy clusters mark the transition between linear (or weakly-non linear) regime and non-linear one.

The possibility of modelling their statistical properties as a function of cosmological parameters, combined with the capability of measuring their basic properties, such as the mass, as discussed previously in this Chapter, makes them optimal tracers of the large scale structure of the Universe.

The clustering properties (discussed in the next Chapter) of the large-scale distribution of galaxy clusters provide direct information on the shape and amplitude of the underlying DM power spectrum. Furthermore, the evolution of these clustering properties is sensitive to the

value of the density parameters through the linear growth rate of perturbations (see Section 4.4.2). A powerful strategy is to extract cosmological information from the two-point correlation function or power spectrum of galaxy clusters as a standalone (e.g. Estrada et al., 2009; Marulli et al., 2018) or in a joint analysis with mass function measurements (see Mana et al. (2013a) and reference therein), with the lensing information (e.g. Sereno et al., 2015b). Indeed, these constraints are even more powerful when combined with, or compared to, results from other observables such as primary temperature and polarization anisotropies of the CMB radiation and baryon acoustic oscillations (BAO) (e.g. Salvati et al. (2018)).

In this Thesis work, we focus on the possibility to constrain some cosmological parameters and the scaling relation that links photometric characteristics of clusters to their masses, exploiting the correlation function (see Chapter 6). In Section 7, we present a detailed overview on the main cosmological work carried out exploiting cluster clustering signal.

# Chapter 4

## The correlation function

In this Chapter we discuss the *clustering* properties of the large-scale structure of the Universe. In particular, this analysis focuses on the correlation functions because the two-point-correlation function is exploited in our work (as it will be discussed in Chapter 6). The two-point correlation function will be presented with both its theoretical definition and its estimators (Section 4.2 and Section 4.2.1, respectively). We will discuss the main problems in the detection of the clustering signal using the correlation function. i.e. geometric distortions and dynamical distortions, and how to avoid them through the use of different estimators, in particular introducing the projected correlation function.

### 4.1 Clustering

The term *clustering* refers to the grouping of the structures of the Universe into larger systems. As we have discussed in Chapter 2, according to the modern cosmological scenario, the aggregation of structures is caused by a bottom-up merging process. Indeed, in this scenario, the larger structures are formed by the continuous merging of smaller structures. Thus, this process leads to the formation of the objects that we observe in the Universe today. Therefore, studying the clustering properties means to carry out a study of the large-scale structure of the Universe.

In Chapter 2, we have also introduced the statistical framework on which this investigation is built on. In particular, we have characterised the power spectrum  $P(k)$ , that according to the Wiener-Khinchin theorem, is the equivalent in the Fourier space of the correlation function  $\xi(r)$  in the real space. In fact, these two definitions are linked by Fourier transforms as follows:

$$\begin{aligned} P(k) & \xrightarrow{a-FFT} \xi(r) \\ \xi(r) & \xrightarrow{a-FFT} P(k), \end{aligned}$$

in which  $P(k) \propto \langle \delta^2(\vec{k}) \rangle$  and  $\xi(\vec{r}) = \langle \delta(\vec{x}) \delta(\vec{x} - \vec{r}) \rangle$ .

In our theoretical framework, both the correlation function and the power spectrum describe the statistics of the perturbed density field. The global statistical properties of the Universe, discussed in Chapter 2, cannot be easily observed. Instead, one can observe discrete tracers of the DM density field.

However, measuring the clustering of cosmic tracers (such as galaxies and galaxy clusters), is not the same as measuring the clustering of the perturbed density field. Indeed, moving from theory to observations, we have to take into account that we cannot observe the punctual density contrast,  $\delta(x)$ , but only discrete tracers in a finite volume. Moreover, the possible tracers are *biased* with respect to the density field in a way not easy to model, as mentioned before in Section 2.4.1, and it will be discussed later in this Chapter.

Thus, it is only possible to measure the *smoothed* version of the density field in a finite volume through our surveys. Furthermore, our measures have statistical errors caused by both the limitedness of the volumes (cosmic variance) and the finite number of sources used to trace the underlying density field (shot noise).

The correlation functions have been the standard way of describing the clustering in cosmology since the pioneering studies carried out during the 1960s and 1970s (e.g. see Totsuji et al., 1969 and Peebles, 1974). Indeed, the correlation functions furnish a description of the clustering properties of a set of objects (e.g. galaxies or galaxy clusters in our cosmological surveys) distributed in space.

To infer the correlation function, it is necessary to know the distance between the tracers, but only a rough estimate is possible. Indeed, the source coordinates are estimated using their redshifts, which is not a pure distance indicator (see Section 4.4). Moreover, our estimations have errors due to cosmic variance and to the shot noise. One of the main issues is that we have to assume a fiducial cosmological model to compute the comoving distances leading to *geometric distortion* (as it will be discussed in Section 4.3). In the detected clustering signal there are also *dynamical distortions* caused by the peculiar velocities (see Section 4.4.2) that influence the observed redshift.

## 4.2 The Two-Point Correlation Function

The two-point correlation function (2PCF), as defined in Peebles (1980), is related to the joint probability of findings a pair of objects (e.g. galaxies or galaxy clusters) in two comoving volumes,  $dV_1$  and  $dV_2$ , separated by a comoving distance  $r_{1,2}$ :

$$\delta P = \bar{n}^2 [1 + \xi(\vec{r}_{1,2})] \delta V_1 \delta V_2, \quad (4.1)$$

where  $\bar{n}$  is the mean number density,  $\bar{n} dV_i$  is the stochastic probability of finding an object in  $dV_i$ , and  $\xi(r_{1,2})$  is called the *spatial two-point correlation function*. Therefore, the 2PCF quantifies the deviation of the objects distribution from that expected for a random distribution of tracers. From this definition, it is clear that  $\xi(\vec{r}_{1,2}) = 0$  means that the considered tracers are completely independent and randomly distributed; if instead  $\xi(\vec{r}_{1,2}) > 0$ , the objects are correlated, so to find an object in each of the two volumes is more probable than for a random distribution; then, if  $\xi(\vec{r}_{1,2}) < 0$ , there is anti-correlation, so finding a pair is less probable than for a random distribution. Since the probability values must be comprised between zero and one, the 2PCF cannot assume all the real values, but only  $\xi \geq -1$  is acceptable.

The number of objects contained within a radius  $r$  around a given one, is definable by the spatial 2PCF as follows:

$$N(< r) = \frac{4\pi}{3} \bar{n} r^3 + 4\pi \bar{n} \int_0^r r'^2 \xi(r') dr', \quad (4.2)$$

where the first term on the right-hand side represents the probability to have an object contained within the radius  $r$  for a random distribution, while the second term takes into account the deviation from the random distribution.

### 4.2.1 The 2PCF estimators

As we mentioned above, from a practical point of view, the clustering investigation is possible only through the observation of discrete tracers, like galaxies or galaxy clusters. Therefore, in order to study clustering through our cosmological surveys, we need observable estimators to use Eq.(4.1) for discrete tracers.

As a first step, we can define  $dP_{12}$ , as binned in shells of width  $\Delta r$ , as follows:

$$dP_{12} = \frac{DD(r)}{N_{DD}}, \quad (4.3)$$

where  $DD(r)$  represents the total number of object pairs separated by a distance  $r \pm \Delta r$ , and  $N_{DD}$  is the total number of pairs in the sample:

$$N_{DD} = N_D \frac{(N_D - 1)}{2},$$

where  $N_D$  is the number of available data. Moreover, also the term  $\bar{n}^2 dV_1 dV_2$  in Eq.(4.1) has to be re-written in such a way to be related to observable quantities. This term describes the

uncorrelated probability of finding a pair of objects and must hold all the geometrical properties of the volume sampled by the data. Indeed, considering the distribution of the tracers, the 2PCF at a given distance  $r$  is estimated by counting and averaging the number of neighbours each object has at a given scale. It is clear that the boundaries of the sample have to be considered because, as the tracers cannot be observed beyond the boundaries, the number of pairs is systematically underestimated at larger distances. The geometrical properties of the sample are considered by extracting random data points from the survey volume, and computing random pairs, as well as for data, obtaining:

$$\bar{n}^2 dV_1 dV_2 = \frac{RR(r)}{N_{RR}}, \quad (4.4)$$

where  $RR(r)$  and  $N_{RR}$  correspond to  $DD(r)$  and  $N_{DD}$  but for a random collection of points, so characterised by null clustering ( $\xi(r) = 0$ ).

Hence, substituting in Eq.(4.1) these two new quantities, we obtain the Peebles and Hauser unbiased estimator of the correlation function (Peebles et al., 1974), expressed as:

$$\xi_{PH}(r) = \frac{N_{RR}}{N_{DD}} \frac{DD(r)}{RR(r)} - 1. \quad (4.5)$$

Landy et al. (1993) introduced another estimator characterised by a lower variance. This estimator, called Landy-Szalay (LS) *estimator*, is given as:

$$\xi_{LS}(r) = \frac{N_{RR}}{N_{DD}} \frac{DD(r)}{RR(r)} - 2 \frac{N_{RR}}{N_{DR}} \frac{DR(r)}{RR(r)} + 1, \quad (4.6)$$

where the  $DR(r)$  term is the number of data-random cross pairs and  $N_{DR} = N_D N_R$  is the total number of cross pairs. Furthermore, in order to have an estimator of the correlation function which variance is not affected by discrete pair counts from the random sample, the random collection of point should be larger than the clustered one.

In the analysis presented in this dissertation, discussed in Chapter 6, the correlation function is calculated by the LS estimator. This estimator is chosen because its variance is almost completely Poissonian, with an error that depends on the number of pairs in the catalogue (see Landy et al., 1993). Moreover, this estimator is widely used in clustering studies also because at large scales the performance of the Landy and Szalay estimator has been proved to be better than other proposed estimators (Kerscher et al., 2000) and was validated against distributions with known correlation signal (e.g. Hamilton, 1992; Labatie et al., 2010).

### 4.3 Geometric distortions

When a fiducial cosmology, different to the true one, is assumed to convert observed coordinates to physical ones, geometric distortions appear. In fact, the effect of this assumption is to alter distances of the tracers differently in radial and angular directions, since  $D_A(z)$  and  $H(z)$ , defined in Eqs.(1.15)-(1.29), depend in a different way on cosmological parameters and redshift. As a first approximation, the effect of the geometrical distortion is an equal shift over all the scales.

The relation that links the observed coordinates to the physical ones can be written as follows:

$$ds^2 = \left[ (1+z)^2 D_A(z)^2 \frac{cz}{H(z)} \right] d\Omega dz, \quad (4.7)$$

where the term in parentheses is the Jacobian transformation,  $ds^2$  is the volume elements in physical coordinates while  $d\Omega dz$  is the volume expressed in observed coordinates. The average distance of the volume,  $D_v(z)$ , is expressed as:

$$D_v(z) = \left[ (1+z)^2 D_A^f(z)^2 \frac{cz}{H^f(z)} \right], \quad (4.8)$$

where  $H^f(z)$  and  $D_A^f(z)$  are calculated in the assumed fiducial cosmology. Thanks to the definition of  $D_v(z)$ , a cosmology-independent quantity,  $y_s$ , is definable. Therefore, it is possible to extract unbiased results for the 2PCF, performing the transformation from  $s$  to  $y_s$ , where

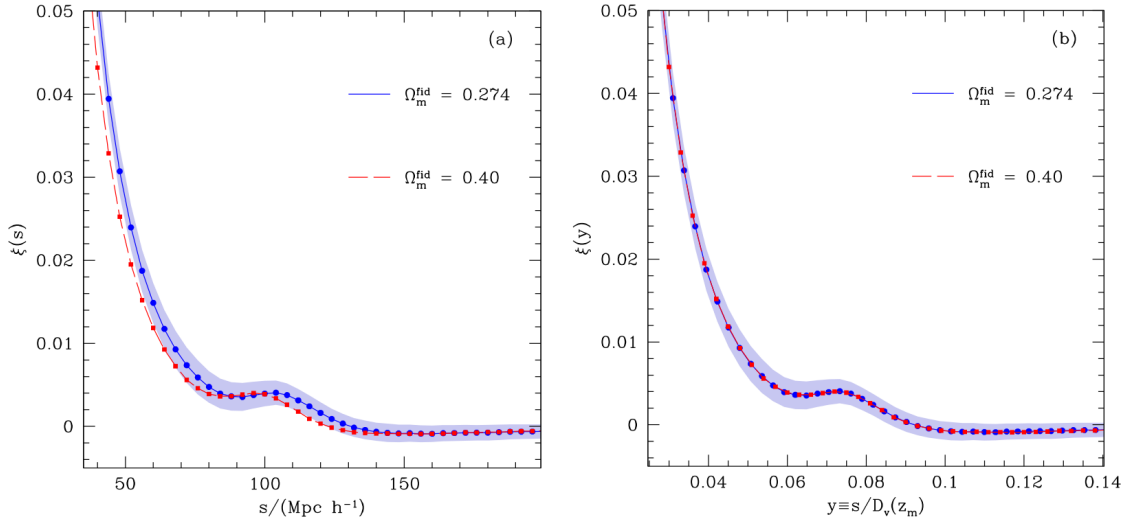


**Figure 4.1:** *Left panel:* measure of 2PCF monopole for a set of simulated data using two different fiducial cosmology characterised by different  $\Omega_M^f$  ( $\Omega_M^f = 0.257$  in blue,  $\Omega_M^f = 0.4$  in red; the blue shaded region represents the typical variance of the data). *Right panel:* measure of 2PCF monopole for the same data but expressed through  $y_s$ , removing in this way the dependence on the fiducial cosmology. Credits to: Sánchez et al. (2017).

$y_s \equiv s/D_V^f(z)$ . This has been done in Sánchez et al. (2017), in which the monopole of the 2PCF measured with two different cosmological models is compared to the monopole of the 2PCF for the same data but with the modelling of the geometric distortions obtained by performing the transformation  $s \rightarrow y_s$  (the results are shown in left and right panels in Fig.4.1, respectively).

## 4.4 Redshift-space distortions

The use of the redshifts as distance proxies induces other kind of distortions. Indeed, the observed redshift,  $z_{obs}$ , depends on different quantities:

$$z_{obs} = z_c + \frac{v_{\parallel}}{c} (1 + z_c) \pm \sigma_z, \quad (4.9)$$

where  $z_c$  is the *cosmological redshift*, due to the Universe expansion,  $\sigma_z$  is the error on the measurements and  $v_{\parallel}$  is the component of the peculiar velocity along the line of sight. Therefore, if we use  $z_{obs}$  to estimate the comoving distance, we will have distortions in our measures of the 2PCF, not only because of the error on the measurement ( $\sigma_z$ ) but also because  $z_{obs}$  encodes information about the peculiar motions along the line of sight ( $v_{\parallel}$ ). The peculiar motions cause the so-called *dynamical distortions*, an effect commonly known also as redshift-space distortions (RSD).

### 4.4.1 The Photometric redshifts

For our studies, we want to obtain the cosmological redshift because it is related to the distance of the observed objects via Eq.(4.9) and so, the estimation of  $z_c$  is complicated by the dependencies over the error on the measurement ( $\sigma_z$ ) and by the peculiar motions along the line of sight ( $v_{\parallel}$ )

To calculate the distances from the redshift, it is necessary to have the term  $\sigma_z$  in Eq.(4.9) as small as possible. This term becomes negligible when spectroscopic redshifts is used, while, generally, for photometric redshifts cannot be neglected.

The photometric redshift technique has been used for the first time in the 1960s (Baum, 1962) but this method of estimation was supplanted in the 1970s and 1980s by the spectroscopic technique, because through the study of the spectra details, as we mentioned above, the observed redshift has negligible errors compared to the photometric one. Nowadays, as a result of the ongoing and upcoming large sky surveys, the photometric redshift technique is widely used again, because, over large samples, spectroscopic data cannot be easily obtained, because of the hugely amount of time requested for employ this techniques over a large sample.

Triggered by the necessity of using photometric data, and so by the increasingly more stringent requirements on the photometric redshift accuracy, during the last years various and new techniques have been proposed to obtain more accurate photometric redshifts, such as template-fitting and machine learning (a review over these techniques is given by Salvato et al., 2019).

Our work is conducted on the AMICO-KiDS catalogue, that we will present in Chapter 5, obtained by extraction of clusters from the KiDS survey (see de Jong et al., 2017), through the AMICO algorithm (described in Section 5.2). Hence, all our analysis is performed on photometric data (a detailed description of the technique used to estimate photometric redshifts in KiDS data is presented in Bilicki et al., 2018). Hence, it is important in this case to accurately take into account the errors on the observed redshifts. Therefore, for modelling the 2PCF monopole, we have modelled the errors on the photometric redshift measurements in the likelihood, discussed in Section 4.5.2.

#### 4.4.2 The 2D 2PCF estimators and dynamical distortions

Geometrical and dynamical distortions impact on the shape of the 2PCF introducing predictable anisotropic effects. In order to study the correlation function signals, we have to properly model these distortions effect. These two kinds of distortions can be disentangled exploiting at the *2D 2PCF* at sufficiently large scales (Marulli et al., 2012).

In analogy with the definition of the one dimensional version of 2PCF, expressed in Eq.(4.6), the 2D 2PCF LS estimator is given as:

$$\xi(r_p, \pi) = \frac{DD(r_p, \pi) + RR(r_p, \pi) - 2DR(r_p, \pi)}{RR(r_p, \pi)} \quad (4.10)$$

where  $DD(r_p, \pi)$ ,  $RR(r_p, \pi)$ ,  $DR(r_p, \pi)$  are the data-data, random-random, data-random pairs, counted in bins with comoving separations given by  $\Delta r_p$  and  $\Delta \pi$ , in radial and transverse direction to the line-of-sight, respectively. In real space and with no geometric distortions, assumed the true cosmology,  $\xi(r_p, \pi) \equiv \xi(r)$ , with  $r = \sqrt{r_p^2 + \pi^2}$ .

While the geometric distortions are invariant over different scales, as we mentioned above, the dynamical distortions change with scale. Indeed, on small scales,  $r < 1 h^{-1}$  Mpc, we observe galaxies inside large virialised DM haloes (as galaxy clusters or galaxy groups) that are characterised by a random motion due to the potential in which they are immersed. This influences how we see these galaxies in the redshift space. Indeed the correlation function  $\xi(r_p, \pi)$  appears stretched along the radial direction causing the so-called *fingers of God structures*; over larger scales, the redshift deviations are caused by the bulk motion of galaxies that fall in larger forming structures. As a result, the redshift-space correlation function  $\xi(r_p, \pi)$  appears *squashed*. In particular, the distortions on large scale satisfy the following relation:

$$\vec{v} = \frac{2}{3} \frac{G \rho_c a}{H} f(\Omega_M), \quad (4.11)$$

where  $f$  is the growth rate, defined in Eq.(2.26). In the standard cosmological framework, it can be demonstrated that  $f$  can be approximated as follows:

$$f \approx \Omega_M^\gamma, \quad (4.12)$$

with  $\gamma = 0.545$  for GR (Kaiser, 1987; Peebles, 1980; Linder et al., 2003). Different  $\gamma$  values are obtained for different gravity models. Therefore, it is also possible to test the GR and the modified gravity models, through the growth factor (as done e.g. in Alam et al., 2016b; Alam et al., 2016a; a review is given in Huterer et al., 2015). The first RSD measurements were exploited primarily to estimate  $\Omega_M$ , that can be derived directly from Eq.(4.12) once  $f(z)$  is estimated (see e.g. Peacock et al., 2001).

The scale-dependence of redshift-space distortions in  $\xi(r_p, \pi)$  are shown in Fig.4.2, in which, in particular, it is illustrated a comparison between the galaxy clustering measured from the SDSS in redshift-space and a theoretical expectation obtained in the standard  $\Lambda$ CDM scenario (He et al., 2018).

Therefore, the peculiar velocity field, on large scale, provides key cosmological information (e.g. Kaiser (1987)). One of the most promising ways to constrain the growth rate is to exploit the distortion in the clustering of galaxies caused by peculiar motions.

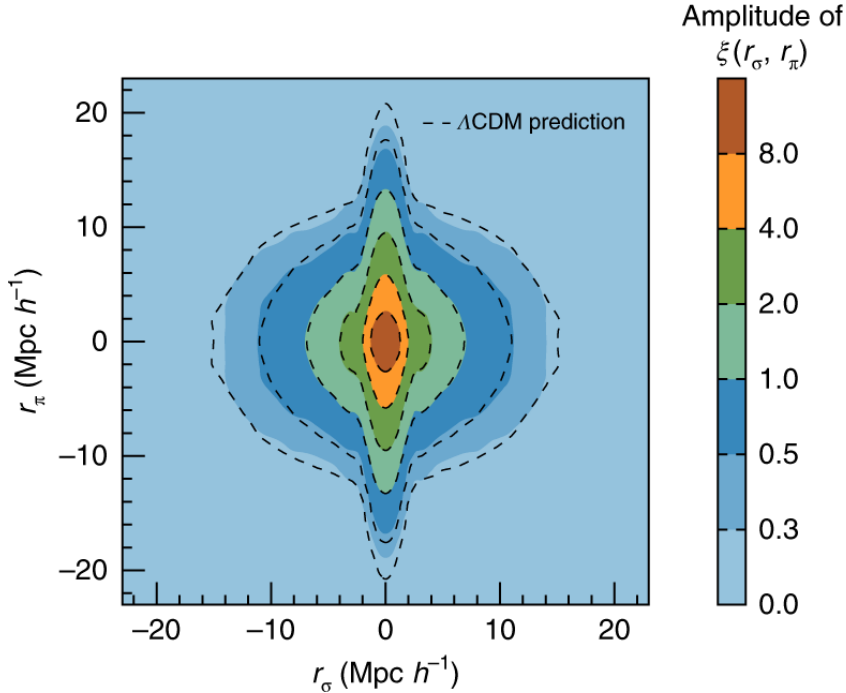


**Figure 4.2:** Correlation function in the *redshift-space*. The colour-coded contours show the amplitude of the two-point correlation function  $\xi(r_\sigma, r_\pi)$ , where  $r_\sigma$  indicates the transverse separation, while  $r_\pi$  refers to the radial one. The measurement is replicated over different scales to highlight the deviations from circular symmetry, produced by galaxy peculiar velocities when observed redshifts are used as a proxy for distance. The black dashed lines represent the corresponding prediction of  $\Lambda$ CDM scenario obtained from a mock galaxy survey. Credits to: He et al. (2018)

In conclusion, these distortions could be used to obtain cosmological information by studying the distortions themselves or, alternatively, by subtracting these distortions and studying the correlation function signals.

## 4.5 2PCF measures

As we mentioned, the use of correlation functions to investigate the large-scale structure of the Universe was first suggested in the 1960s (Totsuji et al., 1969). Then, during the 1970s, Peebles and his team undertook a program to evaluate estimates of these functions from the Lick galaxy catalogue and other data sets (Peebles, 1980; Peebles, 1974). All these works were done on the *projected distribution* of galaxies since little or no redshift information was available. The central discovery was that, over galaxy scales, the 2PCF is a simple function having a power-law form. This result has stood firm through numerous analyses of diverse catalogues over the subsequent decades (a review over these results is given, for example, in Jones et al., 2004). Observing also galaxy clusters, it is discovered that, at intermediate scales,  $10 \leq r \leq 100 \text{ Mpc}/h$ ,  $\xi(r)$  can be described as follows:

$$\xi(r) = \left( \frac{r}{r_0} \right)^{-\gamma}, \quad (4.13)$$

where  $r_0$  is called *correlation scale* (e.g. in Pan et al. (2000) is obtained  $\gamma \simeq 2.26$  for  $r < 10 \text{ Mpc } h^{-1}$ , while, for  $10 < r < 30 \text{ Mpc } h^{-1}$ ,  $\gamma$  is  $\simeq 2.71$ ).

The galaxy correlation scale length appears as a function of galaxy luminosity, morphological or spectral type, color, stellar mass, and redshift (a review over this topic is presented, for example, in Coil, 2013). In Marulli et al. (2013) these relations are investigated, confirming the increasing of the clustering length  $r_0$  both as a function of B-magnitude and stellar mass, as shown in Fig. 4.3. It is also demonstrated that  $r_0$  increases with the luminosity, especially at higher redshift.

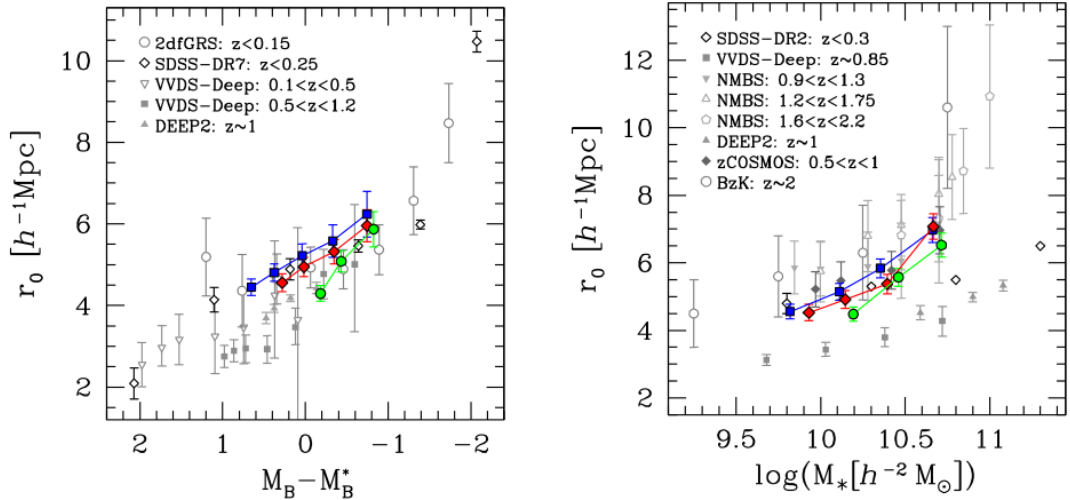


**Figure 4.3:** *Left panel:* Best-fit values of the correlation length  $r_0$  as a function of B-band absolute magnitude. *Right panel:* Best-fit values of the correlation length  $r_0$  as a function of stellar mass. VIPER constraints in three different redshift bins are shown ( $0.5 < z < 0.7$  with blue squares;  $0.7 < z < 0.9$  with red diamonds;  $0.9 < z < 1.1$  with green circles). The grey symbols represents constrains from other catalogues. Credits to: Marulli et al. (2013).

However, if we consider Eq.(4.2), for  $r \rightarrow \infty$ , the number of counts is expected to tend to the average density of the Universe:

$$\int_0^r r'^2 \xi(r') dr' \xrightarrow{r \rightarrow \infty} 0, \quad (4.14)$$

that means  $\xi(r)$  over larger scale must become negative and consequently cannot be simply described as Eq.(4.13) with a different correlation-scale.

#### 4.5.1 Projected and real-space correlations

In our work, to correct for redshift-space distortions due to galaxy peculiar velocities and to derive the 2PCF in real space,  $\xi(r)$ , we first measure the 2PCF with Eq.(4.10), using the LS estimator. Then, we integrate along the line of sight,  $\pi$ , as:

$$w_p(r_p) = 2 \int_0^{\pi_{max}} d\pi' \xi(r_p, \pi'). \quad (4.15)$$

The real-space correlation,  $\xi(r)$ , can be estimated by deprojecting  $w_p(r_p)$  as:

$$\xi(r) = -\frac{1}{\pi} \int_r^\infty dr'_p \frac{dw_p(r'_p)/dr'_p}{\sqrt{r_p'^2 - r^2}}.$$

In our work, we assume that  $\xi(r)$  can be described by Eq.(4.13). Thank to this assumption, Eq.(4.15) can be solved analytically:

$$w_p(r_p) = r_p \left( \frac{r_0}{r_p} \right)^\gamma \frac{\Gamma(\frac{1}{2})\Gamma(\frac{\gamma-1}{2})}{\Gamma(\frac{\gamma}{2})}. \quad (4.16)$$

where  $\Gamma$  is the *Gamma function*. The parameters  $\gamma$  and  $r_0$  can be obtained by a power-law fit to  $w_p(r_p)$ .

In our work, this analysis is done once the 2D 2PCF of galaxy clusters of AMICO-KiDS catalogue is measured, using different fiducial cosmologies. Thus, we model the 2D 2PCF using Eq.(4.16) and, in this way, we estimate  $r_0$  and  $\gamma$  (the full description of our results obtained through this investigation is reported in Chapter 6).

## 4.5.2 The 2PCF in the redshift-space

As we discussed above, large photometric redshift (photo-z) errors influence the measured  $\xi(s)$ . The real-space clustering can be derived by projecting the correlation function along the line of sight, as described in the previous Section. However, it is also possible to fit directly the redshift-space clustering with a model that takes into account both the redshift-space distortions and the photo-z uncertainties. In our work, we use this model also to constrain both cosmological parameters (discussed in Section 6.5) and the scaling relation (examined in Section 6.6), ignoring geometric distortions, whose effect is negligible with respect to dynamic distortions and photo-z errors (see Marulli et al., 2012).

The redshift-space 2D power spectrum can be modelled in polar coordinates as

$$P(k, \mu) = P_{DM}(k) (b + f\mu^2)^2 \exp(-k^2 \mu^2 \sigma^2), \quad (4.17)$$

as derived in Kaiser (1987), where  $k = \sqrt{k_{\perp}^2 + k_{\parallel}^2}$ , in which  $k_{\parallel}$  and  $k_{\perp}$  are the wave-vector components parallel and perpendicular to the line of sight, respectively;  $\mu$  is equal to  $k_{\parallel}/k$ ;  $b$  is the linear bias factor (discussed below in Section 4.6);  $f$  is the growth factor (Eq.4.12); the  $f\mu^2$  term parametrises the coherent motions of large-scale structures, enhancing the clustering signal at all scales. The exponential cut-off term describes the random perturbations of the redshifts caused by both non-linear stochastic motions and redshift errors. It is a Gaussian damping term that removes the signal over a typical scale  $k \sim 1/\sigma$ , thus causing a scale-dependent effect, where  $\sigma$  is the displacement along the line of sight due to random perturbations of cosmological redshifts, defined as

$$\sigma = \frac{c \sigma_z}{H(z_m)}, \quad (4.18)$$

where  $H(z_m)$  is the Hubble function computed at the median redshift of the sample  $z_m$  and  $\sigma_z$  is the typical photo-z error.

To derive the monopole of the correlation function, we integrated Eq.(4.17) over the angle  $\mu$ , and then Fourier anti-transformed the result.

The solution can be written as follows

$$\xi(s) = b^2 \xi'(s) + b\xi''(s) + \xi'''(s), \quad (4.19)$$

where, the main term,  $\xi'(s)$ , is the Fourier anti-transform of the monopole  $P'(k)$ , that is:

$$P'(k) = P_{DM}(k) \frac{\sqrt{\pi}}{2k\sigma} \operatorname{erf}(k\sigma), \quad (4.20)$$

while,  $\xi''(s)$  and  $\xi'''(s)$ , are the Fourier anti-transform, respectively, of  $P''(k)$  and  $P'''(k)$ , that are defined as:

$$P''(k) = \frac{f}{(k\sigma)^3} P_{DM}(k) \left[ \frac{\sqrt{\pi}}{2} \operatorname{erf}(k\sigma) - k\sigma \exp(-k^2\sigma^2) \right]$$

$$P'''(k) = \frac{f^2}{(k\sigma)^5} P_{DM}(k) \left\{ \frac{3\sqrt{\pi}}{8} \operatorname{erf}(k\sigma) - \frac{k\sigma}{4} \left[ 2(k\sigma)^2 + 3 \right] \exp(-k^2\sigma^2) \right\}$$

This approach is followed in Sereno et al. (2015b).

## 4.6 Bias

The main complication affecting clustering studies is that all tracers that we can observe, such as galaxies or galaxy clusters, do not exactly trace the DM density field. Generally, the density contrast of tracers of the sample population,  $\delta_o$ , can be expressed as a function of the total density field,  $\delta_m$ , as:

$$\delta_o = f(\delta_m), \quad (4.21)$$

where  $\delta_o$  is the density field derived from a discrete distribution, that has to be averaged on a volume  $dV$ . This definition implicitly ensures all the processes involved in structures formation

and evolution. These process may depend over some observables such as the halo mass, the total magnitude, the richness etc.

We can assume that the function  $f$  is linear, so

$$\delta_o = b\delta_m \quad (4.22)$$

where  $b$  is called the *bias factor*. When  $b > 1$  the considered tracers have higher *clustering* than DM, so these tracers are higher peaks in the density field. From Eq.(2.29) and Eq.(4.22) we can derive

$$b = \sqrt{\frac{\xi_o(r)}{\xi_{DM}(r)}}, \quad (4.23)$$

where  $\xi_{DM}(r)$  is the correlation function of the matter distribution. The fact that the luminous matter is a biased tracer of the total density field first discovered by Kaiser (1984), who compared clustering results of galaxies and galaxy clusters, finding that clusters have higher correlation than galaxies. In fact, rare objects such as clusters show greater clustering signal since they can only form at the highest peaks of DM density field.

#### 4.6.1 Theoretical bias models

Theory and numerical simulations show that the bias is complicated to model: it is stochastic, and it depends on object properties such as the luminosity, mass, redshift. Our ignorance on the bias impacts the cosmological constraints we can derive from clustering measurements. A common strategy is to consider the bias as a nuisance parameter. Specifically, the bias is highly degenerate with the amplitude parameters such as the initial power spectrum normalisation or the density fluctuations growth rate. Information complementary to the density field statistics is required to break this degeneracy. Combining number counts and clustering of massive objects, such as galaxy clusters, is thus a possible way to break degeneracies (Mana et al., 2013b; Sartoris et al., 2016).

Standard theoretical models predicts that the DM halo bias depends on halo mass and redshift. Specifically, at a fixed redshift, the bias increases with the tracers' mass, while for a given mass, the bias is an increasing function of the redshift (e.g. Sheth et al., 1999). The effective bias of DM haloes with masses in a given range and at a given mean redshift can be estimated as:

$$b_{eff}(z) = \frac{\int_{M_{min}}^{M_{max}} dM b(M, z)\Phi(M, z)}{\int_{M_{min}}^{M_{max}} dM \Phi(M, z)} \quad (4.24)$$

where  $\Phi(M, z)$  is the halo mass function, and  $M_{min}$  and  $M_{max}$  are the lowest and largest masses in the sample, respectively.

In Chapter 6, in order to evaluate the theoretical bias of our cluster catalogue, we will assume specific models to compute the mass function  $\Phi(M, z)$  and the bias  $b(M, z)$ . Specifically, Eq.(4.24) is computed with the CosmoBolognaLib (CBL, presented in Marulli et al., 2016) using either Code for Anisotropies in the Microwave Background (CAMB, <http://camb.info>) or the Eisenstein and Hu code (<http://background.uchicago.edu/~whu/transfer/transferpage.html>) to compute the matter power spectrum and mass variance. The Tinker model (a detailed description is given in Tinker et al., 2010) will be assumed to described the linear bias, that is defined as follows:

$$b(\nu) = 1 - A \frac{\nu^\alpha}{\nu^\alpha + \delta_c^\alpha} + B\nu^\beta + C\nu^c, \quad (4.25)$$

where  $\nu = \delta_c/\sigma_M$  and  $A, B, C, \alpha, \delta$  are expressed as function of  $y \equiv \log_{10} \Delta$ , where  $\Delta$  is an assumed multiple of the background density, that links the density of the considered collapsed structure with the background density (a detailed description is given in Tinker et al., 2010).

The capability of measuring accurate cluster masses is crucial in order to constrain their effective bias as a function of the cosmological model, something that is not possible with galaxies and other cosmic tracers. Indeed, theory and numerical simulations shows that the galaxy bias is extremely complicated to model: it is stochastic, it depends on galaxy properties such as luminosity, colour and/or morphological type, and it is scale dependent on small scales (as shown in Marulli et al., 2013). The proper treatment of how galaxies populate dark mat- ter

haloes, assembly bias, and baryonic effects on the matter power spectrum on small scales requires a very accurate modelling. If the adopted scheme is too restrictive and fails to account for some important features, the constraining power on cosmological parameters is limited and the results can be severely biased. Therefore, using galaxy cluster to constrain cosmological parameter has this great advantage.

## Chapter 5

# The AMICO-KiDS galaxy cluster catalogue

In this Chapter, we present the AMICO-KiDS galaxy cluster catalogue on which our work is based. At first, we briefly summarise the characteristics of the photometric Kilo-Degree Survey as the AMICO-KiDS catalogue is built by extracting clusters from this survey employing the AMICO code. Then, we focus on how this extraction has been performed by the AMICO algorithm.

Specifically, in Section 5.2.1, we summarise the main characteristics of the AMICO algorithm and we report the main steps of its detection procedure. Moreover, we describe both how the quantities associated with each detected cluster are estimated and how their errors are computed, because we exploit this information to study the clustering properties of this catalogue.

In particular, in Section 5.4, we present the mass-observable scaling relations constructed in Bellagamba et al. (2019) and employed to assign a mass to each detected cluster. We focus on this point because one of the main goals in this Thesis is to present a different method to estimate the mass-richness scaling relation through the clustering measurements, instead of the lensing estimation exploited in Bellagamba et al. (2019).

Finally, we delineate the main characteristics of the AMICO-KiDS catalogue, underlining the quantities that we exploit for our analysis.

### 5.1 The KiDS survey

The Kilo-Degree Survey (KiDS) is a 1500 square degree optical photometric survey that exploited the OmegaCAM wide-field imager on the VLT Survey Telescope (VST) with four broad-band filters ( $u, g, r, i$ ). The scientific purpose of KiDS is to map the large-scale matter distribution in the Universe, exploiting weak lensing and photometric redshift measurements. This aim requires depth images with high quality. The VST-OmegaCAM has a resolution of 0.21 arcsec/pixel. The current KiDS catalogue is composed of about 100,000 sources per square degree, for a total of almost 150 million sources over the full survey area. The KiDS catalogue provides the coordinates, the 2 arcsec aperture photometry in the four bands and the photometric redshift for all the detected galaxies down to the  $5\sigma$  magnitude limits of 24.3, 25.1, 24.9 and 23.8 in the four filters.

The photometric redshift of the galaxies has been obtained with three different techniques: two of these are Machine-Learning techniques while the other method exploits a Bayesian photo- $z$  estimator based on a template-fitting method, the so-called BPZ method; see Bilicki et al. (2018) for a complete explanation of these techniques.

The AMICO algorithm was been used to look for galaxy clusters in the KiDS Data Release 3 (KiDS-DR3, presented in de Jong et al. (2017)). This survey covers a total area of 438 deg<sup>2</sup>, but avoiding the regions of the sky affected by satellite tracks and haloes produced by bright stars and regions with accentuated distortions, the effective area is of 377 deg<sup>2</sup>. The final AMICO-KiDS galaxy cluster catalogue contains 7988 candidate galaxy clusters down to  $S/N > 3.5$  up to redshift  $\sim 0.8$ .

In the following Sections, we explain how the detection procedure of AMICO works for detecting galaxy clusters in the KiDS-DR3.

## 5.2 The AMICO detection algorithm

AMICO, which stands for Adaptive Matched Identifier of Clustered Objects, is an algorithm for the detection of galaxy clusters in photometric surveys, based on the *Optimal Filtering Technique* (for a detailed discussion on the *Optimal Filtering Technique* technique see i.e. Maturi, M. et al., 2005, Bellagamba et al., 2011). Specifically, AMICO adopts an iterative approach for the extraction of cluster candidates from the observed galaxy distribution with the aim of maximising the signal to noise ratio ( $S/N$ ) of the clusters, utilising the statistical properties of both field galaxies and member galaxies, which are described by an arbitrary number of physical quantities. A detailed description of AMICO can be found in Maturi et al. (2019). In the next Sections, a brief overview on this algorithm is given.

### 5.2.1 Linear optimal matched filtering

AMICO is built on the *linear optimal matched filter method*, so the data are modelled as the superimposition of the signal and noise as:

$$d(\vec{x}) = s(\vec{x}) + n(\vec{x}), \quad (5.1)$$

where  $d(\vec{x})$  represents the data,  $s(\vec{x})$  is the signal we want to extract and  $n(\vec{x})$  is the *background noise*, respectively. The two last quantities represent the galaxy clusters signal and the contamination given by the field galaxies in AMICO, respectively.

Despite the fact that AMICO can work on an arbitrary number of galaxy properties for building the AMICO-KiDS cluster catalogue from KiDS-DR3 data, in Bellagamba et al. (2018), the galaxies are simply represented as data points, labelled with  $i$ , characterised by sky coordinates  $\theta_i$ , a band magnitudes  $m_i$  and a photometric redshift distribution  $p(\vec{z})$ , so each galaxy is defined as  $\vec{x}_i = (\vec{\theta}_i, m_i, p_i(\vec{z}))$ .

The galaxy cluster signal is defined as  $s(\vec{x}) = A c(\vec{x})$ , where  $A$  is the signal amplitude estimated by the convolution between the data and the *filter*, a kernel derived by a constrained minimisation procedure. This convolution returns an unbiased and with minimum variance estimation of  $A$ , which is defined on a three-dimensional grid  $(\vec{\theta}_c, z_c)$ , with resolution of  $0.3'$  across the sky and 0.01 in redshift, and it is discretised to deal with counts of galaxies:

$$A(\vec{\theta}_c, z_c) = \alpha^{-1}(z_c) \sum_{i=1}^{N_{gal}} \frac{C(z_c; \vec{\theta}_i - \vec{\theta}_c, m_i) p_i(z_c)}{N(m_i, z_c)} - B(z_c), \quad (5.2)$$

where  $N$  and  $C$  describe the properties of the distribution of field and member galaxies at redshift  $z_c$ , respectively (as discussed in Section 5.2.2);  $\alpha$  holds the filter normalisation;  $B$  is a background subtraction term that measures the average contribution of the field galaxies over the total signal amplitude, defined as  $B(z_c) = \alpha^{-1}(z_c) \beta(z_c)$ , where  $\beta(z_c)$  is the total number of galaxies in the cluster model at redshift  $z_c$ , ensuring that  $A = 0$  if the galaxy distribution around a given position corresponds to the field one.

The expected root mean square (r.m.s.) of the amplitude is:

$$\sigma_A(\vec{\theta}_c, z_c) = \alpha^{-1}(z_c) + A(\vec{\theta}_c, z_c) \frac{\gamma(z_c)}{\alpha(z_c)^2}, \quad (5.3)$$

where the first term on the right side is given by the background stochastic fluctuations and the second term derives from the Poissonian fluctuations caused by the actual member galaxies present in the data as measured with the filter (an exhaustive description of  $B$  term is given in Bellagamba et al., 2018). The factors  $B$ ,  $\alpha$ , and  $\gamma$  are properties of the filter, and only depend on the cluster and field galaxy models (their definitions is provided in Section 5.2.2 and they are extensively discussed in Maturi et al., 2019).

Once the amplitude  $A$  is computed for all angular and redshift positions, the first cluster candidate is then selected considering the (Gaussian) likelihood (see Appendix A for the definition of the likelihood), defined as:

$$\mathcal{L}(\vec{\theta}_c, z_c) = \mathcal{L}_0 + A^2(\vec{\theta}_c, z_c) \alpha(z_c) \quad (5.4)$$

$$\Delta\mathcal{L}(\vec{\theta}_c, z_c) = A^2(\vec{\theta}_c, z_c) \alpha(z_c), \quad (5.5)$$

where  $\mathcal{L}_0$  is a constant that does not depend on the position. Hence, maximo of  $A$  are also maximo of the likelihood. However, for their quadratic relation, the likelihood does not distinguish between overdensities ( $A > 0$ ) and underdensities ( $A < 0$ ). Hence, to identify the clusters it is also necessary to take into account the S/N, defined as  $A/\sigma_A$ . As we previously mentioned, the aim is to maximise the S/N, that is meaningful only when  $A$  is positive. Therefore, on the 3D grid in which we have defined  $A$ , the position  $(\vec{\theta}_c, z_c)$  characterised both by large S/N values and large likelihood is selected. Therefore, the first cluster candidate is identified as the location with the largest (Gaussian) likelihood and S/N.

Once the cluster is detected, the algorithm computes the probability of all galaxies in the identified region to be members of that cluster. This probability is defined as follows:

$$P_i(j) = P_{f,i} \times \frac{A_j C_j(\vec{\theta}_i - \vec{\theta}_c, m_i) p_i(z_c)}{A_j C(\vec{\theta}_i - \vec{\theta}_c, m_i) p_i(z_c) + N(M_i, z_j)} \quad (5.6)$$

where  $P_{f,i} \equiv 1 - \sum_j P_i(j)$  is the probability of the  $i$ -th galaxy to belong to the field, that is equal to 1 for all the galaxies at the beginning of the process, and then decreases while the galaxies are progressively attributed to detected clusters, marked by  $j$ . When a galaxy is attributed to the detected cluster, that galaxy is removed by AMICO from the amplitude map before looking for a new cluster candidate, re-computing the likelihood and variance on the map. This process, called *cleaning*, leads to:

$$A_{new}(\vec{\theta}_j, z_k) = A(\vec{\theta}_j, z_k) - \sum_{i=1}^{N_{gal}} \frac{C_j(\vec{\theta}_i - \vec{\theta}_c, m_i) p(z_k)}{N(m_i, z_k)}. \quad (5.7)$$

The *cleaning* is an iterative process that stops when a chosen minimum S/N is reached, defined as  $S/N = A/\sigma_A$ . Through the subtractions of the identified cluster in each step, the minimum S/N can be reached, so it is possible to identify also objects characterised by smaller amplitude.

### 5.2.2 Models for member galaxies and field galaxies

The cluster model,  $C(z_c; r, m)$  characterises the expected distribution of galaxies. At redshift  $z_c$ ,  $C(z_c; r, m)$  is a function of the distance of the  $i$ -th galaxy from the cluster centre, defined as  $r = |\vec{\theta}_i - \vec{\theta}_c|$ , and of the band magnitude  $m$ . The cluster model is built on a luminosity function  $\Phi(m)$  and a radial profile  $\Psi(r)$ , as:

$$C(r, m) = \Phi(m) \Psi(r), \quad (5.8)$$

where an implicit  $z_c$  redshift dependence is assumed. The parameters for  $\Phi(m)$  and  $\Psi(r)$  are taken from Hennig et al. (2017), in which a cluster sample detected in the Dark Energy Survey (DES) is analysed. The detection for this sample is based on the tSZ effect, that prevents any selection bias linked to the optical properties of the galaxies in clusters. This cluster sample covers a redshift range similar to the one analysed in Maturi et al. (2018). The luminosity function  $\Phi(m)$  assumed is the Schechter function (Schechter (1976)), expressed as:

$$\Phi(m) = 10^{-0.4(m-m_*)(\beta+1)} \exp\left[-10^{-0.4(m-m_*)}\right], \quad (5.9)$$

where  $\beta \approx -1$  is assumed, as in Hennig et al. (2017) and  $m_*$  is the typical magnitude at the considered redshift.

The radial profile  $\Psi(r)$  is described as:

$$\Psi(r) = \frac{C_0}{\frac{r}{r_s} \left(1 + \frac{r}{r_s}\right)^2}, \quad (5.10)$$

that is the NFW profile (Navarro et al. (1997)), in which  $C_0$  is the normalisation parameter and the scale radius  $r_s$  depends on the *concentration parameter*  $c$ , assumed as  $c = 3.59$ , because  $r_s \equiv R_{200}/c_{200}$ , where  $R_{200}$  corresponds to a mass  $M_{200} = 10^{14}M_{\odot}/h$ . Inside  $R_{200}$  and below  $m_* + 2$ , the total number of galaxies is  $N_{200}$ , which is coherent with Hennig et al. (2017), where  $N_{200} = 22.9$  for  $M_{200} = 10^{14}M_{\odot}/h$ .

### 5.2.3 Mass proxies in AMICO

As we explained in Section 5.2.1, AMICO computes the amplitude  $A$ , expressed as Eq.(5.7), which can be used as a mass proxy. Moreover, other photometric quantities are estimated by AMICO during the selection procedure, expressed as a function of the probabilistic membership association of galaxies Eq.(5.6), that could also be used as mass proxies.

In particular, one of the mass proxies derived by AMICO is the *apparent richness*, defined as the sum of the probabilities of all galaxies associated to the  $j$ -th detection, thus representing the number of visible galaxies belonging to a detected cluster:

$$\lambda_j = \sum_{i=1}^{N_{gal}} P_i(j). \quad (5.11)$$

The convenience of this quantity compared to the amplitude  $A$  is that it is connected to a direct observable, that is the number of visible galaxies. This quantity depends on the redshift because the number of visible members decreases with cosmic distance.

AMICO calculates also the *intrinsic richness*, defined by summing over the galaxies brighter than  $m_* + 1.5$  and within the virial radius  $R_{200}$ :

$$\lambda_{*,j} = \sum_{i=1}^{N_{gal}} P_i(j) \quad \text{with} \quad \begin{cases} m_i < m_*(z_j) + 1.5 \\ r_i(j) < R_{200}(z_j). \end{cases} \quad (5.12)$$

The radial truncation  $R_{200}$  and  $m_*$  are free parameters of the model used for the construction of the filter that are adopted for internal consistency. Clearly, each detection has its own  $R_{200}$ ;  $\lambda_*$  is an almost redshift independent quantity which can better characterise the cluster masses.

## 5.3 The KiDS-AMICO cluster catalogue

The catalogue presented in Maturi et al. (2018), obtained as described in Section 5.2, lists for each detected cluster its identification number, sky coordinates (Right Ascension R.A., Declination Dec), redshift, amplitude  $A$  (Eq.(5.2)), intrinsic richness  $\lambda_*$  (Eq.(5.12)), apparent richness  $\lambda$  (Eq.(5.11)), S/N, likelihood  $\mathcal{L}$  (Eq.(5.4)) and the masked fraction in which the cluster is detected. Moreover, the  $1\text{-}\sigma$  error is given for  $A$ ,  $\lambda$  and  $\lambda_*$  and also for the coordinates, (RA, Dec,  $z$ ). The  $A$  error is defined as Eq.(5.3), while, for  $\lambda$  and  $\lambda_*$ , the error is estimated by running the AMICO code on mock catalogues. The mock catalogues used for this purpose are built on the real data of KiDS-DR3 by a Monte Carlo extraction of both the member galaxies and the field ones, based on their probabilistic association to the detected clusters sample, defined in Eq.(5.6), and to the probability of the  $i$ -th galaxy to belong to the field, defined as

$$P_{f,i} \equiv 1 - \sum_j P_i(j). \quad (5.13)$$

Therefore, the resulting mock cluster catalogues are a random realisation based on the overall statistical properties of all original detections. Therefore, the mock catalogues fully preserve the statistical characteristic of the original data catalogue by construction. The uncertainties on the properties of the detections are evaluated by running on the mock catalogues the AMICO code

and comparing the measured values with the expected ones. In this way, is associated the  $1-\sigma$  error for each quantity estimated by the AMICO code.

The R.A. and Dec errors are estimated as the uncertainties over the maps produced by AMICO in defining the cluster centre. The scatter along the R.A. and Dec increase at lower redshift because of their larger angular extension which makes more difficult to identify the centre of the structure. While, at  $z > 0.45$ , the angular resolution is defined by the pixel size chosen for the maps produced by AMICO, that is  $\sim 0.3$  arcmin.

Comparing the AMICO results to other surveys constructed with different techniques, the redshifts estimated by AMICO are tested. With these tests, a bias of  $\sim 0.02$  emerged. Therefore, the corrected redshift is defined as  $z_{cor} = z - 0.02(1+z)$ , where  $z$  is the redshift estimated by the algorithm. The effect of this correction is shown in Fig.(5.1), in which the comparison between the redshift distributions for both the values is shown. As can be seen in Fig.5.1, in the redshift distribution ( $z$ ) there is a hole at  $z \sim 0.38$  given by the shape of the  $g$  and  $r$  filters, resulting in a not optimal covering of the 4000 Å break at that redshift (Padmanabhan et al., 2005)). Thanks to these comparisons it has been also estimated the accuracy as  $\sigma_z \sim 0.02(1+z)$ , where  $z$  is the redshift estimated by AMICO.

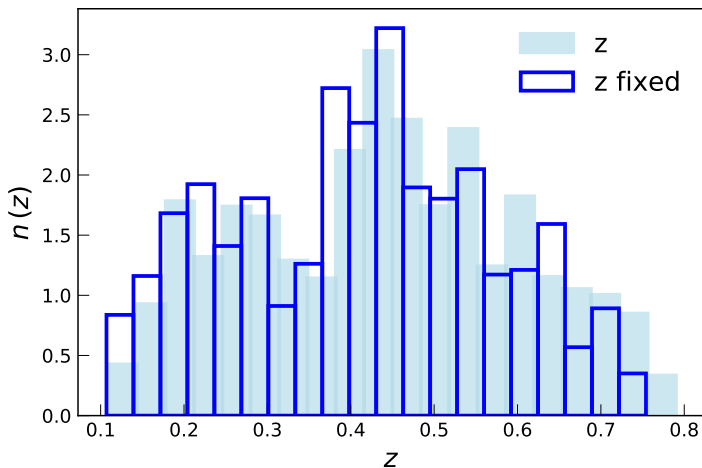


**Figure 5.1:** The redshift distribution in the AMICO-KiDS cluster catalogue, comparing the estimated redshifts (pale blue histogram) to the distribution of the corrected redshifts (blue histogram). For both these redshift distributions the interval  $0.1 - 0.8$  is considered.

## 5.4 Mass-observable relation

To exploit optically-detected galaxy clusters in astrophysics and cosmology, it is necessary to estimate their masses. In Bellagamba et al. (2019) the mass for the clusters detected by AMICO at redshifts between 0.1 and 0.6 are estimated with weak gravitational lensing. Indeed, weak gravitational lensing depends on the total matter density because the light is deflected when encounters the matter presents along the line of sight. The deflection of light leads both to the amplification and to the distortion of galaxy shapes. With stacked lensing, the galaxy-mass cross-correlation can be measured. Therefore, to estimate weak lensing masses, KiDS shear data are used, performing a stacked weak lensing analysis for groups of clusters selected according to their redshift and amplitude. The relation between the weak lensing masses ( $M_{200}$ ) and the photometric observable obtained thanks to the selection procedure of the AMICO algorithm, is modelled as:

$$\log \frac{M_{200}}{10^{14} M_{\odot}/h} = \alpha + \beta \log \frac{O}{O_{piv}} + \gamma \frac{E(z)}{E(z_{piv})}, \quad (5.14)$$

where  $E(z) = H(z)/H_0$  and  $O_{piv}$  represent typical values of the considered observable and  $z_{piv}$  is the typical redshift of the total sample. The redshift evolution of the relation is accounted by the factor  $\gamma E(z)$  (as done in Sereno et al., 2015a). The mass in the AMICO-KiDS catalogue are

expressed as  $M_{200}$ , that is the virial mass (Eq.3.7) defined as

$$M_{200} = \frac{4}{3}\pi R_{200}^3 \Delta_c \rho_c$$

with  $\Delta_c = 200$ .

The parameters  $\alpha$ ,  $\beta$  and  $\gamma$  of the mass-observable relation are obtained with a Bayesian analysis (see Appendix A) in which the priors are uniform with ranges given by  $-1 < \alpha < 1$ ,  $0.1 < \beta < 5$  and  $-5 < \gamma < 5$ . The cluster sample is divided in three redshift intervals:  $0.1 \leq z < 0.3$ ,  $0.3 \leq z < 0.45$ ,  $0.45 \leq z < 0.6$ . Then, each bin is subdivided in amplitude, creating 5, 5 and 4 sub-intervals to compute the mass-amplitude relation, in which  $A_{piv} = 2$ . The results are:

- $\alpha = 0.114 \pm 0.038$
- $\beta = 1.99 \pm 0.10$
- $\gamma = 0.73 \pm 0.63$

The same approach is followed to determine the mass-richness relation, in which  $\lambda_{piv}^* = 30$ . This time, the best-fit parameters are:

- $\alpha = 0.004 \pm 0.038$
- $\beta = 1.71 \pm 0.08$
- $\gamma = -1.33 \pm 0.64$

Therefore, in the AMICO-KiDS cluster catalogue, for each object we also have the mass inferred both by richness and amplitude. The defined relation is also extended to the redshift range between 0.6 and 0.8 in which the data from weak lensing are not sufficiently robust to perform a Bayesian analysis.

## 5.5 Main properties of our sample

In our work, we analyse the clustering characteristics of the AMICO-KiDS cluster catalogue characterised by 7988 objects. Selecting the clusters in the range  $0.1 \leq z \leq 0.8$ , the objects become 7936 and their distribution in redshift and intrinsic richness is shown in Fig.5.1-5.3, respectively. The characteristic redshift is  $z_m = 0.412$  and the peculiar  $\lambda_*$  is 24.8.

In the next Chapter, we will present our work based on the AMICO-KiDS catalogue. To study the clustering proprieties of this sample, many of the given quantities are used: the coordinates (R.A., Dec,  $z$ ) are necessary both to compute the distance among the pairs in the catalogue and also to construct the random catalogue; the redshift and the masses are exploited to compute the effective bias; the mean photo- $z$  error,  $\sigma_z$ , is considered for defining the Gaussian damping term in the assumed theoretical model for the 2PCF in the redshift-space (discussed in Section 4.5.2). The photo- $z$  error distribution is shown in Fig.5.2 and its mean values is 0.026.

In particular, for our work, the fixed redshifts are used, defined in Section 5.3 and illustrated in Fig.5.1.

The masses given in the AMICO-KiDS catalogue are obtained by the scaling relations discussed in the Section above, both from the amplitude and from the intrinsic richness. We decide to work using the masses obtained by exploiting the scaling relation between the mass and the richness, illustrated in Fig.5.3, after testing that the effective bias estimated with these different quantities are compatible within the errors. Therefore, for now on, we refer with the term mass, to the mass obtained by the scaling relation using the  $\lambda_*$  as the mass-proxy. The minimum mass in the catalogue is  $0.017 M_\odot/h$ , while, the highest mass is  $13.279 M_\odot/h$ .

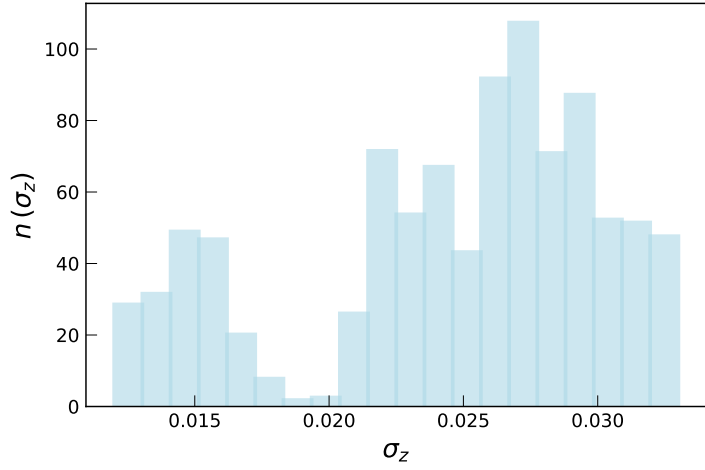


**Figure 5.2:** The photo-z error distribution in the AMICO-KiDS cluster catalogue in the interval  $0.1 - 0.8$  is considered.

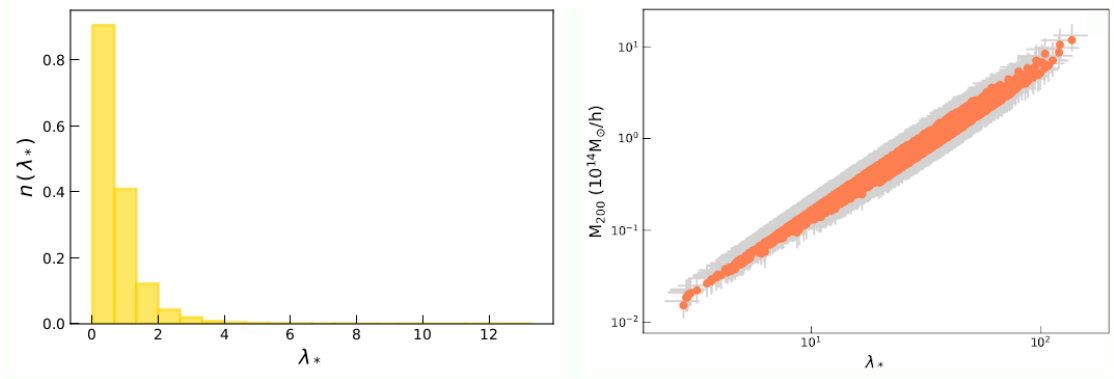


**Figure 5.3:** *Left panel:* the intrinsic richness distribution in AMICO-KiDS cluster catalogue in the redshift range  $0.1 < z < 0.8$ ; *Right panel:* the intrinsic richness and the mass of clusters in AMICO-KiDS catalogue in the redshift range  $0.1 < z < 0.8$ , (in grey the  $1-\sigma$  estimated for  $M_{200}$  and  $\lambda_*$ ).

# Chapter 6

## Results

In this Chapter, we present the clustering proprieties of the photometric sample of 7936 clusters selected from the KiDS-DR3 by the AMICO algorithm (as explained in Chapter 5).

The Chapter is divided as follows:

- in Section ??, we present the CosmoBolognaLib exploiting in our work to perform the analysis presented in this Chapter.
- In Section 6.2, we show the 2PCF measurements in redshift space, comparing our estimates to the theoretical expectations for the correlation function in the  $\Lambda$ CDM model (discussed in Section 4.5.2). Moreover, the effective bias (defined in Section 4.6) is estimated for the entire catalogue and for different sub-catalogues, with the aim to show how its value increases both with the redshift and the mass, as expected in the  $\Lambda$ CDM scenario;
- in Section 6.3, we estimate the correlation length scale  $r_0$  and the slope  $\gamma$ , defined in Section 4.5.1. Also for this analysis we work on the entire catalogue as well as in sub-catalogues selected in redshift and mass to verify if the correlation scale rises with the redshift and in mass, as expected;
- in Section 6.4, we perform a Bayesian statistical Markov chain Monte Carlo (MCMC) analysis to identify the best-fit values for the mean redshift error,  $\sigma_z$ , and for the effective bias of the entire catalogue and of the same sub-catalogues studied in the previous Sections. Carrying out this statistical analysis, we obtain the effective bias with a different approach than the one used in Section 6.2. The two results are completely consistent. In this analysis, a fiducial cosmology is assumed with all the cosmological parameters set as constant;
- in Section 6.5, we conduct the same examination as in Section 6.4, but without setting all the cosmological parameters as constant values. With this approach, we constrain at the same time the bias, the mean  $\sigma_z$  errors and some cosmological parameters. At first we assume as free cosmological parameters the pairs  $\sigma_8$  and  $\Omega_M$ , computing their derived parameter  $S_8$ . Then, also  $w_0$  is let as a free parameter in the statistical analysis;
- in Section 6.6, we investigate the scaling relation between the intrinsic richness,  $\lambda_*$ , and the mass of the clusters. To constrain the normalisation  $\alpha$ , the slope  $\beta$  and the scatter parameter  $\gamma$ , in Eq.(5.14), we exploit our clustering measurements, linking the bias to the scaling relation in our Bayesian analysis.

To summarise, in this Thesis work, we measure for the first time the 2PCF of the AMICO-KiDS catalogue, both in redshift space and in real space. Moreover, the bias of the sample is computed with different techniques, and the estimated value are all consistent (with an effective bias value for the entire catalogue equal to  $2.60 \pm 0.01$ ).

Then, some cosmological parameters ( $\sigma_8$ ,  $\Omega_M$ ,  $S_8$ ,  $w_0$ ) are constrained. The measurements presented in this Thesis are in accordance with the  $\Lambda$ CDM scenario, presented in Section 1.5.

Moreover, we propose a new method to compute the scaling relation between the intrinsic richness and the mass of cluster exploiting the clustering signal, obtaining  $\alpha = 0.036 \pm 0.0534$ ,

$\beta = 1.88 \pm 0.48$  and  $\gamma = -1.32 \pm 0.48$ , perfectly consistent with the results found in Bellagamba et al. (2018) using the lensing data.

In conclusion, this work demonstrates the possibility to exploit the 2PCF of a photometric cluster catalogue for cosmological applications, such as to constrain cosmological parameters and to study the evolution both of the bias and the correlation length scale in redshift and mass. Moreover, it is also possible to constrain the normalisation, slope and scatter of the cluster scaling relation which links photometric observables to the cluster masses.

## 6.1 The CosmoBolognaLib

The CosmoBolognaLib is a free libraries of software C++/Python implemented to investigate the LLS of the Universe. The CBL offers the necessary tools to carry out statistical analyses, to handle with catalogues of extragalactic source and to constrain cosmological parameters. In particular, the CBL provide highly optimised algorithms to measure the 2PCF. One of the main focuses of the CBL is to provide functions to measure and model the clustering properties of astronomical sources. The CBL provide also methods both to construct random catalogues and to manage an external catalogue.

Therefore, in our work, we utilise the CBL to construct the random catalogue and to manage the AMICO-KiDS catalogue (necessary to define the 2PCF as discuss in the following Section), to estimate the effective bias  $b_{eff}$  exploiting the Tinker et al. (2010) model function (as discussed in Section 4.24 and we will use this definition for all our work), to compute the theoretical model presented in this Chapter and also to perform all the Bayesian statistical analysis illustrated in the following Sections. Moreover, with this Thesis, we implement new likelihood modules that were not present in the CBL to constrain both the scaling relation which links the cluster masses to the photometric observables as well as to estimate cosmological parameters assuming a model for the 2PCF that takes into account the main photo- $z$  errors of the photometric catalogue.

These new function will be added to forthcoming version of the CBL.

## 6.2 Redshift-space 2PCF

In this Section, we analyse the redshift-space 2PCF of the AMICO-KiDS cluster catalogue, a photometric sample of 7936 clusters in the range  $0.1 < z < 0.8$ , selected by the AMICO algorithm from the KiDS-DR3 survey. The clusters in the catalogue have mean redshift  $z_m = 0.412$ , while the mean mass is  $M_{200} = 0.774 \cdot 10^{14} M_{\odot}/h$ .

We measure the 2PCF in redshift space with the CBL software (presented in Marulli et al., 2016). specifically, we estimate the 2PCF exploiting the LS estimator, defined in Eq.(4.6). As discussed in Section 4.2.1, choosing this estimator has many advantages. Indeed, it has been demonstrated that the LS estimator provides an unbiased measure of the 2PCF (in the limit  $N_R \rightarrow \infty$ ), with minimum variance. The errors on the measurements can be assumed to be Poissonian, as first approximation.

To measure the 2PCF, as defined in Section 4.2, a random sample has to be provided. The random sample is a catalogue of randomly distributed points having the same three-dimensional coverage of the data. Our random catalogue is generated by shuffling the observed coordinates (R.A., Dec,  $z$ ). Namely, it is attributed to the clusters of the random sample the coordinates (R.A., Dec,  $z$ ) randomly extracted from the AMICO-KiDS catalogue. Therefore, the random sample has the same 3D distribution of the real sample. The random catalogue generated is 30 times larger than the AMICO sample to limit shot noise effects, as mentioned in Section 4.2.1.

To measure the 2PCF of our catalogue, we have to convert observed coordinates into comoving ones and, for this operation, a fiducial cosmology has to be assumed, as noted in Section 4.3. In our work we assume the  $\Lambda$ CDM model, presented in Section 1.5, with cosmological parameters from either Planck 2018 results (Planck18, Aghanim et al., 2018b) and WMAP 9-year results (WMAP9, Hinshaw et al., 2013), as we will specify.

The 2PCF of the AMICO-KiDS catalogue is estimated in the range  $5 \text{ Mpc } h^{-1} < s < 80 \text{ Mpc } h^{-1}$ . At larger scales the signal is weak and dominated by the errors, while at smaller scales the clustering signal is negligible because of cluster sizes that set the minimum cluster separation.

The theoretical model for the 2PCF in the  $\Lambda$ CDM is obtained by Fourier transforming the redshift-space cluster power spectrum of computed with the CBL using CAMB, at the mean redshift of the catalogue, as described in Section 4.6.1. As discussed in Section 4.6, to compare our measurements to the theoretical model, the cluster bias has to be included. The 2PCF model for the tracers distribution, is defined as:

$$\xi_{clu}(s) = b_{eff}^2 \xi_{DM}(s) \quad (6.1)$$

where  $\xi_{DM}(s)$  is computed by Fourier transforming the DM power spectrum, presented in Chapter 2, while  $b_{eff}$  is the effective bias defined in Section 4.6.

For each cluster of the AMICO-KiDS catalogue both the mass and the redshift are known, as explained in Chapter 5. Therefore, it is possible to estimate the effective bias, defined in Eq.(4.24), assuming the Tinker et al. (2010) model function (defined in Eq.(4.25)), as discussed in Section 4.6.1.

Working on a photometric sample, our measurements must be compared to a theoretical model that takes into account the photo- $z$  errors in the data. In Section 4.5.2, we discuss how to consider the photo- $z$  uncertainties in the power spectrum by introducing a Gaussian damping term  $\sigma$ , specified in Eq.(4.18). The Gaussian damping factor  $\sigma$  is computed assuming the  $H(z)$  measured in the fiducial cosmology and taking as  $\sigma_z$  the mean redshift error of the catalogue, that is  $\sigma_z = 0.026$ . In Fig.6.1, we compare our 2PCF measurements in redshift space (black points) to the expected model (blue line). If the theoretical model is computed without considering the damping factor, our measurements are completely inconsistent with the theoretical model (grey line). The assumed bias is the value obtained with the Tinker et al. (2010) model function, that is  $2.60 \pm 0.01$ , for Planck18.

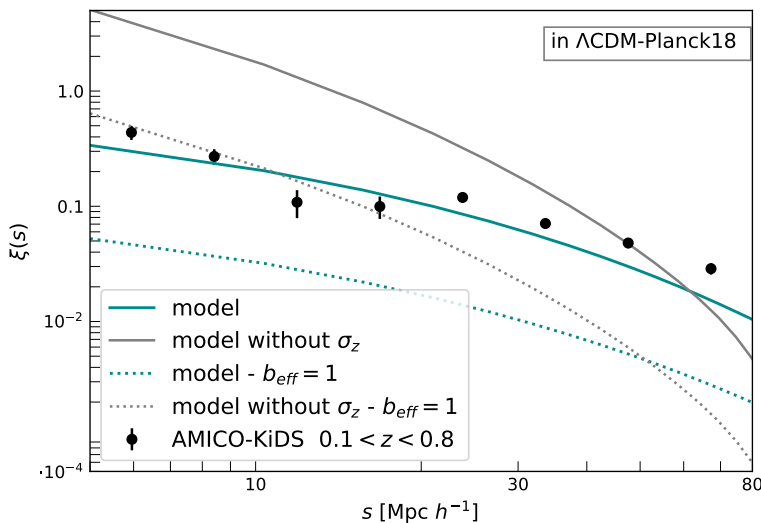


**Figure 6.1:** Redshift-space 2PCF of the AMICO-KiDS clusters in  $0.1 < z < 0.8$  (black dots, with Poissonian errors), in the range  $5.0 \text{ Mpc } h^{-1} < s < 80.0 \text{ Mpc } h^{-1}$ , compared to the *standard* theoretical model (grey solid line) and the theoretical model in which the photo- $z$  error is included with the Gaussian damping factor  $\sigma$  (blue solid line). The fiducial cosmology is the  $\Lambda$ CDM with Planck18 parameters. The *standard* model and the *damped* one for the DM (i.e. with  $b = 1$ ), are also shown (blue and grey dotted lines, respectively).

The result is obtained with assuming the  $\Lambda$ CDM with Planck18 parameters. We repeated the same procedure assuming WMAP9 parameters finding consistent results within the errors.

From Fig.6.1 it is clear that:

1. the bias factor has to be considered when the clusters are used as tracers to study the clustering in the LSS, as discussed in Section 4.6;
2. as expected it is necessary to take into account the photo-z errors, as we explained in Section 4.5.2;

### 6.2.1 Evolution of bias

We study the evolution over time of the 2PCF in the range  $5.0 \text{ Mpc } h^{-1} < s < 80.0 \text{ Mpc } h^{-1}$ , analysing the signal in different redshift bins. Fig.6.2 shows our measurements compared to the *damped* model. This latter is computed with the mean redshift and the mean photo-z error in each different redshift range. These models are also multiplied for the effective bias,  $b_{eff}^2$ , estimated by assuming the Tinker et al. (2010) model function. For these ranges, both the main characteristics of our clusters and the estimated bias are reported in Table 6.1. We consider also the catalogue divided in two redshift ranges, for which the main characteristics are reported in Table 6.2.

**Table 6.1:** The number of clusters ( $N_{cluster}$ ), the mean redshift ( $z_m$ ) and its mean error ( $\sigma_z$ ), and the effective bias computed with Tinker et al. (2010) model function assuming both Planck18 and WMAP9 in the different ranges in  $z$ :  $0.1 < z < 0.25$ ,  $0.25 < z < 0.45$ ,  $0.45 < z < 0.8$ .

	$N_{cluster}$	$z_m$	$\sigma_z$	bias - Planck18	bias - WMAP9
$0.1 < z < 0.25$	1537	0.186	0.019	$1.67 \pm 0.013$	$1.72 \pm 0.014$
$0.25 < z < 0.45$	3059	0.382	0.022	$2.30 \pm 0.013$	$2.37 \pm 0.014$
$0.45 < z < 0.8$	3125	0.558	0.029	$3.27 \pm 0.017$	$3.06 \pm 0.014$

**Table 6.2:** The number of clusters ( $N_{cluster}$ ), the mean redshift ( $z_m$ ) and its mean error ( $\sigma_z$ ), and the effective bias computed with Tinker et al. (2010) model function assuming both Planck18 and WMAP9 in the different ranges in  $z$ :  $0.1 < z < 0.3$  and  $0.35 < z < 0.8$ .

	$N_{cluster}$	$z_m$	$\sigma_z$	bias - Planck18	bias - WMAP9
$0.1 < z < 0.3$	2265	0.215	0.022	$1.78 \pm 0.012$	$1.83 \pm 0.012$
$0.35 < z < 0.8$	5332	0.502	0.025	$2.93 \pm 0.013$	$3.06 \pm 0.014$

**Table 6.3:** The number of clusters ( $N_{cluster}$ ), the mean redshift ( $z_m$ ) and its mean error ( $\sigma_z$ ), and the effective bias computed with Tinker et al. (2010) model function assuming both Planck18 and WMAP9 in the different ranges in mass:  $M_{200} < 0.77 \cdot 10^{14} M_{\odot}/h$  and  $M_{200} > 0.77 \cdot 10^{14} M_{\odot}/h$

	$N_{cluster}$	$z_m$	$\sigma_z$	bias - Planck18	bias - WMAP9
$M_{200} < 0.77 \cdot 10^{14} M_{\odot}/h$	5201	0.367	0.019	$2.02 \pm 0.0067$	$2.08 \pm 0.068$
$M_{200} > 0.77 \cdot 10^{14} M_{\odot}/h$	2735	0.488	0.024	$3.61 \pm 0.018$	$3.69 \pm 0.018$

Figure 6.2 shows how the effective bias of our samples increases with the redshift, as expected from the theory, discussed in Section 4.6.

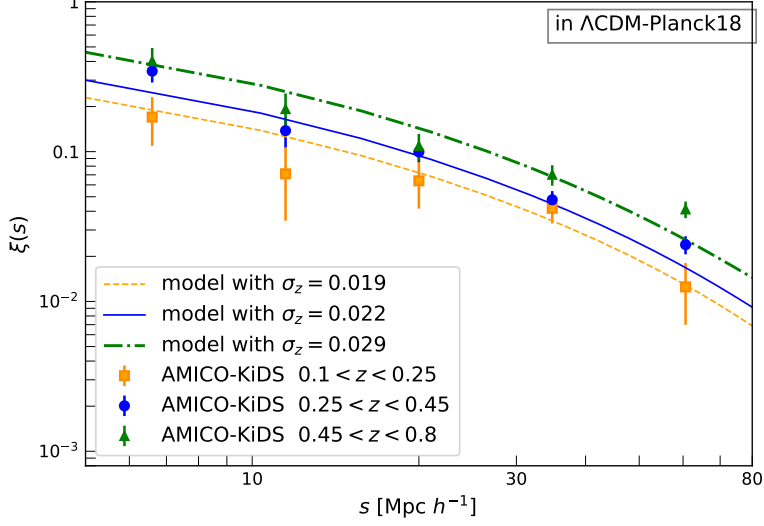


**Figure 6.2:** Redshift-space 2PCF of the AMICO-KiDS clusters in the range  $5.0 \text{ Mpc } h^{-1} < s < 80.0 \text{ Mpc } h^{-1}$ , for three different ranges in redshift:  $0.1 < z < 0.25$  (orange squares);  $0.25 < z < 0.45$  (blue dots);  $0.45 < z < 0.80$  (green triangles). The measured 2PCF in each bin is compared to the *damped* model (the orange dashed line, the blue solid line and the green dot-dashed line, respectively). The *damped* model is computed assuming  $\Lambda\text{CDM}$  with Planck18 parameters. The bias is estimated for each bin assuming the Tinker et al. (2010) model function.

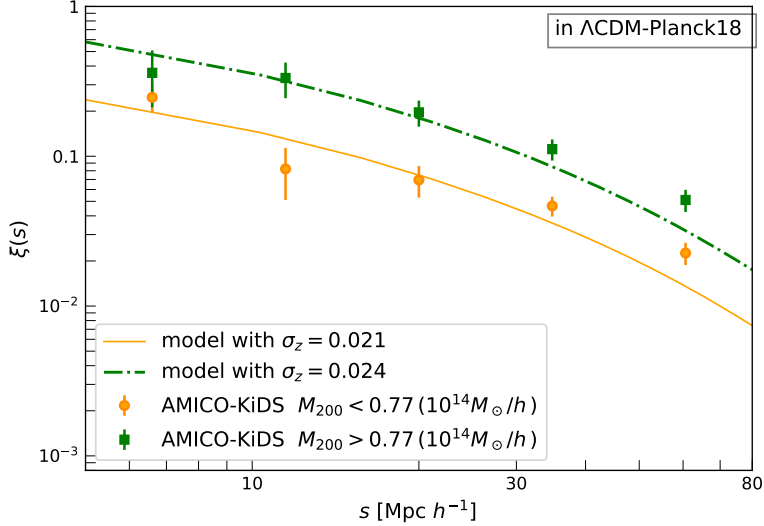


**Figure 6.3:** Redshift-space 2PCF of the AMICO clusters in the range  $5.0 \text{ Mpc } h^{-1} < s < 80.0 \text{ Mpc } h^{-1}$ , for two different ranges in mass:  $M_{200} < 0.77 \cdot 10^{14} M_{\odot}/h$  (orange dots) and  $M_{200} > 0.77 \cdot 10^{14} M_{\odot}/h$  (green squares). The measured 2PCF in each bin is compared to the *damped* model (the orange line and the dot-dashed green line, respectively). The effective bias is computed assuming the Tinker et al. (2010) model function. It is assumed the  $\Lambda\text{CDM}$  cosmology characterised by Planck18 parameters.

From the theory we also expect that the bias increases with the mass. To study the evolution in the mass of the bias, we measure the 2PCF of our catalogue in different mass ranges. Unfortunately, it was not possible to estimate the clustering signal in more than two mass intervals without being dominated by the errors. The 2PCF measurements in two mass intervals are shown in Fig.6.3. The fundamental parameters for these ranges are reported in Table 6.3.

Moreover, we divide the two sub-catalogues in mass in two  $z$  intervals: a *low-mass* catalogue (characterised by masses lower than  $0.77 \cdot 10^{14} M_{\odot}/h$ ) and a *high-mass* catalogue (characterised by masses higher than  $0.77 \cdot 10^{14} M_{\odot}/h$ ). With this analysis, we see how the bias increases with both  $z$  and mass.

Fig.6.4 shows that the highest signal is associated with the highest values of redshift and masses, while the lowest signal is associated with the lowest values in redshift and masses, as expected. We report the main proprieties of these sub-catalogues in Table 6.4.

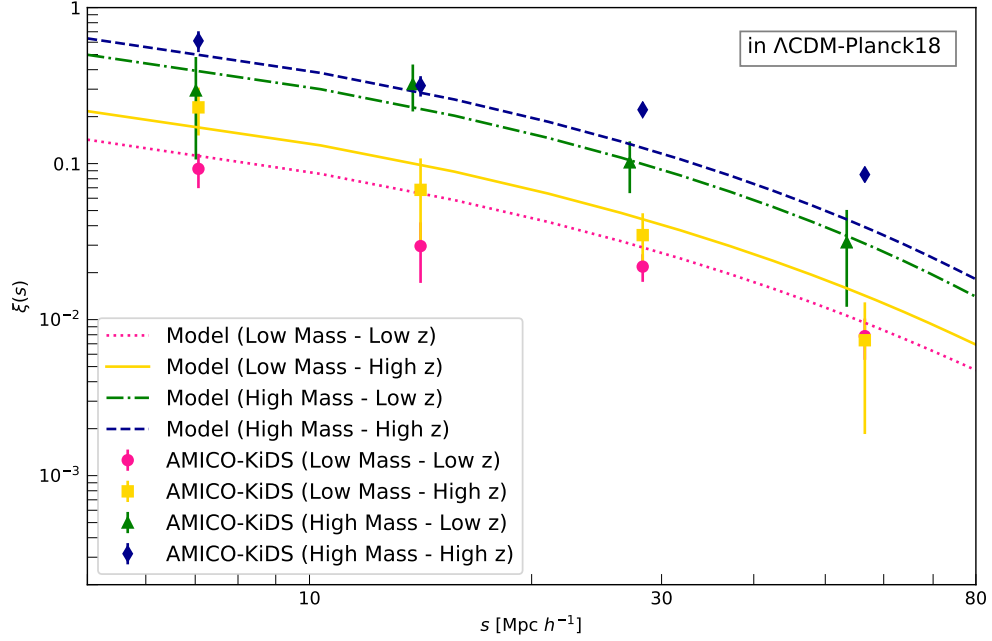


**Figure 6.4:** Redshift-space 2PCF of the AMICO-KiDS clusters in  $5.0 \text{ Mpc } h^{-1} < s < 80.0 \text{ Mpc } h^{-1}$ , divided in two sub-catalogues in mass: a low-mass sub-catalogue with  $M_{200} < 0.77 \cdot 10^{14} M_{\odot}/h$  and a high-mass sub-catalogue with  $M_{200} > 0.77 \cdot 10^{14} M_{\odot}/h$ . These sub-catalogues are selected in two different ranges in redshift:  $0.1 < z < 0.3$  and  $0.35 < z < 0.8$ . For each interval, the measurements are compared to the theoretical model with the Tinker et al. (2010) model function ( $1.60 \pm 0.02$ ,  $2.09 \pm 0.02$ ,  $2.67 \pm 0.03$ ,  $3.51 \pm 0.02$ , respectively). The theoretical models are represent with the pink dotted-line, the yellow solid line, the green dot-dashed line and with the blue dashed line, respectively. It is assumed the  $\Lambda$ CDM cosmology with Planck18 parameters.

**Table 6.4:** The number of clusters ( $N_{cluster}$ ), the redshift interval, the mean mass, the mean redshift ( $z_m$ ) and its mean error ( $\sigma_z$ ), and the effective bias computed with Tinker et al. (2010) model function assuming both Planck18 and WMAP9 for the sub-catalogues in mass in different range in redshift. The reported masses  $M_{200}$  are given in  $10^{14} M_{\odot}/h$ .

	$N_{cluster}$	$z$ interval	mean $M_{200}$	$z_m$	$\sigma_z$	bias - Planck18	bias - WMAP9
$M_{200} < 0.77$	1725	$0.1 < z < 0.3$	0.29	0.22	0.019	$1.60 \pm 0.02$	$1.62 \pm 0.007$
$M_{200} < 0.77$	2411	$0.3 < z < 0.8$	0.39	0.45	0.022	$2.09 \pm 0.02$	$2.13 \pm 0.02$
$M_{200} > 0.77$	537	$0.1 < z < 0.3$	1.19	0.25	0.024	$2.67 \pm 0.03$	$2.77 \pm 0.02$
$M_{200} > 0.77$	2815	$0.3 < z < 0.8$	1.31	0.53	0.027	$3.51 \pm 0.02$	$3.58 \pm 0.02$

### 6.3 The real-space 2PCF

In this Section, we present the 2PCF in real space. This function is exploited to estimate the correlation scale length,  $r_0$ , and the slope,  $\gamma$ , of the AMICO-KiDS catalogue, defined in Section 4.5.

The estimation of the correlation scale has been one of the main aims in clustering studies since the first works on galaxies surveys. The correlation scale appears as a function of galaxy properties (such as luminosity, morphological or spectral type, color and stellar mass), as we discuss in Section 6.3. The observations show that  $r_0$  increases with time and mass. It has long been known that clusters of galaxies are much more strongly clustered than galaxies (see Kaiser, 1984). Indeed, rare objects, such as clusters, show greater clustering because they can only form at the highest peaks of the DM density field. The clusters' correlation scale  $r_0$  depends on both the richness and the redshift, increasing with these two quantities.

As explained in Chapter 4, our data in redshift space are affected by geometrical and dynamical distortions as well as photo-z errors, which impact on the shape of the 2PCF. In order to assess the correlation function signals in real space, we have to subtract these distortions' effect or to take them into account. The predominant effect on our data, as discussed in Section 4.5.2, is given by photo-z errors. Hence, in redshift space, we exploit a theoretical *damped* model that includes these distortions, as done in the above Section. However, it is also possible to remove the distortions by interacting at the *2D 2PCF* up to sufficiently large scales along the line of sight, as explained in Section 4.5.1.

We derive the real-space clustering by computing  $\xi(r_p, \pi)$ , defined in Eq.(4.10), with  $r_p$  between  $5.0 \text{ Mpc } h^{-1}$  and  $75.0 \text{ Mpc } h^{-1}$ , while  $\pi$  is considered between  $0. \text{ Mpc } h^{-1}$  and  $50.0 \text{ Mpc } h^{-1}$ .

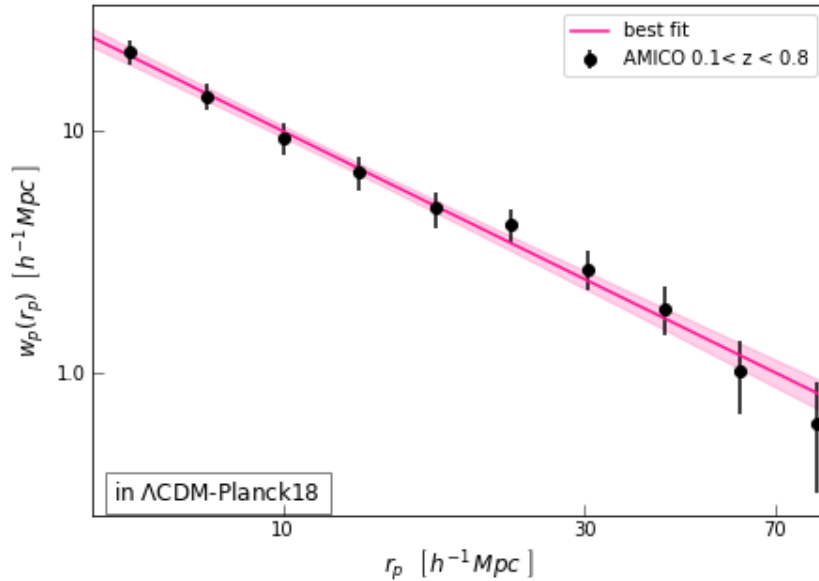


**Figure 6.5:** The projected 2PCF  $w_p(r_p)$  of AMICO-KiDS (black dots) in the redshift range  $0.1 < z < 0.8$ , from  $5.0 \text{ Mpc } h^{-1}$  to  $75.0 \text{ Mpc } h^{-1}$  compared to the best-fit power law model (pink line, the shadow represents the 68% of confidence).

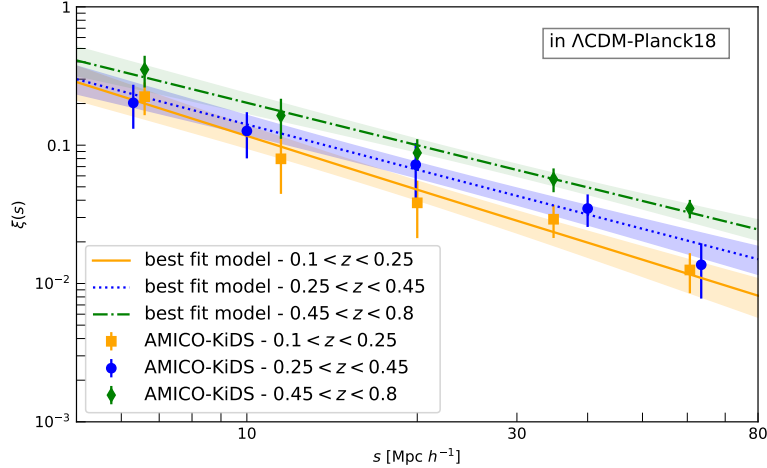


**Figure 6.6:** The best-fit models, obtained by fitting  $w_p(r_p)$  correlation function of the AMICO clusters in the three different ranges in redshift:  $0.1 < z < 0.25$  (with the orange line is illustrated the best fit, the data are represented by the orange squares, the orange shadow region represents the 68% of confidence),  $0.25 < z < 0.45$  (with the blue dotted line is illustrated the best fit, the data are represented by the blue dots, the blue shadow region represent the 68% of confidence),  $0.45 < z < 0.80$  (with the green dot-dashed line is illustrated the best fit, the data are represented by the green diamonds, the green shadow region represent the 68% of confidence).

Then, we compute the integral along the line of sight, as explained in Section 4.5.1, obtaining the projected correlation function,  $w_p(r_p)$ , which is illustrated for the entire catalogue in Fig.6.5. We compute  $w_p(r_p)$  also for the redshift three ranges described in Table 6.1, as shown in Fig.6.6.

The projected correlation function is modelled with a function having a power-law form (Eq.4.16), as illustrated in Fig.6.5, in order to define the correlation scale  $r_0$  and the slope  $\gamma$ . This analysis is also done in the five redshift intervals (described in Tables 6.2- 6.1) and in the two ranges in mass (presented in Tables 6.3). To perform this analysis, a fiducial cosmology is assumed. We show the results for Planck18. Assuming WMAP9 we found consistent results within the  $1 - \sigma$  errors.

With the power-law fitting, we estimate the correlation scale,  $r_0$ , and the slope,  $\gamma$  for each bin. These results are illustrated in Fig.6.7.

Our data show an increment of the scale correlation in the redshift and in mass, as expected from the theory because more massive clusters at higher redshift are more clustered objects, as confirmed also in the precedent Section. In contrast, the clustering slope,  $\gamma$ , appears quite constant in the different ranges of mass and redshift.

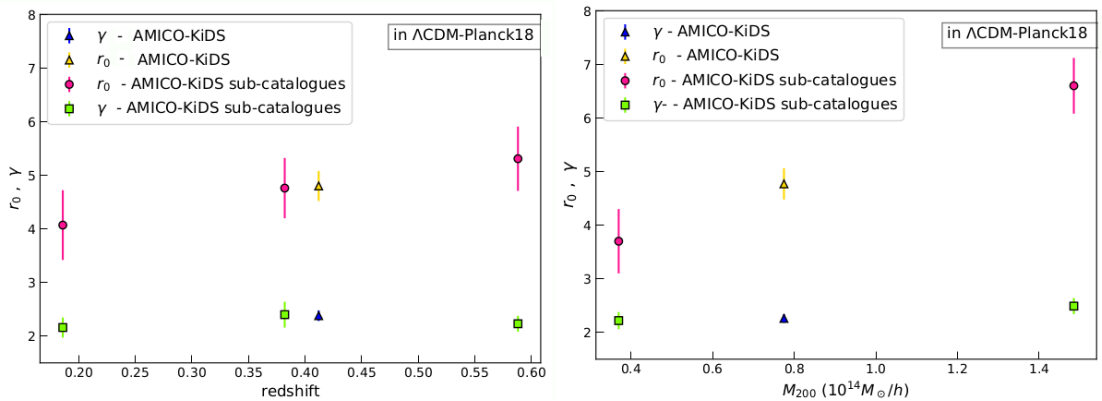


**Figure 6.7:** The correlation scale  $r_0$ , computed in sub-ranges and for the entire catalogue (represented by pink dots and the yellow triangles respectively; the error bars represent the  $1 - \sigma$  errors) and the slope  $\gamma$ , estimated in sub-ranges and for the entire catalogue (represent by green squares the blue triangles, respectively; the error bars represent the 68% of confidence), both in function of the redshift and of the mass. *Left panel:* the correlation scale  $r_0$  and the slope  $\gamma$  computed in three redshift ranges (described in Table 6.1) and for the entire catalogue. *Right panel:* the correlation scale  $r_0$  and the slope  $\gamma$  in two mass ranges (defined in Table 6.2) and for the entire catalogue.

## 6.4 Constraints on the bias and the mean photo-z errors

In Section 6.2, the 2PCF measurements in redshift space were compared to the theoretical model with the Gaussian damping factor. As noted, this theoretical model depends on bias,  $\sigma_z$  and cosmological parameters. In Section 6.2, to compute this model, we assumed the bias estimated exploiting the Tinker et al. (2010) model function, the value of  $\sigma_z$  measured as in the AMICO-KiDS catalogue (see Chapter 5) and a fiducial cosmology.

In this Section we still assume a fiducial cosmology (either Planck18 or WMAP9), while the bias and the mean photo-z error are estimated by a Bayesian statistical Markov chain Monte Carlo (MCMC) analysis (see Appendix A) of the 2PCF by sampling the posterior distribution of  $b_{eff}$  and  $\sigma_z$ , for which we assume flat priors in the range  $[1., 5.]$  and  $[0.01, 0.1]$ .

This statistical analysis is performed to identify the pair  $b_{eff}-\sigma_z$  capable to fit our model and to compare our previous results with the value obtained with this procedure. Actually, the parameters  $b_{eff}-\sigma_z$  are partially degenerate, as shown in Fig.6.8. The expected 2PCF increases with the bias values, while decreases with the increasing of the photo-z errors.

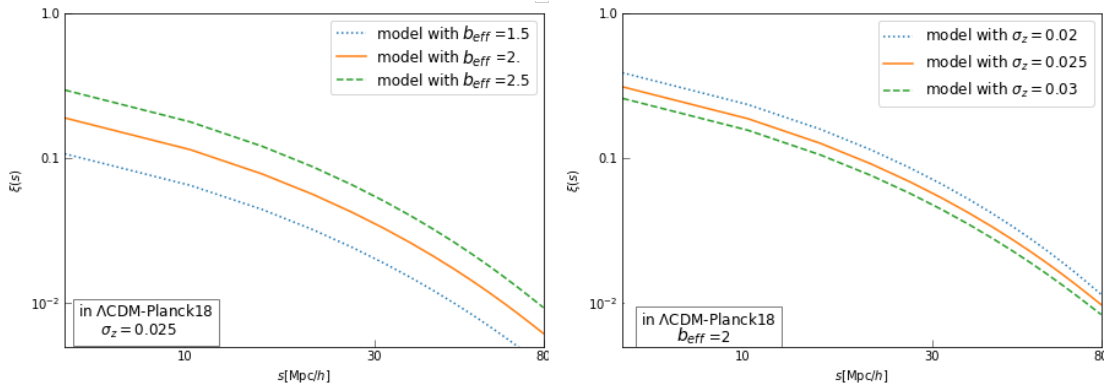


**Figure 6.8:** The 2PCF theoretical model in the range between  $5.0 \text{ Mpc h}^{-1}$  to  $80.0 \text{ Mpc h}^{-1}$  for the mean redshift of the catalogue, measured assuming the Planck18 cosmology. *Left panel:* are shown three different theoretical models for the 2PCF assuming the same photo-z error (equals to 0.025) but different bias. The highest theoretical curve is obtained with  $b_{eff} = 2.5$  (dashed green line); with  $b_{eff} = 1.5$  the lowest theoretical curve is obtained (blue dotted line); the middle curve is given by  $b_{eff} = 2.0$  (orange line). *Right-panel:* for the same  $b_{eff}$  (equals to 2.0) are illustrated three different theoretical curves: the highest photo-z error gives the lowest theoretical curve ( $\sigma_z = 0.03$ , green dashed line); the highest  $\sigma_z$  error is associated with the highest theoretical curve ( $\sigma_z = 0.02$  blue dotted line); the middle curve is given by  $\sigma_z = 0.025$  (the orange line).

For this Bayesian analysis, a standard Gaussian likelihood is considered, defined as:

$$\mathcal{L}_{CL} \propto \exp(-\chi_{CL}^2/2) \quad (6.2)$$

$$\chi_{CL}^2 = \sum_{i=0}^N \sum_{j=0}^N (\xi_i^d - \xi_i^m) C_{i,j}^{-1} (\xi_j^d - \xi_j^m), \quad (6.3)$$

where  $N$  is the number of comoving separation bins in which the 2PCF is computed,  $d$  and  $m$  indicates *data* and *model* respectively, and  $C_{i,j}^{-1}$  is the inverse of the *covariance matrix* estimated from the data. The covariance matrix measures the variance and the correlation between the different bins of the 2PCF. To define the likelihood, it is necessary to compute the covariance matrix, which is calculated once the random catalogue is constructed. Indeed the *covariance matrix*  $C_{i,j}$  is defined as follows:

$$C_{i,j} = \mathcal{N} \sum_{k=1}^{N_R} (\xi_i^k - \bar{\xi}_i) (\xi_j^k - \bar{\xi}_j). \quad (6.4)$$

In Eq.(6.4) the subscripts  $i$  and  $j$  run over the 2PCF bins, while  $k$  refers to the 2PCF of the  $k$ -th of the  $N_R$  random catalogue realisations.  $\mathcal{N}$  is the normalisation factor in which is considered the possibility that the  $N_R$  realisations may not be independent (see Norberg et al., 2009).

However, this method is very computational expensive, since a large set of mocks have to be created and analysed. Alternatively, different statistical techniques can be exploited, that still provide a fairly robust estimation of the covariance matrix. In this work, the estimated Poisson errors are used to set the diagonal elements of  $C_{i,j}$ , while the other terms are neglected.

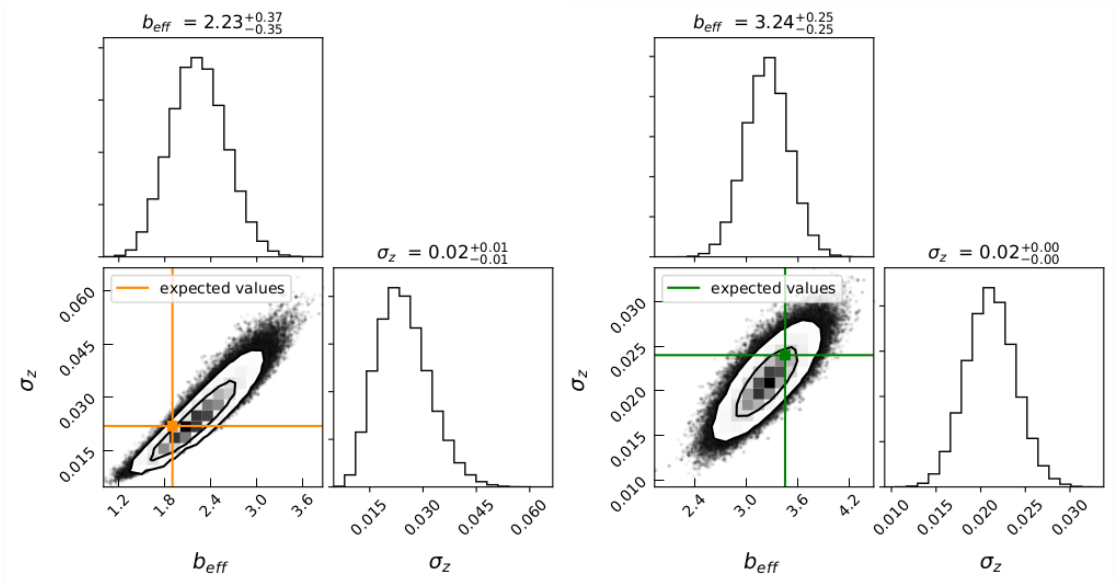


**Figure 6.9:** The posterior distribution and the 68% – 95% confidence contours for bias and  $\sigma_z$  in two different ranges in mass. *Left panel:*  $M_{200} < 0.77 \cdot 10^{14} M_{\odot}/h$ ; *Right oanel:*  $M_{200} > 0.77 \cdot 10^{14} M_{\odot}/h$ . The expected values reported in figure are the effective bias computed with Tinker, assuming the same fiducial cosmology and the mean photo-z, computed for each considered bin (represented with orange lines and green lines for the two bins respectively and defined in Table 6.3).

This analysis is done for the five ranges in redshift (presented in Tables 6.1-6.2) and two bins in mass (described in Table 6.3) as well as for the entire catalogue. The 68% – 95% confidence contours provided by the MCMC are shown in Figs.6.9-6.10 for the three bins in redshift and the two bins in mass. Moreover, we also computed the best-fit model for these ranges. Both the 68% – 95% confidence contours and the best-fit model for the two ranges in redshift are shown in Fig.6.11. With our data it is possible to break the degeneracy between the effective bias and  $\sigma_z$  for each sub-catalogue.

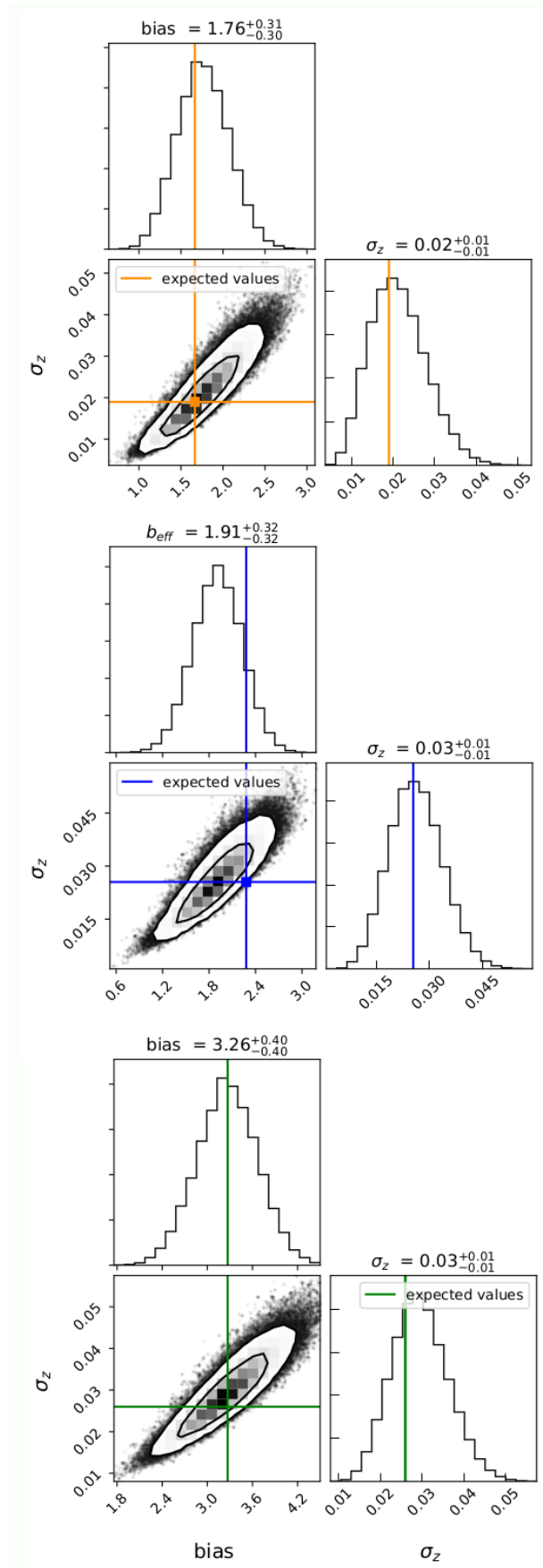


**Figure 6.10:** The posterior distribution for bias and  $\sigma_z$  and the 68% – 95% confidence contours for these two free parameters, in three different ranges in redshift. The expected values for bias and the mean photo- $z$  error are reported in Table 6.1. *Upper panel:* results for the redshift range  $0.1 < z < 0.25$  with the expected values for this bin indicated with the orange lines. *Central panel:* results for the redshift range  $0.25 < z < 0.45$ , with the expected values for this bin indicated with the blue lines. *Last panel:* the range  $0.45 < z < 0.8$ , with the expected values reported with the green lines.

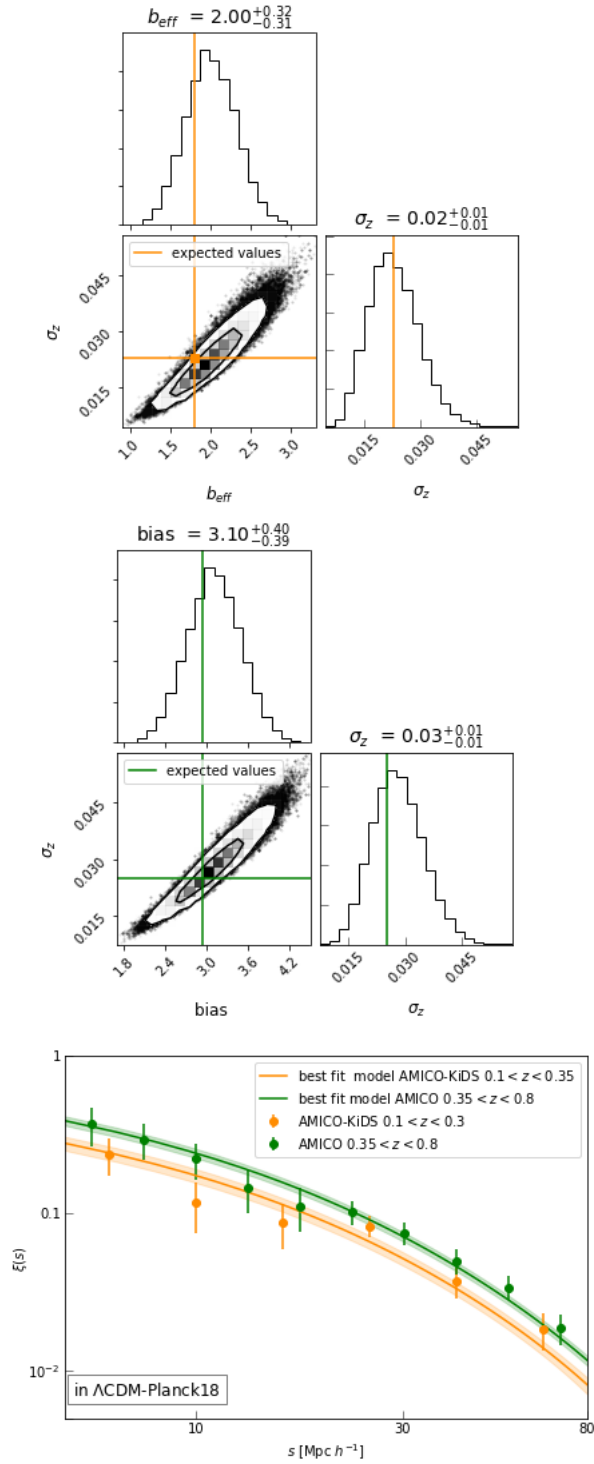


**Figure 6.11:** *Upper panel:* the posterior distribution and the 68% – 95% confidence contours for  $b_{eff}$  and  $\sigma_z$  in the redshift range  $0.1 < z < 0.3$  with the expected values (in orange) assumed as the Tinker et al. (2010) model function and the average photo- $z$  in the considered redshift bin. *Central panel:* the 68% – 95% confidence contours for  $b_{eff}$  and  $\sigma_z$  in the redshift range  $0.35 < z < 0.8$  with the expected values (in green) given by the Tinker et al. (2010) bias and the average photo- $z$  in the considered redshift bin. *Last panel:* the best-fit model for these two intervals. The orange line is the best-fit for the range  $0.1 < z < 0.3$ , the shadow region represents the 68% of confidence, the data are reported with orange dots; the green line represents the best-fit model for the interval  $0.35 < z < 0.8$ , with the shadow region that represents the 68% of confidence, while the data are reported with the green dots.

In Fig.6.12 we compare the bias computed directly with the Tinker et al. (2010) model function with the best-fit values obtained by performing the MCMC statistical analysis. As we can see, the values obtained with these two different approaches are consistent within the errors.

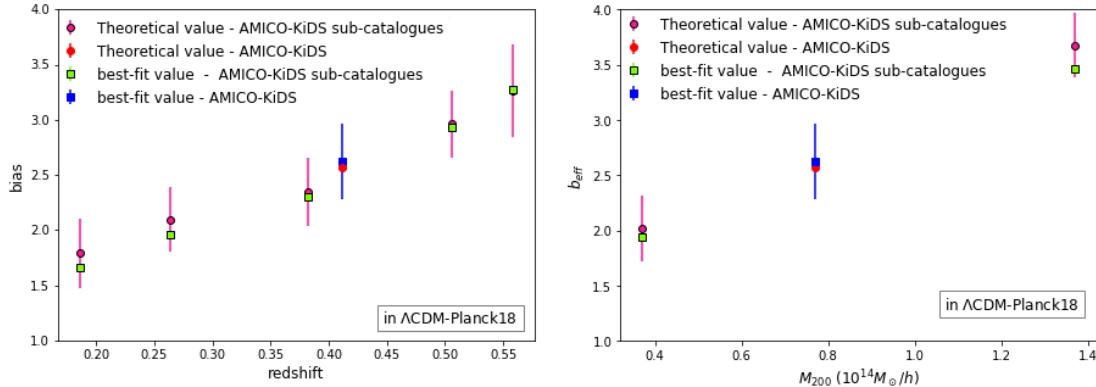


**Figure 6.12:** *Left panel:* the bias obtained with Tinker in the different ranges in redshift (green square) with the analytical error, compared to the bias estimated by the statistical analysis in the same bin with the 68% confidence. *Right panel:* the bias obtained with Tinker in the different ranges in mass (green square) with the analytical error, compared to the bias estimated by the statistical analysis in the same bin with the 68% confidence.

As expected from the theory (discussed in Section 4.6), also with this statistical approach we find that the bias increases both with mass and redshift.

## 6.5 Cosmological parameters

This Section is dedicated to the statistical analysis of our data for estimating cosmological parameters. With this statistical analysis, we investigate the constraints given by galaxy clusters clustering measurements to both cosmological parameters and galaxy cluster bias.

The 2PCF of galaxy clusters can be exploited to constrain the main cosmological parameters (Sereno et al., 2015b, Marulli et al., 2018). As explained in Chapter 4, the 2PCF is defined as the Fourier transform of the power spectrum and it is sensitive to the underlying cosmology, as discussed in Chapter 2. In particular, the 2PCF is sensitive to both the amplitude parameter,  $\sigma_8$ , and  $\Omega_M$  (as explained in Sections 2.4.1 and 2.4.3, respectively). Moreover, as seen in Fig.6.1, the theoretical model computed by the Fourier transform of the DM power spectrum ( $\xi_{DM}(s)$ ) has to be multiplied, as first approximation, to the square of the effective bias of the tracers. Therefore, it is possible to constrain both the cosmological parameters and the bias from our the 2PCF measurements.

There is a partial degeneracy among  $\sigma_8$ ,  $\Omega_M$  and the effective bias: as it is shown in Fig.6.13, the expected theoretical values for the 2PCF increases both with the minimum mass and  $\sigma_8$ , while it decreases with the increasing of  $\Omega_M$ . The increasing of  $\Omega_M$  is reflected in lower bias values, instead, if  $\sigma_8$  value rises, the bias rises too. Moreover, as we have discussed in Section 6.2, lower masses correspond to lower estimated values for the bias.

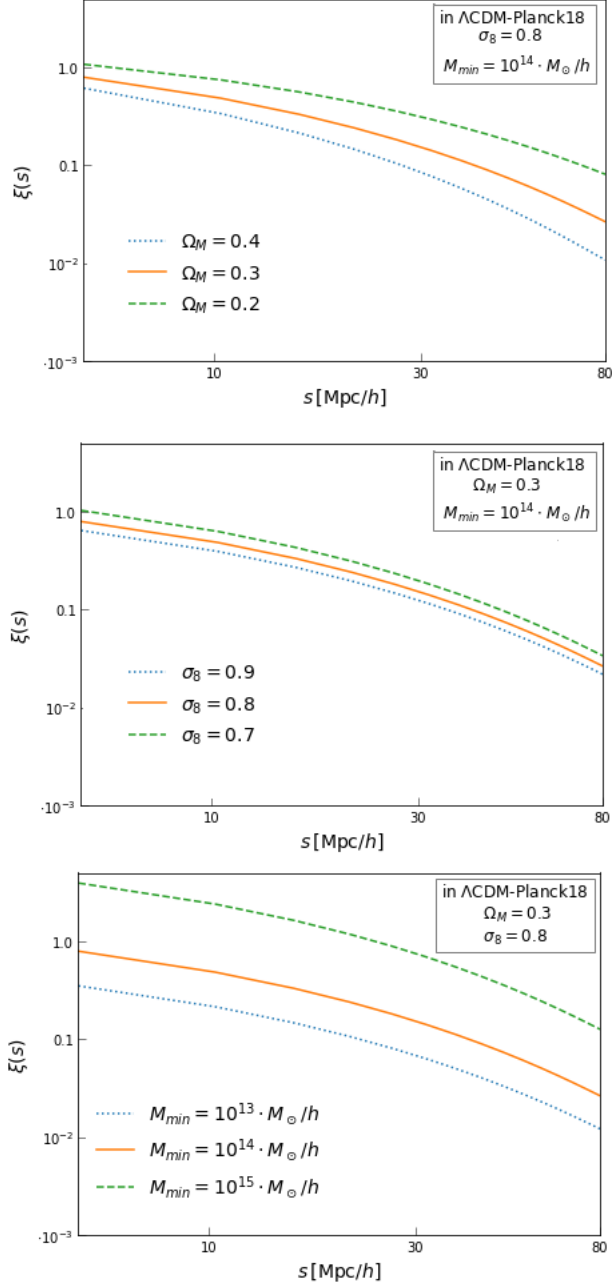


**Figure 6.13:** The 2PCF damped theoretical model in  $z$ -space for  $\sigma_z = 0.026$  in the range between  $5.0 \text{ Mpc h}^{-1}$  to  $80.0 \text{ Mpc h}^{-1}$  at the mean redshift of the AMICO-KiDS catalogue, measured assuming the Planck18 cosmology in three different cases. *Upper panel:* fixing  $\sigma_8 = 0.8$  and the minimum mass of the sample as  $M_{min} = 10^{14} M_{\odot}/h$ , three different values for  $\Omega_M$  are considered: 0.4 (dotted blue line), 0.3 (orange solid line) and 0.2 (dot-dashed green line); the corresponding  $b_{eff}$ , estimated with Tinker et al. (2010), are  $3.94 \pm 0.02$ ,  $4.20 \pm 0.02$  and  $4.44 \pm 0.02$ . *Second panel:* assuming the Planck18 cosmology, fixing  $\Omega_M = 0.3$  and the minimum mass of the sample as  $M_{min} = 10^{14} M_{\odot}/h$ , three different values for  $\sigma_8$  are assumed: 0.9 (dotted blue line), 0.8 (orange solid line) and 0.7 (dot-dashed green line); the corresponding bias are  $3.35 \pm 0.02$ ,  $4.20 \pm 0.02$  and  $5.47 \pm 0.03$ . *Third panel:* assuming the Planck18 cosmology, fixing  $\sigma_8 = 0.8$  and  $\Omega_M = 0.3$ ,  $M_{min}$  values considered are  $M_{min} > 10^{13} M_{\odot}/h$  (dotted blue line),  $M_{min} > 10^{14} M_{\odot}/h$  (orange solid line) and  $M > 10^{15} M_{\odot}/h$  (dot-dashed green line); the corresponding effective bias are  $3.35 \pm 0.02$ ,  $4.20 \pm 0.02$  and  $5.47 \pm 0.03$ .

We perform a Bayesian statistical MCMC analysis in the two mentioned ranges in  $z$  and in mass (Tables 6.2-6.1), assuming as fiducial cosmology either Planck18 or WMAP9, which predict different theoretical curves for the  $\xi(s)$ , as shown in Fig.6.14.

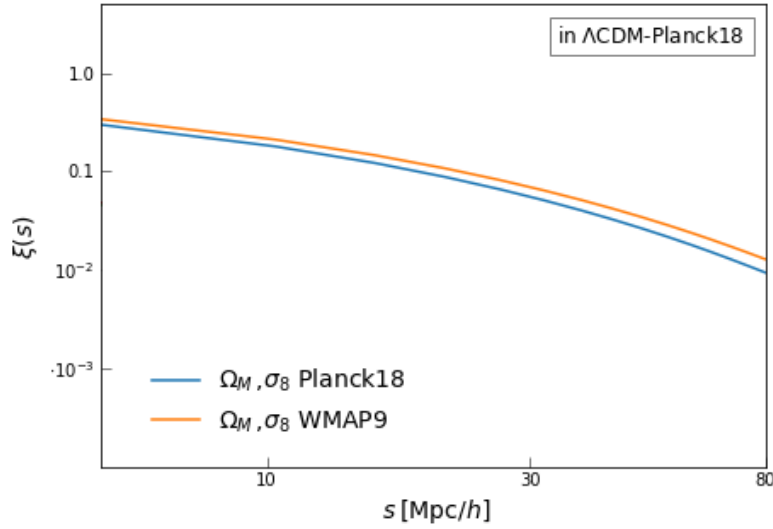


**Figure 6.14:** The  $\xi(s)$  damped theoretical model for  $\sigma_z = 0.025$  computed from  $5.0 \text{ Mpc h}^{-1}$  to  $80.0 \text{ Mpc h}^{-1}$ , in the AMICO-KiDS redshift range ( $0.1 < z < 0.8$ ) and in its mass range ( $0.017 M_\odot/h < M_{200} < 13.279 M_\odot/h$ ). In *orange* is assumed  $\Omega_M = 0.288$  and  $\sigma_8 = 0.817$  as obtained in WMAP9, while in *blue* it is shown the  $\xi(s)$  from Planck18, so  $\Omega_M = 0.301$  and  $\sigma_8 = 0.810$ .

Specifically, firstly we constrain  $\sigma_8$  and  $\Omega_M$ , estimating  $S_8$  as a derived parameter, defined as:

$$S_8 = \sigma_8 \sqrt{\Omega_M/0.3}, \quad (6.5)$$

which describes the growth of cosmic structure.

Then, we also analysis  $w_0$  (defined in 1.4.2), that in the first analysis is assumed equal to  $-1$ . The value of  $w_0$  impacts the growing rate of the structures. Hence, also between this cosmological parameters and the previously mentioned one there is pariyal degeneracy. In Fig.6.15 it is shown how the theoretical model for  $\xi(s)$  depends on the choice of the  $w_0$  value.

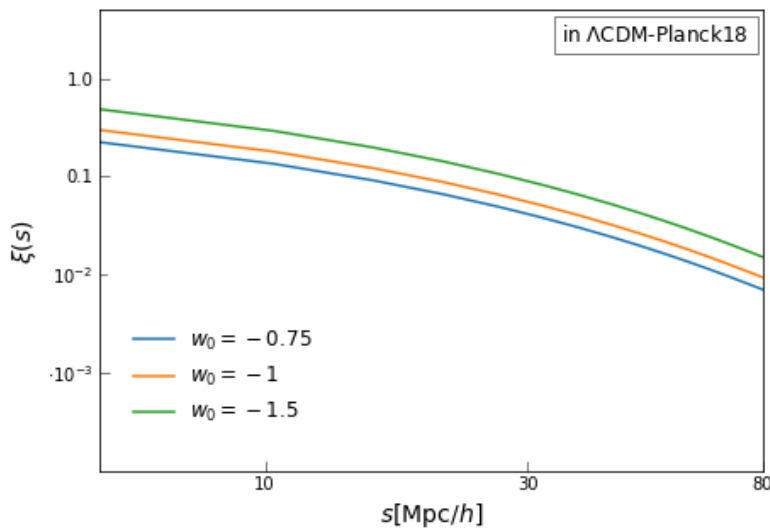


**Figure 6.15:** The  $\xi(s)$  damped theoretical model for  $\sigma_z = 0.025$  computed from  $5.0 \text{ Mpc h}^{-1}$  to  $80.0 \text{ Mpc h}^{-1}$ , in the AMICO-KiDS redshift range  $0.1 < z < 0.8$ , and in its mass range ( $0.017 M_\odot/h < M_{200} < 13.279 M_\odot/h$ ), computed assuming as fiducial cosmological model Planck18 with different values for  $w_0$ :  $-0.75$ ,  $-1$ ,  $-1.5$ . With the decreasing of  $w_0$ , the expected 2PCF signal increase.

All the cosmological constraints presented in this Section, are obtained by carrying out a Bayesian statistical MCMC analysis to sample the posterior. A standard Gaussian likelihood is assumed defined in Eq.(6.2), as done in Section 6.4.

For the Bayesian statistical analysis, at first, we assume, flat priors for  $\sigma_8$  and  $\Omega_M$ , while, for the effective bias and  $\sigma_z$  we consider Gaussian priors with mean at the results of our previous analysis and with standard deviation equal to 1. and 0.01, respectively. This choice is motivated by the attempt to break the degeneracy among the four parameters, being strongly related. In any case, the adopted priors are large enough as the resulting posterior distribution (reported in Fig.6.16) are much narrower than the prior distributions.

This analysis is done only for two ranges in  $z$  and two ranges in mass (Tables 6.2-6.3), where the 2PCF signal is good enough. For each range, we obtain the posterior distribution and the 68% – 95% confidence contours for our free parameters ( $\sigma_z$ ,  $b_{eff}$ ,  $\sigma_8$  and  $\Omega_M$ ) and also for the derived parameter ( $S_8$ ). Fig.6.16 shows the results for the redshift bin  $0.35 < z < 0.8$ .

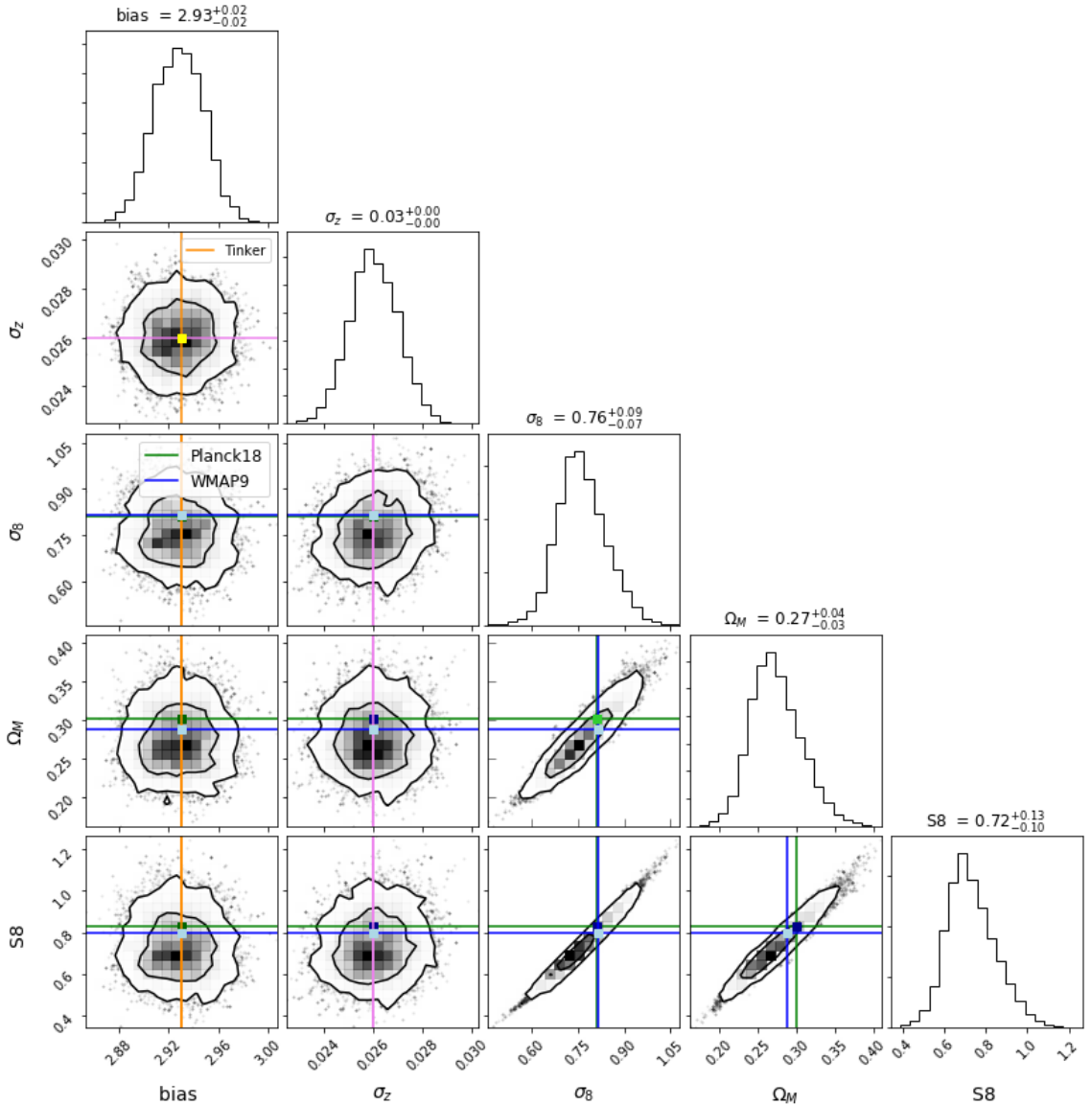


**Figure 6.16:** The 68% – 95% confidence contours and the posterior distribution for the free parameters ( $\sigma_z$ , bias,  $\sigma_8$  and  $\Omega_M$ ) and also for the derived parameter ( $S_8$ ) exploiting our measurements in the range in  $z$   $0.35 < z < 0.8$ . The coloured line represent the expected values: the expected bias (orange line) is assumed to be the Tinker value; the  $\sigma_z$  expected values is assumed to be the mean value in the catalogue for this bin; the expected value for the cosmological parameters are represented by the blue lines and the green lines, respectively from WMAP9 and Planck18 (for Planck18:  $\Omega_M = 0.301$  and  $\sigma_8 = 0.8102$ ; for WMAP9:  $\Omega_M = 0.288$  and  $\sigma_8 = 0.817$ ).

With the MCMC analysis, we obtain the confidence contours for the two independent bins in redshift and mass, and assess the marginalised posterior distributions; Fig.6.17 shows the results for  $\sigma_8$ ,  $\Omega_M$  and  $S_8$  in the two redshift bins considered.

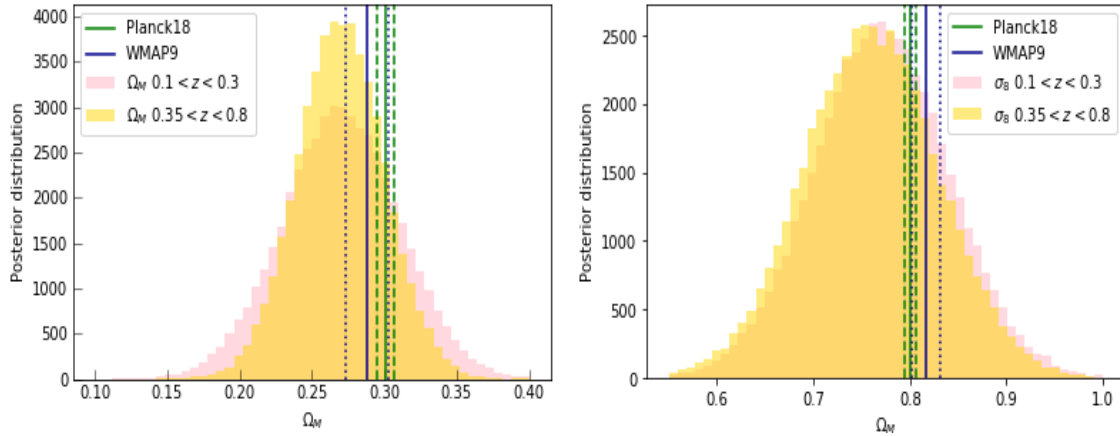


**Figure 6.17:** The combination of the posterior distributions in the two independent redshift bins for  $\sigma_z$  and  $\Omega_M$ . With the pink histogram are represented the results obtained in the redshift range 0.1 – 0.3, while, with the yellow histogram are represented the results obtained in the redshift range 0.35 – 0.8. The Planck18 (solid green line, the dashed green lines shows the 1- $\sigma$  errors) and WMAP9 (solid blue line, the dotted blue lines shows the 1- $\sigma$  errors)

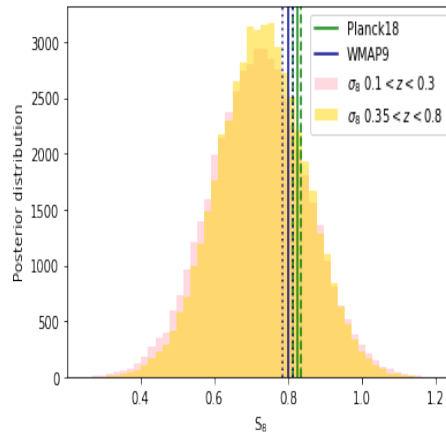


**Figure 6.18:** The combination of the posterior distributions in the two independent redshift bins for  $S_8$ . With the pink histogram are represented the results obtained in the redshift range 0.1 – 0.3, while, with the yellow histogram are represented the results obtained in the redshift range 0.35 – 0.8. The Planck18 (solid green line, the dashed green lines shows the 1- $\sigma$  errors) and WMAP9 (solid blue line, the dotted blue lines shows the 1- $\sigma$  errors)

Exploiting the combination of the posterior distribution, illustrated in Fig.6.17, we obtain:

- $\sigma_8 = 0.77 \pm 0.04$
- $\Omega_M = 0.27 \pm 0.02$
- $S_8 = 0.72 \pm 0.09$

we find consistent results from the analysis of the 2PCF in the sub-samples selected in mass. Repeating the analysis in the same bins but assuming WMAP9 as the fiducial cosmology, we find

- $\sigma_8 = 0.76 \pm 0.05$
- $\Omega_M = 0.26 \pm 0.02$

- $S_8 = 0.72 \pm 0.08$

combining the posterior distributions for the two ranges in redshift.

Our measurements appear fully consistent with  $\Lambda$ CDM predictions. However, The AMICO-KiDS clustering uncertainties are still too large to allow us to discriminate between WMAP9 and Planck18 cosmologies: both appear consistent with the data.

Finally, also the  $w_0$  is let free in the MCMC analysis. The prior is assumed uniform for  $w_0$  in the range  $[-5, 1]$ , while for  $\sigma_8$  and  $\Omega_M$  the priors are assumed Gaussian with mean at 0.8 and 0.3 respectively, and with the standard deviations equal to 0.1. Assuming all the cosmological parameters, the degeneracy among them is not broken. For each redshift and mass range we obtain the 68%–95% confidence contours for our free parameters ( $\sigma_z$ ,  $b_{eff}$ ,  $\sigma_8$ ,  $\Omega_M$  and  $w_0$ ) and also for the derived parameter ( $S_8$ ). Fig.6.19 shows the results for the redshift bin  $0.35 < z < 0.8$ . All the posterior distributions are narrower than the prior distribution. Figs.6.20-6.21 report the combination of the posterior distributions obtained in the two ranges in  $z$ , compared with the expected value in Planck18 and WMAP9.

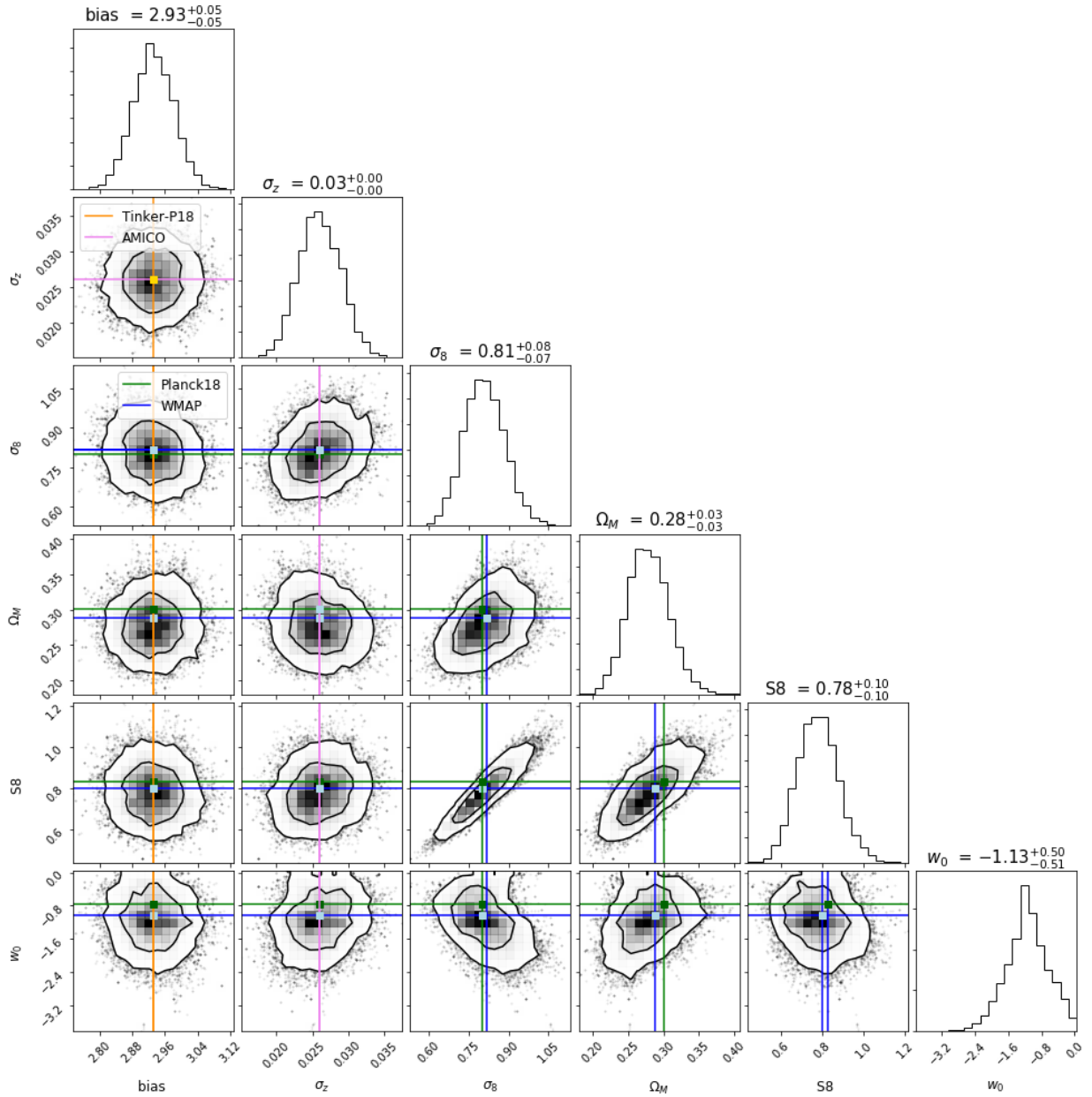


**Figure 6.19:** The 68% – 95% confidence contours for the free parameters ( $\sigma_z$ , bias,  $\sigma_8$ ,  $\Omega_M$  and  $w_0$ ) and also the derived parameter ( $S_8$ ). The coloured line represent the expected values: the bias expected values (orange line) is assumed to be the Tinker value; the  $\sigma_z$  expected values is assumed to be the mean value for this bin in the catalogue; the expected value for the cosmological parameters are represented by the blue lines and the green lines, respectively from WMAP9 and Planck18.

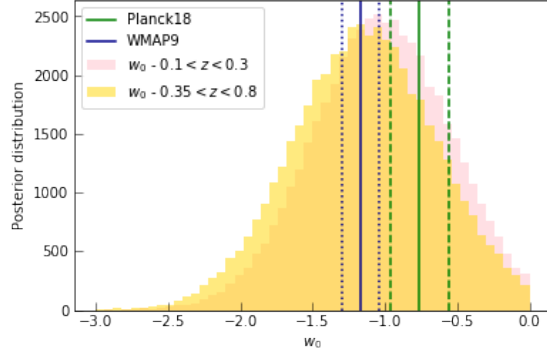


**Figure 6.20:** The combination of the posterior distributions in the two independent redshift bins for  $\sigma_z$  and  $\Omega_M$ . With the orange histogram are represented the results obtained in the redshift range 0.1 – 0.3, while, with the green histogram are represented the results obtained in the redshift range 0.35 – 0.8

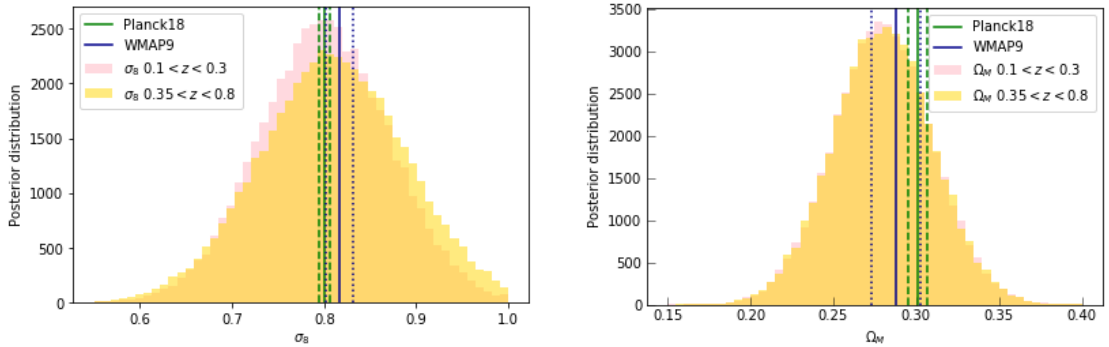


**Figure 6.21:** The combination of the posterior distributions in the two independent redshift bins for  $\sigma_z$  and  $\Omega_M$ . With the orange histogram are represented the results obtained in the redshift range 0.1 – 0.3, while, with the green histogram are represented the results obtained in the redshift range 0.35 – 0.8

Exploiting the combination of the posterior distributions, illustrated in Fig.6.17, we obtain:

- $\sigma_8 = 0.8 \pm 0.04$
- $\Omega_M = 0.28 \pm 0.02$
- $S_8 = 0.73 \pm 0.08$
- $w_0 = -1.07 \pm 0.34$

we find consistent results from the analysis of the 2PCF in the sub-samples selected in mass and also working with the assumption of WMAP9 as the fiducial cosmology.

## 6.6 The scaling relation

As we discussed in Chapter 3, one of the main issue in the study of galaxy clusters is to estimate their mass. In Bellagamba et al. (2019), the weak lensing data are exploited to estimate the clusters mass for the objects detected by AMICO, as illustrated in Section 5.4. Then, with a Bayesian statistical MCMC analysis, the scaling relations between these masses and the mass-proxies computed during the AMICO detection procedure (5.2.3) are defined.

In this Thesis, we propose a new method to estimate the scaling relation with a different approach, which exploits the cluster clustering signal. Specifically, we focus on the scaling relation that links the cluster masses to the intrinsic richness  $\lambda_*$ .

To obtain the normalisation, the slope and the scatter parameters ( $\alpha$ ,  $\beta$  and  $\gamma$ , respectively) of Eq.(5.14), we perform a Bayesian statistical MCMC analysis. The likelihood is defined as in Eq.(6.2). For this statistical approach, we consider the *damped* model for the 2PCF, in which,

as previously explained, the parameters are the mean photo- $z$  error, the bias and the fiducial cosmology. At first, we work with a fiducial cosmology completely defined, thus the cosmological parameters are set as constant values. We assume the  $\sigma_z$  as a free parameters, while the bias is derived. Indeed, the Tinker et al. (2010) model function considered to model the bias depends on the fiducial cosmology, the redshift and the mass. The masses for this work are expressed as in Eq.5.14, in which  $\alpha$ ,  $\beta$ ,  $\gamma$  are let as free parameters. Therefore, with this statistical analysis, we obtain the posterior distribution for  $\sigma_z$ ,  $\alpha$ ,  $\beta$  and  $\gamma$  and also for the derived bias.

We perform this statistical analysis in two redshift ranges (described in Table 6.2). In Eq.5.14 we assume  $z_{piv}$  equal to 0.412, while  $\lambda_{piv} = 24.5$  because we work on the entire redshift range ( $0.1 < z < 0.8$ ) instead of  $0.1 < z < 0.6$ .

In the MCMC analysis we assume Gaussian priors for both  $\beta$  and  $\gamma$  with the mean as the mean values in Bellagamba et al. (2019) and standard deviations equal to 1. The resulting posterior distributions for all the free parameters are shown in Fig.6.22 in which we can see how their standard deviations are reduced respect to the assigned prior distributions.

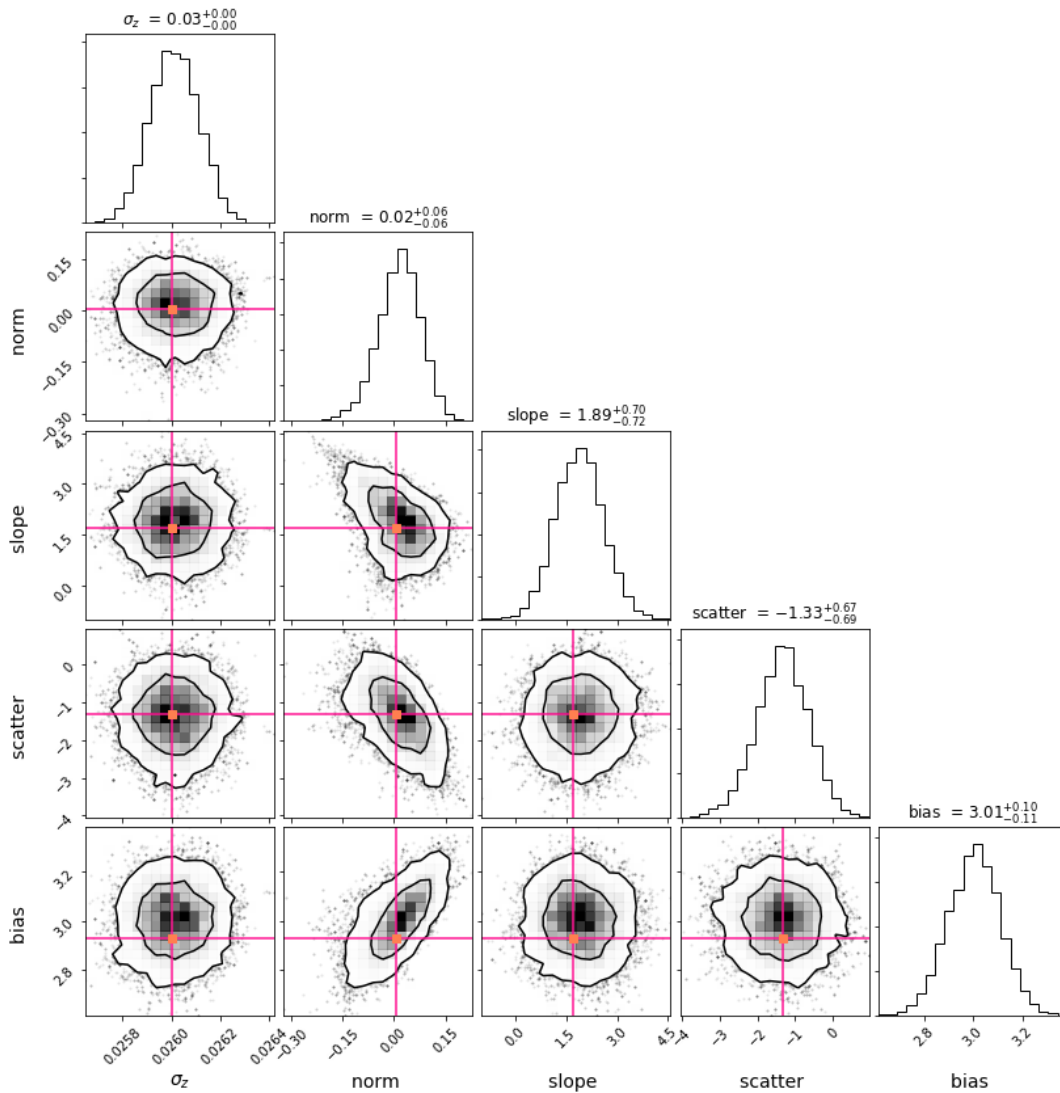


**Figure 6.22:** The 68% – 95% confidence contours and the posterior distribution for the free parameters ( $\sigma_z$ ,  $\alpha$ ,  $\beta$  and  $\gamma$ ) and also the derived parameter ( $b_{eff}$ ) obtained analysing our 2PCF measurements in the redshift range  $0.35 < z < 0.8$ . The coloured line represent the expected values: the bias expected values is assumed to be the Tinker value; the  $\sigma_z$  expected values is assumed to be the mean value for this bin in the catalogue; for the scaling relation parameters the expected values reported are given by the results obtained in Bellagamba et al., 2019

Performing the same analysis on both the redshift intervals and combining the resulting posterior distributions, as shown in Fig.6.23 we obtain:

- $\alpha = 0.04 \pm 0.05$
- $\beta = 1.88 \pm 0.48$
- $\gamma = -1.32 \pm 0.48$

while, the bias estimated in the two redshift bins are  $1.88 \pm 0.1$  and  $3.01 \pm 0.1$ .

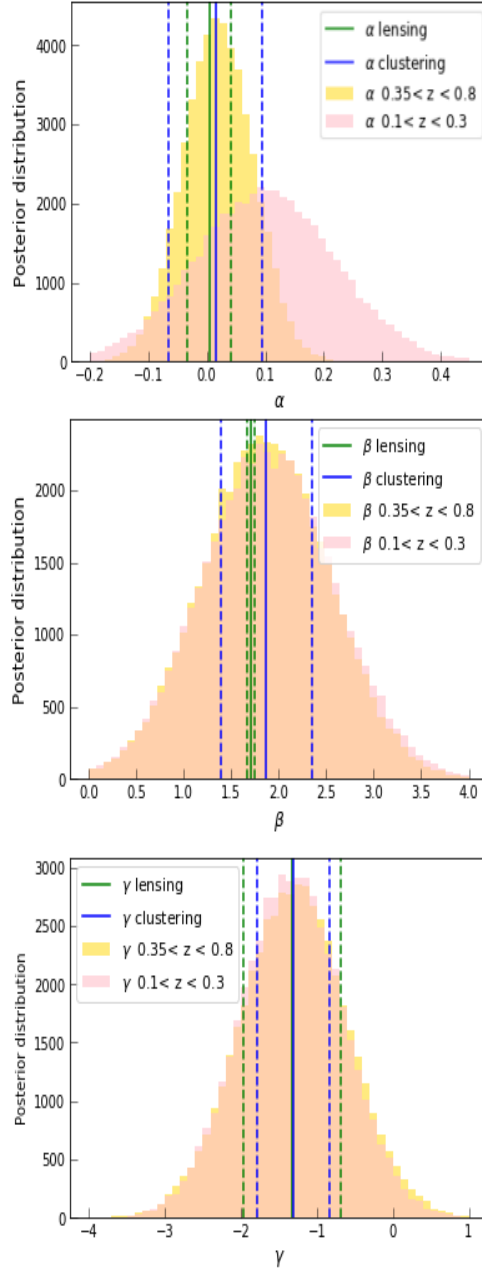


**Figure 6.23:** The combination of the posterior distributions in the two independent redshift bins for  $\alpha$ ,  $\beta$  and  $\gamma$ . With the pink histogram are represented the results obtained in the redshift range 0.35 – 0.8, while, with the yellow histogram are represented the results obtained in the redshift range 0.1 – 0.3. The  $\alpha$ ,  $\beta$  and  $\gamma$  obtained in Bellagamba et al., 2019 are shown (solid green line, the dashed green lines shows the 1- $\sigma$  errors). The results for  $\alpha$ ,  $\beta$  and  $\gamma$  obtained with our analysis combining the results in the two redshift bins are reported (solid blue line, the dotted blue lines shows the 1- $\sigma$  errors).

Then, we perform the same analysis but also with two others free terms:  $\sigma_8$  and  $\Omega_M$ . Their prior are defined as Gaussian centred on Planck18 values, assuming as mean the values given by Planck18 ( $\Omega_M = 0.301$  and  $\sigma_8 = 0.8102$ ) and as standard deviations the  $1-\sigma$  errors computed in Planck18 (respectively  $\pm 0.0056$  and  $0.006$ ). The resulting posterior distributions for all the free parameters are shown in Fig.6.24 in which we can see how their standard deviations are reduced respect the first case but also respect the assigned prior distribution.

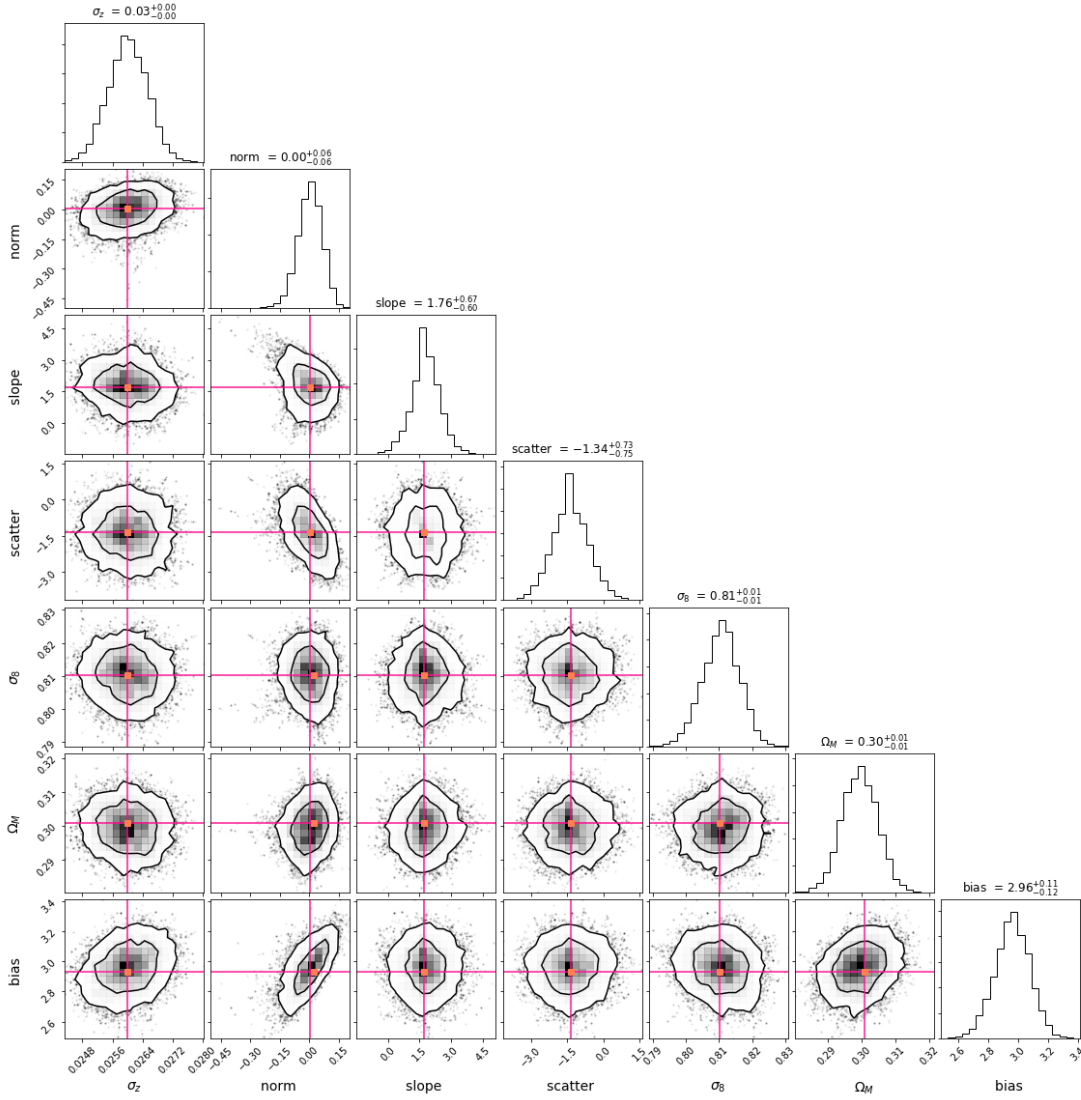


**Figure 6.24:** The 68%–95% confidence contours and the posterior distribution for the free parameters ( $\sigma_z$ ,  $\alpha$ ,  $\beta$ ,  $\gamma$ ,  $\Omega_M$  and  $\sigma_8$ ) and also the derived parameter ( $b_{eff}$ ) obtained analysing our 2PCF measurements in the redshift range  $0.35 < z < 0.8$ . The coloured line represent the expected values: the bias expected values is assumed to be the Tinker value; the  $\sigma_z$  expected values is assumed to be the mean value for this bin in the catalogue; for the scaling relation parameters the expected values reported are given by the results obtained in Bellagamba et al., 2019; for the cosmological parameter are shown the value estimated by Planck18.

Performing the same analysis on both the redshift intervals and combining the resulting posterior distributions, shown in Fig.6.25, we obtain:

- $\alpha = 0.013 \pm 0.045$
- $\beta = 1.69 \pm 0.490$
- $\gamma = -1.29 \pm 0.515$

while, the cosmological parameters are

- $\Omega_M = 0.299 \pm 0.0037$
- $\sigma_8 = 0.810 \pm 0.0034$

and the derived bias are  $1.86 \pm 0.10$  and  $2.95 \pm 0.11$ .

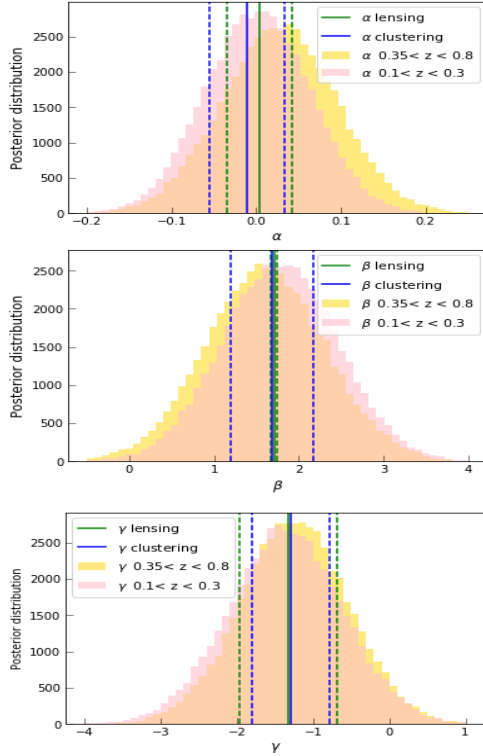


**Figure 6.25:** The combination of the posterior distributions in the two independent redshift bins for  $\alpha$ ,  $\beta$  and  $\gamma$ . With the pink histogram are represented the results obtained in the redshift range  $0.35 - 0.8$ , while, with the yellow histogram are represented the results obtained in the redshift range  $0.1 - 0.3$ . The  $\alpha$ ,  $\beta$  and  $\gamma$  obtained in Bellagamba et al., 2019 are shown (solid green line, the dashed green lines shows the  $1-\sigma$  errors). The results for  $\alpha$ ,  $\beta$  and  $\gamma$  obtained with our analysis combining the results in the two redshift bins are reported (solid blue line, the dotted blue lines shows the  $1-\sigma$  errors).

Therefore, with our results we show how the clustering measure can be exploited to constrain the scaling-relation between the cluster mass and the richness.

## 6.7 Comparison between the different bias estimation

In this Thesis, the bias is estimated in four different way: assuming the Tinker theoretical model (defined in Section 4.6 and employed in Section 6.2) and by carrying out a Bayesian statistical MCMC analysis (see Appendix A) of the measured 2PCF in three different contexts. In the first analysis, we compare our 2PCF measurements with the theoretical model presented in Section 4.5.2 having as free parameters both the bias and the mean photo-z error and with a fiducial cosmology assumed (in Section 6.4). Then, in the same context, we assume a fiducial cosmology

but with different cosmological parameters set as free together with the bias and the mean photo-z error (Section 6.5). Finally, we also obtain the bias as a derived parameter constraining the *scaling-relation* between the intrinsic richness and the mass, as explained in Section 6.6. The obtained results are consistent, as shown in Fig.6.26

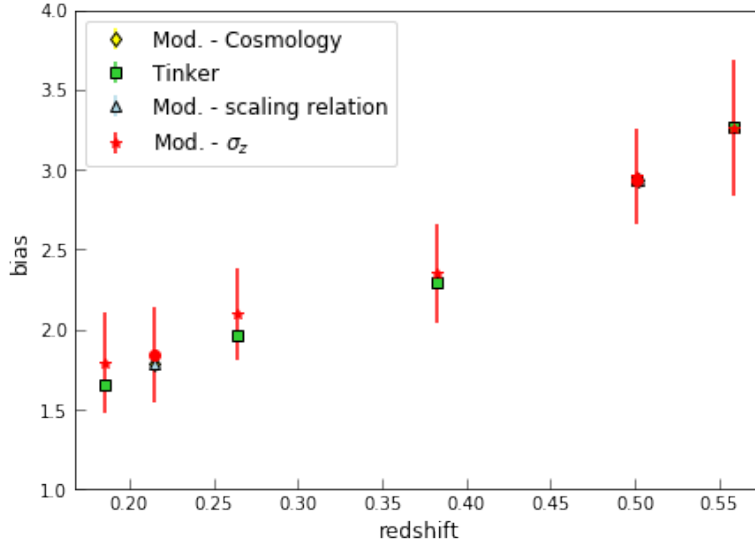


**Figure 6.26:** Comparison between the effective bias estimated in various sub-ranges in redshift with the different approach. With the yellow diamonds are reported the values computed during the Bayesian analysis to infer cosmological parameters together with the bias; with the green squares are represented the value obtained assuming the Tinker model; the blue triangles illustrates the bias obtained as derived parameter performing the Bayesian analysis to constrain the scaling relation; with the red stars are reported the value obtained with the statistical analysis carried out to constrain the bias together with the photo-z error.

# Chapter 7

## Discussion and conclusions

### 7.1 Scientific background

According to the  $\Lambda$ CDM cosmological model, galaxy clusters form in the rare highest peaks of the cosmological density field. Therefore, being both relatively rare objects and the largest gravitationally bound systems in the Universe, they provide stringent constraints on theories of structure formation, tracing the statistical properties of the matter density field and its growth.

To describe the underlying density field of the LSS of the Universe, it is necessary to employ large samples of cosmic tracers. Therefore, extended galaxy surveys have been largely utilised for this study. However, despite the larger size of galaxy samples relative to cluster ones, and the difficulty in constructing complete and pure cluster catalogues, covering broad ranges of masses and redshifts, there are many advantages to exploiting clusters as cosmic tracers. Firstly, clusters trace the massive dark matter haloes and are more clustered than galaxies. Moreover, their effective bias is defined as a function of the cosmological model, while the galaxy bias cannot be defined in this way, being stochastic and a function of the galaxy properties such as luminosity, colour and/or morphological type. Moreover, using different tracers is fundamental in cosmology. Indeed, to test possible failures of the standard  $\Lambda$ CDM model and to verify its predictions the best way is exploiting independent probes to measure cosmological parameters, and comparing the estimated values from different experiments to assess their robustness.

In the  $\Lambda$ CDM scenario, both the correlation function and the power spectrum describe the statistical properties of the perturbed density field. As we discuss in Chapter ??, the correlation functions have been the standard way of describing the clustering in cosmology since 1960s (more details can be found in that Chapter and in the references reported). We also explain how the clustering can be measured through the 2PCF, defined as the Fourier transform of the power spectrum, and how that is one of the most successful statistics for analysing clustering processes, being a privileged tool for testing structure formation and evolution models.

As already mentioned, the cluster correlation function is much higher than that of galaxies (Bahcall et al., 1983) as a consequence of their formation in the most massive haloes, that correspond to the highest and rarest density fluctuations in the matter density distribution. Therefore, they are characterised by a higher correlation signal as shown in Kaiser (1984). The evolution of the cluster halo mass, bias and clustering has been examined analytically (Mo et al., 1996; Moscardini et al., 2000; Sheth et al., 2001). The increase of the correlation length with cluster mass and redshift has been used to constrain the cosmological model and the bias (see for example Colberg et al., 2000; Bahcall et al., 2004).

The abundance of galaxy clusters and the 2PCF have been used since 90's to constrain the mean matter density in the Universe,  $\Omega_M$ , and the amplitude of the density fluctuations in terms of  $\sigma_8$ . For example, in Eke et al. (1998), the evolution of the abundance of galaxy clusters is exploited to estimate  $\Omega_M$ , working on X-ray survey obtained with ASCA at  $z < 0.4$ . The estimated value for  $\Omega_M$  was  $0.45 \pm 0.25$ . Also in Borgani et al. (2001) constraints on  $\Omega_M$  are obtained exploiting an X-ray cluster survey acquired with Chandra in the redshift range  $0.57 \leq z \leq 1.27$ . The estimated values are  $\Omega_M = 0.35_{-0.10}^{+0.13}$  and  $\sigma_8 = 0.66_{-0.05}^{+0.06}$ . Reiprich et al. (2002) constrained both  $\sigma_8$  and  $\Omega_M$  analysing ROSAT All-Sky Survey in the redshift range

$z \leq 0.3$  measuring  $\Omega_M = 0.12_{-0.04}^{+0.06}$  and  $\sigma_8 = 0.96_{-0.12}^{+0.15}$ .

More recent studies, using cluster catalogues selected in the X-ray and optical wavelengths, provided better constraints on  $\sigma_8$  and  $\Omega_M$ . The abundance and clustering of galaxy clusters have been also used in combination with gravitational lensing and BAO to place competitive constraints. Rozo et al. (2010) studied the abundance of clusters in the Sloan Digital Sky Survey maxBCG cluster catalogue together with weak lensing mass measurements to constrain  $\sigma_8$  (equal to  $0.807 \pm 0.020$ ) and  $\Omega_M$  (equal to  $0.265 \pm 0.016$ ). In Sereno et al. (2015b) the weak lensing signal is exploited together with the correlation function to constrain both the effective bias and  $\sigma_8$  (that is found to be equal to  $0.78 \pm 0.16$ ). In Vikhlinin et al. (2009), it is studied the cluster mass functions of clusters in the Chandra survey, in order to constrain  $w_0$ , that is  $-1.14 \pm 0.21$ . Marulli et al. (2018) constrained  $\Omega_M$  analysing the redshift-space 2PCF of the X-ray selected XXL cluster catalogue.

Large galaxy cluster samples can be efficiently extracted from photometric galaxy surveys, as explained in Chapter 5, where we presented the cluster catalogue detected by the AMICO code from the KiDS-3DR survey. However, photometric redshift uncertainties cause a damping in the 2PCF, especially at small scales, that has to be properly taken into account in the likelihood model to avoid systematics, as we discussed in Chapter 3. The distortions caused by the photo- $z$  errors can be modelled by adding a Gaussian damping term to the power spectrum (see Eq. (4.18)), as explained in 4.5.2.

Another major issue in constraining cosmological model parameters with galaxy clusters comes from uncertainties in cluster mass estimates. As we explained in Chapter 3, cluster properties, such as the optical richness, can be used as mass proxies. This requires to accurately calibrate the relation between these observable quantities and direct mass estimates, such as weak lensing masses, as done e.g. in Bellagamba et al., 2019 (for a brief overview see Section 3.2).

The combination of different observables, such as gravitational lensing and clustering, provides a viable method to self calibrate the mass-observable relation. For instance, Costanzi et al. (2018) combined cluster abundances and stacked weak gravitational lensing mass measurements from the Sloan Digital Sky Survey data to simultaneously constrain cosmology and the richness-mass relation of galaxy clusters in the redshift range  $0.1 < z < 0.3$ .

## 7.2 Discussion

In this Thesis, we presented the clustering properties of a photometric sample obtained with the AMICO code from the third data release of the KiDS survey (see Chapter ??). The catalogue consists of 7936 clusters in the redshift range  $0.1 < z < 0.8$ , with the mean redshift equal to 0.412, while the mass range is  $0.017 M_\odot/h \leq M_{200} \leq 13.279 M_\odot/h$ .

As previously discussed, one of the main problems in exploiting photometric surveys is that the errors on the photometric redshifts cannot be neglected and have to be properly modelled in the likelihood. In the presented analysis, we introduced a Gaussian damping factor in the model power spectrum to take into account the photo- $z$  errors in the 2PCF modelling.

As illustrated in Chapter 6, the main results of this Thesis work can be summarised as follows:

- We presented the first measurements of the redshift-space 2PCF for the entire AMICO-KiDS sample, as well as for different mass and redshift selected sub-catalogues (for which the main characteristics are presented in Tables 6.1-6.2-6.3). As expected in the  $\Lambda$ CDM scenario, we found that the clustering signal increases with cluster mass and redshift, as shown in Figs.6.2-6.3-6.4. Moreover, we estimated the effective bias of the samples, defined in Eq.(6.1), assuming the Tinker model, presented in Section 4.6.1. The derived redshift and mass dependence of the effective bias is consistent with  $\Lambda$ CDM predictions.
- We derive the real-space correlation scale length and slope from the projected 2PCF for all the analysed sub-catalogues. Our results (shown in Fig.6.7) demonstrate how the correlation length increases both with redshift and the mass of the clusters, as expected, while the slope stays approximately constant.
- The effective bias and the mean photo- $z$  error in the full sample and in the different sub-catalogues are estimated with a Bayesian statistical MCMC analysis. We obtained results perfectly consistent with the expected values estimated with the Tinker bias model and measuring the mean photo- $z$  error directly from the catalogue.
- With a Bayesian analysis we derived constraints on both the cosmological parameters and the cluster effective bias. Firstly, we focus on the standard  $\Lambda$ CDM model, constraining  $\sigma_8$  and  $\Omega_M$ , and estimating  $S_8$  as their derived parameter. We found:

- $\sigma_8 = 0.77 \pm 0.04$
- $\Omega_M = 0.27 \pm 0.02$
- $S_8 = 0.72 \pm 0.09$

Then, we explored an extended cosmological framework with also  $w_0$  as a free parameter. In this case, we get:

- $\sigma_8 = 0.8 \pm 0.04$
- $\Omega_M = 0.28 \pm 0.02$
- $S_8 = 0.73 \pm 0.08$
- $w_0 = -1.07 \pm 0.34$

Indeed, with our data it could be possible to break the degeneracy between the effective bias of the sample and the main cosmological parameters, as shown by the posterior distributions presented in Figs.6.16-6.19. However, with our clustering uncertainties it is not possible to discriminate between WMAP9 and Planck18 cosmologies. Indeed both appear consistent with the data.

- Finally, we exploited the clustering signal to constrain the cluster scaling relation (defined in Eq.5.14), which links the mass and the richness of the clusters. Specifically, we performed a Bayesian statistical analysis to estimate the normalisation  $\alpha$ , the slope  $\beta$ , and the scatter  $\gamma$  in Eq.(5.14). In this analysis, the effective bias is a derived parameter. We obtain:

- $\alpha = 0.04 \pm 0.05$
- $\beta = 1.88 \pm 0.48$
- $\gamma = -1.32 \pm 0.48$

### 7.3 Conclusion and future perspectives

To test the cosmological model and constrain its parameters, it is fundamental to exploit independent probes of the LSS of the Universe. With this Thesis work, we illustrated how it is possible to extract cosmological constraints from the redshift-space 2PCF of photometric galaxy cluster catalogues. To achieved this goal, it is necessary to accurately take into account the photo- $z$  errors in the likelihood model. In our work, we exploit the 2PCF to constrain both the cosmological parameters and the parameters of the cluster scaling relation. The obtained cosmological constraints are in excellent agreement with  $\Lambda$ CDM predictions, though not narrow enough to discriminate between WMAP9 and Planck18 cosmologies. With a larger cluster sample it would be possible to obtain stronger constraints, because clustering uncertainties would be smaller and, also, because it will be possible perform the same statistical analysis in a larger set of independent bins of mass and redshift.

We performed also a new method to constrain the cluster scaling relation parameters from the 2PCF signal. In particular, we provided new independent constraints on the relation between cluster richness and mass. These results will be used to improve cosmological constraints from cluster number count analyses. Moreover, in a forthcoming work we plan to combine these results with gravitational lensing data on the same sample to better constrain the scaling relation parameters.

# Appendix A

## Bayesian statistics

In the Bayesian approach, the probability is a measure of the degree of plausibility of a statement. Moreover, the probability of any event is determined by taking into account also the prior knowledge we might have on that event. With this approach, we can calculate the probability of a model, or the probability of its parameters, giving the data and any prior knowledge. One of the advantages of the Bayesian approach is that it enables us to assign the probability that a model is the best one in describing the data, compared to the other considered models.

The Bayesian statistics is based on the Bayes theorem. Assuming that  $D$  is some set of data and  $\Theta = (\theta_1, \dots, \theta_m)$  is the  $m$ -dimensional unknown parameter vector of a certain model, then the Bayes theorem can be expressed as:

$$P(\Theta|D) = \frac{P(\Theta)P(D|\Theta)}{P(D)} = \frac{P(\Theta|D)P(\theta)}{\int P(\Theta|D)P(\Theta) d\Theta}, \quad (\text{A.1})$$

where  $P(\Theta|D)$  is the multivariate posterior distribution, that is the deduced joint probability distribution of the parameters, after considering the data. This is estimated by calculating the **likelihood**,  $P(D|\Theta) \equiv \mathcal{L}(D|\Theta)$ , which is the conditional probability of obtaining the observed data given a set of input parameter values, and by setting a prior probability on the parameters themselves,  $P(\Theta)$ . The likelihood represents the mismatch between data and theoretical expectations. The prior, instead, denotes the a priori knowledge on the distribution of the expectation values of the parameters, before examining any measurement. The normalisation constant  $P(D)$  is called evidence, or marginal likelihood. From Eq.(A.1), it can be demonstrated that it is equal to the integral over  $\Theta$  of the likelihood times the prior. Hence, the general problem of posterior estimation is to calculate an integral. To compress the posterior distribution to a set of samples can save a vast amount of computational time, if compared to the integration over the  $m$ -dimensional parameter space. This can be done efficiently exploiting a sampling approach.

The most common method for sampling from a general distribution in high-dimensions is the Markov Chain Monte Carlo (MCMC) sampling method, based on the Monte Carlo approximation method and on the useful properties of the Markov Chains.

If we consider that  $X$  is a random variable and  $X_t$  is its value at time  $t$ , we define  $X$  as a Markov process if the probability distribution at the present status,  $X_t$ , depends only on the previous status,  $X_{t-1}$ , and not on the entire history:

$$P(X_t = x_t | X_0 = x_0, \dots, X_{t-1} = x_{t-1}) = P(X_t = x_t | X_{t-1} = x_{t-1}).$$

If the probability is regular, the chain will gradually forget about the initial state  $X_0$  and approach an invariant distribution after a sufficient number of steps.

The Monte Carlo integration utilises the extraction of random numbers to evaluate a multidimensional integral that cannot be computed analytically or by using one-dimensional approaches. This method is exploited when the number of dimensions is high and/or the boundaries for the integration are complex.

Through the MCMC we can sample the posterior distribution, focusing on the regions where it is larger. The term Monte Carlo refers to the fact that for the computation we recourse to a repeated random sampling.

# Bibliography

- Abell, G. O. (1958). “The Distribution of Rich Clusters of Galaxies.” In: 3, p. 211. DOI: [10.1086/190036](https://doi.org/10.1086/190036).
- Aghanim, F. et al. (2018a). “Planck 2018 results. VI. Cosmological parameters”. In: arXiv: [1807.06209](https://arxiv.org/abs/1807.06209) [[astro-ph.CO](https://arxiv.org/abs/1807.06209)].
- Aghanim, N. et al. (2018b). “Planck 2018 results. VI. Cosmological parameters”. In: arXiv: [1807.06209](https://arxiv.org/abs/1807.06209) [[astro-ph.CO](https://arxiv.org/abs/1807.06209)].
- Alam, Shadab et al. (2016a). “Testing deviations from CDM with growth rate measurements from six large-scale structure surveys at  $z=0.06-1$ ”. In: *Monthly Notices of the Royal Astronomical Society* 456.4, pp. 3743–3756. ISSN: 0035-8711. DOI: [10.1093/mnras/stv2935](https://doi.org/10.1093/mnras/stv2935). eprint: <http://oup.prod.sis.lan/mnras/article-pdf/456/4/3743/9384512/stv2935.pdf>. URL: <https://doi.org/10.1093/mnras/stv2935>.
- Alam, S. et al. (2016b). “Testing deviations from  $\Lambda$ CDM with growth rate measurements from six large-scale structure surveys at  $z=0.06-1$ ”. In: 456, pp. 3743–3756. DOI: [10.1093/mnras/stv2935](https://doi.org/10.1093/mnras/stv2935). arXiv: [1509.05034](https://arxiv.org/abs/1509.05034).
- Allen, S. W. et al. (2001). “The X-ray virial relations for relaxed lensing clusters observed with Chandra”. In: 328, pp. L37–L41. DOI: [10.1046/j.1365-8711.2001.05079.x](https://doi.org/10.1046/j.1365-8711.2001.05079.x). eprint: [astro-ph/0110610](https://arxiv.org/abs/astro-ph/0110610).
- Andreon et al. (2010). “The scaling relation between richness and mass of galaxy clusters: A Bayesian approach”. In: *Monthly Notices of the Royal Astronomical Society* 404.
- Arnaud, M. et al. (2005). “The structural and scaling properties of nearby galaxy clusters - II. The M-T relation”. In: *A&A* 441.3, pp. 893–903. DOI: [10.1051/0004-6361:20052856](https://doi.org/10.1051/0004-6361:20052856). URL: <https://doi.org/10.1051/0004-6361:20052856>.
- Bahcall, N. A. et al. (1983). “The spatial correlation function of rich clusters of galaxies”. In: 270, pp. 20–38. DOI: [10.1086/161094](https://doi.org/10.1086/161094).
- Bahcall, Neta A. et al. (2004). “Evolution of the Cluster Correlation Function”. In: *The Astrophysical Journal* 603.1, pp. 1–6. DOI: [10.1086/381386](https://doi.org/10.1086/381386). URL: <https://doi.org/10.1086/381386>.
- Baum, W. A. (1962). *Photoelectric Magnitudes and Red-Shifts*. Ed. by G. C. McVittie. Vol. 15. IAU Symposium, p. 390.
- Bellagamba, F. et al. (2011). “Optimal filtering of optical and weak lensing data to search for galaxy clusters: application to the COSMOS field”. In: *Monthly Notices of the Royal Astronomical Society* 413.2, pp. 1145–1157. ISSN: 0035-8711. DOI: [10.1111/j.1365-2966.2011.18202.x](https://doi.org/10.1111/j.1365-2966.2011.18202.x). eprint: <http://oup.prod.sis.lan/mnras/article-pdf/413/2/1145/18590703/mnras0413-1145.pdf>. URL: <https://doi.org/10.1111/j.1365-2966.2011.18202.x>.
- Bellagamba, F. et al. (2018). “AMICO: optimized detection of galaxy clusters in photometric surveys”. In: 473, pp. 5221–5236. DOI: [10.1093/mnras/stx2701](https://doi.org/10.1093/mnras/stx2701). arXiv: [1705.03029](https://arxiv.org/abs/1705.03029).
- Bellagamba et al. (2019). “AMICO galaxy clusters in KiDS-DR3: weak lensing mass calibration”. In: *Monthly Notices of the Royal Astronomical Society* 484.2, pp. 1598–1615. ISSN: 0035-8711. DOI: [10.1093/mnras/stz090](https://doi.org/10.1093/mnras/stz090). eprint: <http://oup.prod.sis.lan/mnras/article-pdf/484/2/1598/27583209/stz090.pdf>. URL: <https://doi.org/10.1093/mnras/stz090>.
- Bilicki, M. et al. (2018). “Photometric redshifts for the Kilo-Degree Survey - Machine-learning analysis with artificial neural networks”. In: *A&A* 616, A69. DOI: [10.1051/0004-6361/201731942](https://doi.org/10.1051/0004-6361/201731942). URL: <https://doi.org/10.1051/0004-6361/201731942>.
- Binney, J. et al. (1987). *Galactic dynamics*.

- Borgani, S. (2008). *Cosmology with Clusters of Galaxies*. Ed. by Manolis Plionis et al. Dordrecht: Springer Netherlands, pp. 287–334. ISBN: 978-1-4020-6941-3. DOI: [10.1007/978-1-4020-6941-3\\_9](https://doi.org/10.1007/978-1-4020-6941-3_9). URL: [https://doi.org/10.1007/978-1-4020-6941-3\\_9](https://doi.org/10.1007/978-1-4020-6941-3_9).
- Borgani, Stefano et al. (2001). “Measuring  $\Omega_M$  with the ROSAT Deep Cluster Survey”. In: *The Astrophysical Journal* 561.1, pp. 13–21. DOI: [10.1086/323214](https://doi.org/10.1086/323214). URL: <https://doi.org/10.1086/323214>.
- Cavaliere, A. et al. (1976). “X-rays from hot plasma in clusters of galaxies”. In: 49, pp. 137–144.
- Coil, Alison L. (2013). “The Large-Scale Structure of the Universe”. In: *Planets, Stars and Stellar Systems Vol. 6, by Oswalt, Terry D.; Keel, William C., ISBN 978-94-007-5608-3. Springer Science+Business Media Dordrecht, 2013, p. 387*. Ed. by Terry D. Oswalt et al. Vol. 6, p. 387. DOI: [10.1007/978-94-007-5609-0\\_8](https://doi.org/10.1007/978-94-007-5609-0_8).
- Colberg, J. M. et al. (2000). “Clustering of galaxy clusters in cold dark matter universes”. In: *Monthly Notices of the Royal Astronomical Society* 319.1, pp. 209–214. ISSN: 0035-8711. DOI: [10.1046/j.1365-8711.2000.03832.x](https://doi.org/10.1046/j.1365-8711.2000.03832.x). eprint: <http://oup.prod.sis.lan/mnras/article-pdf/319/1/209/3741214/319-1-209.pdf>. URL: <https://doi.org/10.1046/j.1365-8711.2000.03832.x>.
- Costanzi, M. et al. (2018). “Dark Energy Survey Year 1 Results: Methods for Cluster Cosmology and Application to the SDSS”. In: arXiv: [1810.09456](https://arxiv.org/abs/1810.09456) [astro-ph.CO].
- de Jong et al. (2017). “The third data release of the Kilo-Degree Survey and associated data products”. In: *A&A* 604, A134. DOI: [10.1051/0004-6361/201730747](https://doi.org/10.1051/0004-6361/201730747). URL: <https://doi.org/10.1051/0004-6361/201730747>.
- Einstein, A. (1915). “Zur allgemeinen Relativitätstheorie”. In: *Preussische Akademie der Wissenschaften Sitzungsberichte*, pp. 778–801.
- Eke, V. R. et al. (1998). “Measuring  $\Omega_0$  using cluster evolution”. In: 298, pp. 1145–1158. DOI: [10.1046/j.1365-8711.1998.01713.x](https://doi.org/10.1046/j.1365-8711.1998.01713.x). eprint: [astro-ph/9802350](https://arxiv.org/abs/astro-ph/9802350).
- Estrada, Juan et al. (2009). “THE CORRELATION FUNCTION OF OPTICALLY SELECTED GALAXY CLUSTERS IN THE SLOAN DIGITAL SKY SURVEY”. In: *The Astrophysical Journal* 692.1, pp. 265–282. DOI: [10.1088/0004-637x/692/1/265](https://doi.org/10.1088/0004-637x/692/1/265). URL: <https://doi.org/10.1088/0004-637x/692/1/265>.
- Freese, Katherine et al. (2000). “Limits on stellar objects as the dark matter of our halo: non-baryonic dark matter seems to be required”. In: *Nucl. Phys. Proc. Suppl.* 80, p. 0305. arXiv: [astro-ph/9904401](https://arxiv.org/abs/astro-ph/9904401) [astro-ph].
- Friedmann, A. (1922). “Über die Krümmung des Raumes”. In: *Zeitschrift für Physik*, pp. 377–386.
- Fuchs, B. (2001). “The Amount of Dark Matter in Spiral Galaxies”. In: *Astro- and Particle Physics*, p. 25.
- Giacconi, R. et al. (1972). “The Uhuru catalog of X-ray sources.” In: 178, pp. 281–308.
- Giodini, S et al. (2013). “Scaling Relations for Galaxy Clusters: Properties and Evolution”. In: *Space Science Reviews* 177. DOI: [10.1007/s11214-013-9994-5](https://doi.org/10.1007/s11214-013-9994-5).
- Guth, Alan H. (1981). “Inflationary universe: A possible solution to the horizon and flatness problems”. In: *Phys. Rev. D* 23, pp. 347–356.
- Hamilton, A. J. S. (1992). “Measuring  $\Omega$  and the real correlation function from the redshift correlation function”. In: 385, pp. L5–L8. DOI: [10.1086/186264](https://doi.org/10.1086/186264).
- He, Jian-hua et al. (2018). “No evidence for modifications of gravity from galaxy motions on cosmological scales”. In: *Nat. Astron.* 2.12, pp. 967–972. DOI: [10.1038/s41550-018-0573-2](https://doi.org/10.1038/s41550-018-0573-2). arXiv: [1809.09019](https://arxiv.org/abs/1809.09019) [astro-ph.CO].
- Hennig, C. et al. (2017). “Galaxy populations in massive galaxy clusters to  $z = 1.1$ : colour distribution, concentration, halo occupation number and red sequence fraction”. In: *Monthly Notices of the Royal Astronomical Society* 467.4, pp. 4015–4035.
- Herschel, W. (1785). “On the Construction of the Heavens.” In: *Philosophical Transactions of the Royal Society of London Series I* 75, pp. 213–266.
- Hinshaw, C. et al. (2013). “Nine-year Wilkinson Microwave Anisotropy Probe (WMAP) Observations: Cosmological Parameter Results”. In: *The Astrophysical Journal Supplement Series* 208.2, 19, p. 19. DOI: [10.1088/0067-0049/208/2/19](https://doi.org/10.1088/0067-0049/208/2/19). arXiv: [1212.5226](https://arxiv.org/abs/1212.5226) [astro-ph.CO].
- Hubble, Edwin (1929). “A relation between distance and radial velocity among extra-galactic nebulae”. In: *Proceedings of the National Academy of Sciences* 15.3, pp. 168–173. DOI: [10.1073/pnas.15.3.168](https://doi.org/10.1073/pnas.15.3.168).

- Huterer, Dragan et al. (2015). “Growth of Cosmic Structure: Probing Dark Energy Beyond Expansion”. In: *Astropart. Phys.* 63, pp. 23–41. DOI: [10.1016/j.astropartphys.2014.07.004](https://doi.org/10.1016/j.astropartphys.2014.07.004). arXiv: [1309.5385 \[astro-ph.CO\]](https://arxiv.org/abs/1309.5385).
- Jeans, J. H. (1902). “The Stability of a Spherical Nebula”. In: *Philosophical Transactions of the Royal Society of London Series A* 199, pp. 1–53.
- Jones, Bernard J. et al. (2004). “Scaling laws in the distribution of galaxies”. In: *Reviews of Modern Physics* 76.4, pp. 1211–1266. DOI: [10.1103/RevModPhys.76.1211](https://doi.org/10.1103/RevModPhys.76.1211). arXiv: [astro-ph/0406086 \[astro-ph\]](https://arxiv.org/abs/astro-ph/0406086).
- Joyce, Austin et al. (2016). “Dark Energy Versus Modified Gravity”. In: *Annual Review of Nuclear and Particle Science* 66.1, pp. 95–122. DOI: [10.1146/annurev-nucl-102115-044553](https://doi.org/10.1146/annurev-nucl-102115-044553). eprint: [\url{https://doi.org/10.1146/annurev-nucl-102115-044553}](https://doi.org/10.1146/annurev-nucl-102115-044553). URL: [5Curl%7B%20https://doi.org/10.1146/annurev-nucl-102115-044553%7D](https://doi.org/10.1146/annurev-nucl-102115-044553%7D).
- Kaiser, N. (1984). “On the spatial correlations of Abell clusters”. In: 284, pp. L9–L12. DOI: [10.1086/184341](https://doi.org/10.1086/184341).
- (1987). “Clustering in real space and in redshift space”. In: 227, pp. 1–21. DOI: [10.1093/mnras/227.1.1](https://doi.org/10.1093/mnras/227.1.1).
- Kerscher, Martin et al. (2000). “A Comparison of Estimators for the Two-Point Correlation Function”. In: *The Astrophysical Journal* 535.1, pp. L13–L16. DOI: [10.1086/312702](https://doi.org/10.1086%2F312702). URL: <https://doi.org/10.1086%2F312702>.
- Labatie, Antoine et al. (2010). “Uncertainty in 2-point correlation function estimators and BAO detection in SDSS DR7”. In: *arXiv e-prints*, arXiv:1009.1232, arXiv:1009.1232. arXiv: [1009.1232 \[astro-ph.CO\]](https://arxiv.org/abs/1009.1232).
- Landy, S. D. et al. (1993). “Bias and variance of angular correlation functions”. In: 412, pp. 64–71. DOI: [10.1086/172900](https://doi.org/10.1086/172900).
- Li, Ran et al. (2016). “Constraints on the identity of the dark matter from strong gravitational lenses”. In: *Mon. Not. Roy. Astron. Soc.* 460.1, pp. 363–372. DOI: [10.1093/mnras/stw939](https://doi.org/10.1093/mnras/stw939). arXiv: [1512.06507 \[astro-ph.CO\]](https://arxiv.org/abs/1512.06507).
- Lilly, Simon (2014). *JWST and the Assembly of galaxies  $2 < z < 7$* . "[http://www.inaf.it/it/sedi/sede-centrale-nuova/direzione-scientifica/ufficio-spazio/jwst-italian-information-day/Assembly%20of%20galaxies\\_Lilly.pdf](http://www.inaf.it/it/sedi/sede-centrale-nuova/direzione-scientifica/ufficio-spazio/jwst-italian-information-day/Assembly%20of%20galaxies_Lilly.pdf)".
- Lima Neto, Gastao B. et al. (2014). “Structure in galaxy clusters”. In: pp. 277–291. arXiv: [1406.1496 \[astro-ph.CO\]](https://arxiv.org/abs/1406.1496).
- Linder, E. V. et al. (2003). “Cosmic structure growth and dark energy”. In: *Monthly Notices of the Royal Astronomical Society* 346.2, pp. 573–583. ISSN: 0035-8711. DOI: [10.1046/j.1365-2966.2003.07112.x](https://doi.org/10.1046/j.1365-2966.2003.07112.x). eprint: <http://oup.prod.sis.lan/mnras/article-pdf/346/2/573/4294515/346-2-573.pdf>. URL: <https://doi.org/10.1046/j.1365-2966.2003.07112.x>.
- Loewenstein, M. et al. (1998). “Do elliptical galaxies have dark matter?” In: 307, pp. 75–81. DOI: [10.1016/S0370-1573\(98\)00059-3](https://doi.org/10.1016/S0370-1573(98)00059-3).
- Mana, Annalisa et al. (2013a). “Combining clustering and abundances of galaxy clusters to test cosmology and primordial non-Gaussianity”. In: *Monthly Notices of the Royal Astronomical Society* 434.1, pp. 684–695. ISSN: 0035-8711. DOI: [10.1093/mnras/stt1062](https://doi.org/10.1093/mnras/stt1062). eprint: <http://oup.prod.sis.lan/mnras/article-pdf/434/1/684/18495961/stt1062.pdf>. URL: <https://doi.org/10.1093/mnras/stt1062>.
- Mana, Annalisa et al. (2013b). “Combining clustering and abundances of galaxy clusters to test cosmology and primordial non-Gaussianity”. In: *Mon. Not. Roy. Astron. Soc.* 434, p. 684. DOI: [10.1093/mnras/stt1062](https://doi.org/10.1093/mnras/stt1062). arXiv: [1303.0287 \[astro-ph.CO\]](https://arxiv.org/abs/1303.0287).
- Marulli, F. et al. (2013). “The VIMOS Public Extragalactic Redshift Survey (VIPERS). Luminosity and stellar mass dependence of galaxy clustering at  $0.5 < z < 1.1$ ”. In: *Astron. Astrophys.* 557, A17. DOI: [10.1051/0004-6361/201321476](https://doi.org/10.1051/0004-6361/201321476). arXiv: [1303.2633 \[astro-ph.CO\]](https://arxiv.org/abs/1303.2633).
- (2016). “CosmoBolognaLib: C++ libraries for cosmological calculations”. In: *Astron. Comput.* 14, pp. 35–42. DOI: [10.1016/j.ascom.2016.01.005](https://doi.org/10.1016/j.ascom.2016.01.005). arXiv: [1511.00012 \[astro-ph.CO\]](https://arxiv.org/abs/1511.00012).
- (2018). “The XXL Survey: XVI. The clustering of X-ray selected galaxy clusters at  $z \approx 0.3$ ”. In: *Astron. Astrophys.* 620, A1. DOI: [10.1051/0004-6361/201833238](https://doi.org/10.1051/0004-6361/201833238). arXiv: [1807.04760 \[astro-ph.CO\]](https://arxiv.org/abs/1807.04760).
- Marulli et al. (2012). “Cosmology with clustering anisotropies: disentangling dynamic and geometric distortions in galaxy redshift surveys”. In: *Monthly Notices of the Royal Astronomical Society* 426.3, pp. 2566–2580. ISSN: 0035-8711. DOI: [10.1111/j.1365-2966.2012.21875.x](https://doi.org/10.1111/j.1365-2966.2012.21875.x).

- eprint: <http://oup.prod.sis.lan/mnras/article-pdf/426/3/2566/3125539/426-3-2566.pdf>. URL: <https://doi.org/10.1111/j.1365-2966.2012.21875.x>.
- Maturi, M. et al. (2005). “An optimal filter for the detection of galaxy clusters through weak lensing”. In: *A&A* 442.3, pp. 851–860. DOI: [10.1051/0004-6361:20042600](https://doi.org/10.1051/0004-6361:20042600). URL: <https://doi.org/10.1051/0004-6361:20042600>.
- Maturi, Matteo et al. (2018). “AMICO galaxy clusters in KiDS-DR3: sample properties and selection function”. In:
- Maturi, Matteo et al. (2019). “AMICO galaxy clusters in KiDS-DR3: sample properties and selection function”. In: *Monthly Notices of the Royal Astronomical Society* 485.1, pp. 498–512. ISSN: 0035-8711. DOI: [10.1093/mnras/stz294](https://doi.org/10.1093/mnras/stz294). eprint: <http://oup.prod.sis.lan/mnras/article-pdf/485/1/498/27966016/stz294.pdf>. URL: <https://doi.org/10.1093/mnras/stz294>.
- Messier, C. (1784). “Catalogue des Nébuleuses des amas d’Étoiles”. In: *Connaissance des Temps*, pp. 238–282.
- Meszaros, P. (1974). “The behaviour of point masses in an expanding cosmological substratum”. In: 37, pp. 225–228.
- Minkowski, H. (1908). “Raum und Zeit”. In: *Physikalische Zeitschrift* 10, pp. 75–88.
- Mo, H. J. et al. (1996). “An analytic model for the spatial clustering of dark matter haloes”. In: 282, pp. 347–361. DOI: [10.1093/mnras/282.2.347](https://doi.org/10.1093/mnras/282.2.347). eprint: [astro-ph/9512127](http://astro-ph/9512127).
- Moscardini, Lauro et al. (2011). “Cosmology with Numerical Simulations”. In: *Dark Matter and Dark Energy: A Challenge for Modern Cosmology*. Ed. by Sabino Matarrese et al. Dordrecht: Springer Netherlands, pp. 217–237. ISBN: 978-90-481-8685-3. DOI: [10.1007/978-90-481-8685-3\\_4](https://doi.org/10.1007/978-90-481-8685-3_4). URL: [https://doi.org/10.1007/978-90-481-8685-3\\_4](https://doi.org/10.1007/978-90-481-8685-3_4).
- Moscardini, L. et al. (2000). “Predicting the clustering of X-ray selected galaxy clusters in flux-limited surveys”. In: *Monthly Notices of the Royal Astronomical Society* 316.2, pp. 283–298. ISSN: 0035-8711. DOI: [10.1046/j.1365-8711.2000.03494.x](https://doi.org/10.1046/j.1365-8711.2000.03494.x). eprint: <http://oup.prod.sis.lan/mnras/article-pdf/316/2/283/18409225/316-2-283.pdf>. URL: <https://doi.org/10.1046/j.1365-8711.2000.03494.x>.
- Mulroy, Sarah L. et al. (2014). “LoCuSS: The Near-Infrared Luminosity and Weak-Lensing Mass Scaling Relation of Galaxy Clusters”. In: *Mon. Not. Roy. Astron. Soc.* 443.4, pp. 3309–3317. DOI: [10.1093/mnras/stu1387](https://doi.org/10.1093/mnras/stu1387). arXiv: [1407.1767](https://arxiv.org/abs/1407.1767) [[astro-ph.CO](https://arxiv.org/abs/1407.1767)].
- Navarro, J. F. et al. (1997). “A Universal Density Profile from Hierarchical Clustering”. In: 490, pp. 493–508. DOI: [10.1086/304888](https://doi.org/10.1086/304888). eprint: [astro-ph/9611107](http://astro-ph/9611107).
- Norberg, Peder et al. (2009). “Statistical Analysis of Galaxy Surveys - I. Robust error estimation for 2-point clustering statistics”. In: *Mon. Not. Roy. Astron. Soc.* 396, p. 19. DOI: [10.1111/j.1365-2966.2009.14389.x](https://doi.org/10.1111/j.1365-2966.2009.14389.x). arXiv: [0810.1885](https://arxiv.org/abs/0810.1885) [[astro-ph](https://arxiv.org/abs/0810.1885)].
- Norman, Michael L. (2010). *Simulating Galaxy Cluster: Cosmological framework and perturbation growth in linear regime*. "<https://ned.ipac.caltech.edu/level5/Sept11/Norman/Norman2.html>".
- Oukbir, J. et al. (1992). “X-ray clusters in open universes”. In: 262, pp. L21–L24.
- P. Coles, F. Lucchin (2008). *Cosmology: the origin and evolution of cosmic structure*. John Wiley & Sons, LTD.
- Padmanabhan, Nikhil et al. (2005). “Calibrating photometric redshifts of luminous red galaxies”. In: *Monthly Notices of the Royal Astronomical Society* 359.1, pp. 237–250. ISSN: 0035-8711. DOI: [10.1111/j.1365-2966.2005.08915.x](https://doi.org/10.1111/j.1365-2966.2005.08915.x). eprint: <http://oup.prod.sis.lan/mnras/article-pdf/359/1/237/5999764/359-1-237.pdf>. URL: <https://doi.org/10.1111/j.1365-2966.2005.08915.x>.
- Pan, Jun et al. (2000). “Large-scale cosmic homogeneity from a multifractal analysis of the PSCz catalogue”. In: *Monthly Notices of the Royal Astronomical Society* 318.4, pp. L51–L54. ISSN: 0035-8711. DOI: [10.1046/j.1365-8711.2000.03965.x](https://doi.org/10.1046/j.1365-8711.2000.03965.x). eprint: <http://oup.prod.sis.lan/mnras/article-pdf/318/4/L51/2830262/318-4-L51.pdf>. URL: <https://doi.org/10.1046/j.1365-8711.2000.03965.x>.
- Peacock, John A. et al. (2001). “A Measurement of the cosmological mass density from clustering in the 2dF Galaxy Redshift Survey”. In: *Nature* 410, pp. 169–173. DOI: [10.1038/35065528](https://doi.org/10.1038/35065528). arXiv: [astro-ph/0103143](https://arxiv.org/abs/astro-ph/0103143) [[astro-ph](https://arxiv.org/abs/astro-ph/0103143)].
- Pearson, Chris (2018). *Theory of Galaxy Formation*. "<http://www.ir.isas.ac.jp/~cpp/teaching/cosmology/documents/cosmology02-03.pdf>".

- Peebles, P. J. E. (1974). “A model for continuous clustering in the large-scale distribution of matter”. In: *Astrophysics and Space Science* 31.2, pp. 403–410. ISSN: 1572-946X. DOI: [10.1007/BF00644096](https://doi.org/10.1007/BF00644096). URL: <https://doi.org/10.1007/BF00644096>.
- (1980). *The large-scale structure of the universe*.
- Peebles, P. J. E. et al. (1974). “Statistical Analysis of Catalogs of Extragalactic Objects. III. The Shane-Wirtanen and Zwicky Catalogs”. In: 28, p. 19. DOI: [10.1086/190308](https://doi.org/10.1086/190308).
- Pereira, Maria E. S. et al. (2018). “Weak-lensing calibration of a stellar mass-based mass proxy for redMaPPer and Voronoi Tessellation clusters in SDSS Stripe 82”. In: *Mon. Not. Roy. Astron. Soc.* 474.1, pp. 1361–1372. DOI: [10.1093/mnras/stx2831](https://doi.org/10.1093/mnras/stx2831). arXiv: [1708.03329](https://arxiv.org/abs/1708.03329) [[astro-ph.CO](https://arxiv.org/abs/1708.03329)].
- Press, W. H. et al. (1974). “Formation of Galaxies and Clusters of Galaxies by Self-Similar Gravitational Condensation”. In: 187, pp. 425–438. DOI: [10.1086/152650](https://doi.org/10.1086/152650).
- Reiprich, T. H. et al. (2002). “The Mass Function of an X-Ray Flux-limited Sample of Galaxy Clusters”. In: 567, pp. 716–740. DOI: [10.1086/338753](https://doi.org/10.1086/338753). eprint: [astro-ph/0111285](https://arxiv.org/abs/astro-ph/0111285).
- Riess, A. G. et al. (1998). “Observational Evidence from Supernovae for an Accelerating Universe and a Cosmological Constant”. In: 116, pp. 1009–1038. DOI: [10.1086/300499](https://doi.org/10.1086/300499). eprint: [astro-ph/9805201](https://arxiv.org/abs/astro-ph/9805201).
- Riess, Adam G. et al. (2019). “Large Magellanic Cloud Cepheid Standards Provide a 1% Foundation for the Determination of the Hubble Constant and Stronger Evidence for Physics beyond  $\Lambda$ CDM”. In: *The Astrophysical Journal* 876.1, p. 85. DOI: [10.3847/1538-4357/ab1422](https://doi.org/10.3847/1538-4357/ab1422). URL: <https://doi.org/10.3847/1538-4357/ab1422>.
- Rozo, E. et al. (2010). “Cosmological Constraints from the Sloan Digital Sky Survey maxBCG Cluster Catalog”. In: 708, pp. 645–660. DOI: [10.1088/0004-637X/708/1/645](https://doi.org/10.1088/0004-637X/708/1/645). arXiv: [0902.3702](https://arxiv.org/abs/0902.3702) [[astro-ph.CO](https://arxiv.org/abs/0902.3702)].
- Rykoff, E. S. et al. (2014). “redMaPPer. I. Algorithm and SDSS DR8 Catalog”. In: 785, 104, p. 104. DOI: [10.1088/0004-637X/785/2/104](https://doi.org/10.1088/0004-637X/785/2/104). arXiv: [1303.3562](https://arxiv.org/abs/1303.3562).
- Salvati, Laura et al. (2018). “Constraints from thermal Sunyaev-Zel’dovich cluster counts and power spectrum combined with CMB”. In: *A&A* 614, A13. DOI: [10.1051/0004-6361/201731990](https://doi.org/10.1051/0004-6361/201731990). URL: <https://doi.org/10.1051/0004-6361/201731990>.
- Salvato, Mara et al. (2019). “The many flavours of photometric redshifts”. In: *Nature Astronomy* 3, pp. 212–222. DOI: [10.1038/s41550-018-0478-0](https://doi.org/10.1038/s41550-018-0478-0). arXiv: [1805.12574](https://arxiv.org/abs/1805.12574) [[astro-ph.GA](https://arxiv.org/abs/1805.12574)].
- Sánchez, Ariel G. et al. (2017). “The clustering of galaxies in the completed SDSS-III Baryon Oscillation Spectroscopic Survey: Cosmological implications of the configuration-space clustering wedges”. In: 464.2, pp. 1640–1658. DOI: [10.1093/mnras/stw2443](https://doi.org/10.1093/mnras/stw2443). arXiv: [1607.03147](https://arxiv.org/abs/1607.03147) [[astro-ph.CO](https://arxiv.org/abs/1607.03147)].
- Sartoris, B. et al. (2016). “Next Generation Cosmology: Constraints from the Euclid Galaxy Cluster Survey”. In: *Mon. Not. Roy. Astron. Soc.* 459.2, pp. 1764–1780. DOI: [10.1093/mnras/stw630](https://doi.org/10.1093/mnras/stw630). arXiv: [1505.02165](https://arxiv.org/abs/1505.02165) [[astro-ph.CO](https://arxiv.org/abs/1505.02165)].
- Schechter, P. (1976). “An analytic expression for the luminosity function for galaxies.” In: 203, pp. 297–306. DOI: [10.1086/154079](https://doi.org/10.1086/154079).
- Scrimgeour, Morag I. et al. (2012). “The WiggleZ Dark Energy Survey: the transition to large-scale cosmic homogeneity”. In: *Monthly Notices of the Royal Astronomical Society* 425.1, pp. 116–134. ISSN: 0035-8711. DOI: [10.1111/j.1365-2966.2012.21402.x](https://doi.org/10.1111/j.1365-2966.2012.21402.x). eprint: <http://oup.prod.sis.lan/mnras/article-pdf/425/1/116/3176116/425-1-116.pdf>. URL: <https://doi.org/10.1111/j.1365-2966.2012.21402.x>.
- Sereno, Mauro et al. (2015a). “CoMaLit - IV. Evolution and self-similarity of scaling relations with the galaxy cluster mass”. In: 450, pp. 3675–3695. DOI: [10.1093/mnras/stv814](https://doi.org/10.1093/mnras/stv814).
- Sereno, Mauro et al. (2015b). “New constraints on  $\sigma_8$  from a joint analysis of stacked gravitational lensing and clustering of galaxy clusters”. In: *Monthly Notices of the Royal Astronomical Society* 449.4, pp. 4147–4161.
- Sheth, R. K. et al. (2001). “Ellipsoidal collapse and an improved model for the number and spatial distribution of dark matter haloes”. In: 323, pp. 1–12. DOI: [10.1046/j.1365-8711.2001.04006.x](https://doi.org/10.1046/j.1365-8711.2001.04006.x). eprint: [astro-ph/9907024](https://arxiv.org/abs/astro-ph/9907024).
- Sheth, Ravi K. et al. (1999). “Large-scale bias and the peak background split”. In: *Monthly Notices of the Royal Astronomical Society* 308.1, pp. 119–126. ISSN: 0035-8711. DOI: [10.1046/j.1365-8711.1999.02692.x](https://doi.org/10.1046/j.1365-8711.1999.02692.x). eprint: <http://oup.prod.sis.lan/mnras/article-pdf/308/1/119/18409158/308-1-119.pdf>. URL: <https://doi.org/10.1046/j.1365-8711.1999.02692.x>.

- Simet, Melanie et al. (2017). “Weak lensing measurement of the mass-richness relation of SDSS redMaPPer clusters”. English (US). In: *Monthly Notices of the Royal Astronomical Society* 466.3, pp. 3103–3118. ISSN: 0035-8711. DOI: [10.1093/mnras/stw3250](https://doi.org/10.1093/mnras/stw3250).
- Smith, Sinclair (1936). “The Mass of the Virgo Cluster”. In: 83, p. 23. DOI: [10.1086/143697](https://doi.org/10.1086/143697).
- Sunyaev, R. A. et al. (1972). “The Observations of Relic Radiation as a Test of the Nature of X-Ray Radiation from the Clusters of Galaxies”. In: *Comments on Astrophysics and Space Physics* 4, p. 173.
- T. Duncan, C. Tyler (2008). *Your Cosmic Context: An Introduction to Modern Cosmology*. Pearson Addison-Wesley.
- Tinker, J. L. et al. (2010). “The Large-scale Bias of Dark Matter Halos: Numerical Calibration and Model Tests”. In: 724, pp. 878–886. DOI: [10.1088/0004-637X/724/2/878](https://doi.org/10.1088/0004-637X/724/2/878). arXiv: [1001.3162](https://arxiv.org/abs/1001.3162).
- Totsuji, H. et al. (1969). “The Correlation Function for the Distribution of Galaxies”. In: 21, p. 221.
- Trentham, Neil (2005). *The Early Universe*. "<https://www.ast.cam.ac.uk/~trentham/cosmology/lec3.pdf>".
- Veropalumbo, A. et al. (2014). “An improved measurement of baryon acoustic oscillations from the correlation function of galaxy clusters at  $z = 0.3$ ”. In: 442, pp. 3275–3283. DOI: [10.1093/mnras/stu1050](https://doi.org/10.1093/mnras/stu1050). arXiv: [1311.5895](https://arxiv.org/abs/1311.5895).
- (2016). “Measuring the distance-redshift relation with the baryon acoustic oscillations of galaxy clusters”. In: 458, pp. 1909–1920. DOI: [10.1093/mnras/stw306](https://doi.org/10.1093/mnras/stw306). arXiv: [1510.08852](https://arxiv.org/abs/1510.08852).
- Vikhlinin, A. et al. (2009). “Chandra Cluster Cosmology Project III: Cosmological Parameter Constraints”. In: 692, pp. 1060–1074. DOI: [10.1088/0004-637X/692/2/1060](https://doi.org/10.1088/0004-637X/692/2/1060). arXiv: [0812.2720](https://arxiv.org/abs/0812.2720).
- Yee, H. K. C. et al. (2002). “Optical Surveys for Galaxy Clusters”. In: *Astronomical Society of the Pacific Conference Series* 257. Ed. by Lin-Wen Chen et al., p. 109. arXiv: [astro-ph/0111431](https://arxiv.org/abs/astro-ph/0111431) [[astro-ph](https://arxiv.org/abs/astro-ph)].
- Zwicky, F. (1933). “Die Rotverschiebung von extragalaktischen Nebeln”. In: *Helvetica Physica Acta* 6, pp. 110–127.
- (1937). “On the Masses of Nebulae and of Clusters of Nebulae”. In: 86, p. 217. DOI: [10.1086/143864](https://doi.org/10.1086/143864).
- Zwicky, F. et al. (1961). *Catalogue of galaxies and of clusters of galaxies, Vol. I*.